ABSTRACT

Title of dissertation: WAVES IN PLASMAS GENERATED BY A ROTATING MAGNETIC FIELD AND IMPLICATIONS TO RADIATION BELTS

Alexey V. Karavaev, Doctor of Philosophy, 2010

Dissertation directed by: Adviser: Professor Konstantinos Papadopoulos
Department of Physics and
Department of Astronomy

The interaction of rotating magnetic fields (RMF) with magnetized plasmas is a fundamental plasma physics problem with implications to a wide range of areas, including laboratory and space plasma physics. Despite the importance of the topic the basic physics of the phenomenon remains unexplored. An important application of a RMF is its potential use as an efficient radiation source of low frequency waves in space plasmas, including whistler and shear Alfvén waves (SAW) for controlled remediation of energetic particles in the Earth's radiation belts.

In this dissertation the RMF waves generated in magnetized plasma are studied using numerical simulations with a semi-analytical three-dimensional magnetohydrodynamic (MHD) model and experiments on the generation of whistler and magnetohydrodynamic waves conducted in UCLA's Large Plasma Device. Comparisons of the simulation results with the experimental measurements, namely, measured spatiotemporal wave structures, dispersion relation with finite transverse wave number, wave amplitude dependence on plasma and RMF source parameters,

show good agreement in both the whistler and MHD wave regimes. In both the experiments and the 3D MHD simulations a RMF source was found to be very efficient in the generation of MHD and whistler waves with arbitrary polarizations. The RMF source drives significant field aligned plasma currents confined by the ambient magnetic field for both the whistler and MHD wave regimes, resulting in efficient transport of wave energy along the ambient magnetic field. The efficient transfer of the wave energy results in slow decay rates of the wave amplitude along the ambient magnetic field. The circular polarization of the waves generated by the RMF source, slow amplitude decay rate along the ambient magnetic field and nonzero transverse wave number determined by the RMF source size lead to nonlocal gradients of the wave magnetic field in the direction perpendicular to the ambient magnetic field.

A RMF can be generated by a system of polyphase alternating currents or by a rotating permanent or superconducting magnet. For the magnetospheric plasma rotating permanent or superconducting magnets are suitable for injection of very low frequency (VLF) shear Alfvén and magnetosonic waves. The generation of whistler waves in the magnetosphere plasma requires frequencies of the order of kHz, so in order to inject whistler waves generated by a RMF it is necessary to use an antenna with polyphase alternating currents.

The interactions of the waves generated by a RMF source with highly energetic electron population were investigated in LAPD experiment and by test-particle simulations of non-resonant pitch angle scattering of trapped energetic electrons using the electromagnetic fields calculated using the 3D model. It was found in both the experiment and test-particle simulations that waves generated by a RMF source are,

indeed, very efficient in pitch angle scattering of trapped hot electrons due to the creation of magnetic field gradients in the direction perpendicular to the ambient magnetic field. Different scenarios for the applications to the precipitation of highly energetic electrons in the magnetosphere are presented.

WAVES IN PLASMAS GENERATED BY A ROTATING MAGNETIC FIELD AND IMPLICATIONS TO RADIATION BELTS

by

Alexey V. Karavaev

Dissertation submitted to the Faculty of the Graduate School of the
University of Maryland, College Park in partial fulfillment
of the requirements for the degree of
Doctor of Philosophy
2010

Advisory Committee:
Professor Konstantinos Papadopoulos, Chair/Advisor
Dr. A. Surjalal Sharma
Distinguished professor Roald Sagdeev
Professor Thomas Antonsen
Professor James Drake
Professor Ramani Duraiswami
Dr. Parvez N. Guzdar
Professor Adil Hassam

To all my Mentors, who had ever put a thing into my head.

In memory of my loving Grandpa, who was a high-school teacher of Math and Physics for more then 40 years.

Acknowledgments

It is impossible to fully express my gratitude to all the people who have made this dissertation possible and because of whom my graduate student experience at the University of Maryland has been one that I will cherish for the rest of my life.

First of all I would like to thank my co-advisors back in Russia, Academician Evgeniy Nikolaevich Avrorin and Dr. Vadim Aleksandrovich Simonenko, who brought me into the program of joint graduate school between the University of Maryland and Moscow Engineering and Physics Institute (MEPhI). I also deeply thank Distinguished Professor of the University of Maryland Dr. Roald Sagdeev for bringing the wonderful idea of this program to life and his welcoming and hosting me as a member of this program. He has given me continuous support and inspiration during my graduate years. I would like to express my gratitude to the director of Russian Federal Nuclear Centre - Zababahin Institute of Technical Physics (RFNC-VNIITF) - my employer in Russia, Dr. Georgiy Nikolaevich Rykovanov, for letting me out and giving me the opportunity to study at the University of Maryland Graduate School.

Of course this dissertation would be impossible without my advisor, Professor Dennis Papadopoulos, who has given me an invaluable opportunity to do interesting research work involving all the parts of physics a physicist can wish for: an experiment, a theory and numerical simulations. He gave me the opportunity to perform experiments in the world-class state-of-the-art research plasma facility LAPD located in UCLA. His experience as a plasma physicist and his insightful

advice guided and gave shape to my work. He is definitely a kind of boss a graduate student can only wish.

I also would like to thank my co-adviser Dr. A. Surjalal Sharma who has directed my writing of published papers and this dissertation. I am very grateful to Dr. Nail Gumerov whose point of view as a mathematician on plasma physics helped me to see problems from different prospectives. Three-dimensional simulations performed in the frames of my research would be impossible without him. I thank Dr. Xi Shao for continuous discussions of my research work.

I thank all the members of the UCLA's Basic Plasma Science Facility team, and especially the head of the team Dr. Walter Gekelman, who made my experimental experience full and unforgettable, and Dr. Steven Vincena, who spent a lot of time with me in the laboratory doing my experiments, even during sunny weekends in Los Angeles, California.

It has been my pleasure to work with and learn from such distinguished and extraordinary individuals like all of you. I am really proud that I was a member of such an outstanding research team.

I also thank our fellow graduate student Aram Vartanyan who has helped me out with my English. So all the nice and fluent writing in this dissertation is because of him, while all the awkward sentences are because of me.

Thanks are due to all the committee members for agreeing to serve on my thesis committee and for sparing their free time in order to review the manuscript.

The research work was done with financial support of ONR MURI grant.

I would also like to acknowledge help and support from some of the Depart-

ment of Physics and Department of Astronomy staff members, and especially Jane Hessing, who was my "guarding angel" in the "rough sea" of paper work.

I owe my deepest thanks to all my family members, especially my parents who have always supported me through my career. I cannot possibly express my gratitude to my loving wife Oksana and my wonderful daughter Irina, for their extraordinary patience and continuous support during my graduate years at the University of Maryland. This dissertation is the reason why I spend almost four years away from them, and I hope it's worth it.

It is impossible to remember everyone, and I deeply apologize to those I have unintentionally forgotten.

Once again thank you all!

Table of Contents

List of Tables

List of Figures

List of Abbreviations

AB	Adams-Bashforth method
AB4	Adams-Bashforth method of the fourth order
AB6	Adams-Bashforth method of the sixth order
ABM	Adams-Bashforth-Moulton method
ABM4	Adams-Bashforth-Moulton method of the fourth order
ABM6	Adams-Bashforth-Moulton method of the sixth order
BE	Backward Euler method
CMOS	Complementary MetalOxideSemiconductor
CN	Crank-Nicolson method
CPU	Central Processing Unit
ECRH	Electron Cyclotron Resonant Heating
ELF	Extremely Low Frequency range
EMHD	Electron MagnetoHydroDynamics
EMIC	Electromagnetic Ion Cyclotron
FFT	Fast Fourier Transform
FRC	Field-Reversed Configuration
GPU	Graphics Processing Unit
LAPD	LArge Plasma Device
LEO	Low Earth Orbiting (satellites)
LRC	LRC electrical circuit, consisting of inductance (L), resistance (R), and capacitance (C)
MHD	MagnetoHydroDynamics
NIB	Neodymium Iron Boron magnet
ODE	Ordinary Differential Equation
PRBR	Proton Radiation Belt Remediation
RB	Radiation Belts
RBR	Radiation Belt Remediation
RK3	Runge-Kutta method of the third order
RK4	Runge-Kutta method of the fourth order
RMF	Rotating Magnetic Field
SAA	South Atlantic Anomaly
SAW	Shear Alfvén Wave
SEE	Single Event Effect
SEU	Single Event Upset
VLF	Very Low Frequency range

Chapter 1

Introduction

The interaction of rotating magnetic fields (RMF) with plasmas is a fundamental plasma physics problem with implications to a wide range of areas, such as fusion related Field-Reversed Configuration (FRC) [16,43,51], space propulsion, precipitation of energetic particle populations in Van Allen radiation belts [50,73], near zone processes in pulsar magnetospheres, *etc.* Earth itself is an example of a rotating magnetic dipole interacting with surrounding magnetized plasma. The interaction of RMFs with laboratory plasmas has been studied for its applications for plasma confinement, *e.g.*, as a possible magnetic plasma confinement concept [16], which has come to be known as Field-Reversed Configuration (FRC) [43,51]. The FRC shares physical aspects to the generation of the waves in plasmas by a RMF source, but focuses on near field structures generated inside a RMF source. Waves generated by RMF sources in plasmas were studied in the Phaedrus-B mirror machine in terms of ion cyclotron resonance heating [68,97]. It was shown that a rotating magnetic field antenna excited a well controlled in terms of amplitude and polarization mode of shear Alfvén waves (SAW) and was found to be very efficient for transferring energy to ions. In space plasmas a RMF can be used as an efficient radiation source of low-frequency waves and has potential applications in the controlled precipitation of Earth's inner radiation belt energetic electrons [4,69]. In spite of its importance,

the basic plasma physics of the interaction of RMF with magnetoplasmas and the range of potential applications as a source of plasma waves remain unexplored.

At the simplest level a magnetic moment rotating in a collisionless plasma at a rate ω drives a current due to the difference in inertial response between electrons and ions. Electrons quickly come to a co-rotational motion with RMF, generating a differential azimuthal current whose maximum for frequencies $\omega \gg \Omega_{ci}$ (Ω_{ci} is the ion cyclotron frequency) is given by $J_\theta = n\omega r$, where n is the plasma density and r - radius of cylindrical plasma column. These currents can couple to plasma waves, which can propagate out the vicinity of a RMF source.

Because of the wide variety of conditions in the space and laboratory plasmas and the types of waves in magnetized plasmas (whistler, Alfvén, magnetosonic, lower-hybrid, ion-cyclotron, *etc.*) it is essential to understand the spatiotemporal structure of the RMF generated waves and the relevant scaling laws in order to control and optimize wave generation. This dissertation focuses on the study of two types of shear Alfvén and whistler waves generated by the RMF.

The shear Alfvén [6, 7] and whistler [11, 12] waves are two distinct electromagnetic modes of magnetized plasmas [78]. The first has frequencies ω below the ion cyclotron frequency Ω_{ci}, while the second has the frequencies in the range $\Omega_{ci} < \omega < \Omega_{ce}$ (Ω_{ce} is the electron cyclotron frequency). Along with the difference in the frequency bands, the characteristics of the MHD and whistler waves differ greatly. The MHD waves are controlled mainly by ion inertia, while the whistler wave parameters are determined mainly by electron dynamics. Together, the MHD and whistler waves cover a wide frequency spectrum, from very low frequencies up

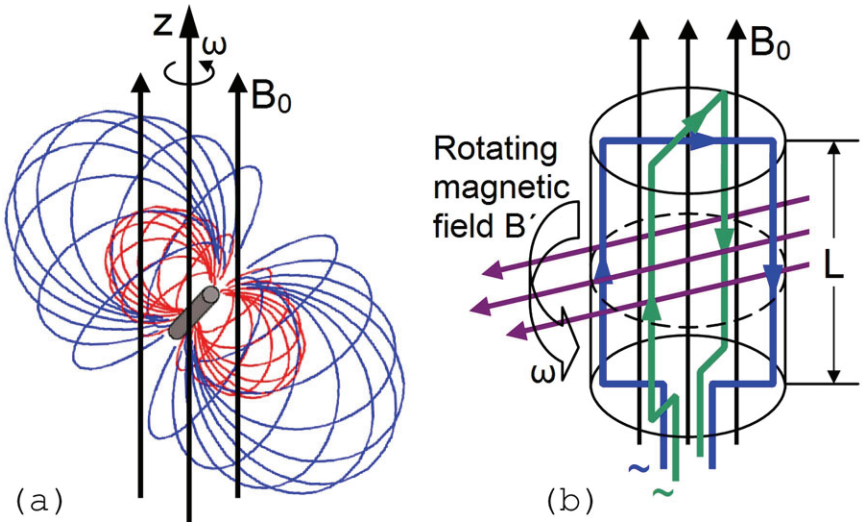

Figure 1.1: Methods for creating a rotating magnetic field (RMF) in a magnetized plasma. The RMF can be generated either by (a) a rotating permanent or superconducting magnet or (b) polyphase coils (superconducting or normal) with alternating phase shifted currents.

to the electron cyclotron frequency Ω_{ce}. Thus, the study of the interaction of RMF with plasma in these two wave regimes will provide a basic understanding of the RMF as a generic source of plasma waves. Key questions about the interaction of the RMF with magnetized plasmas include the coupling of the magnetic field to the plasma, the spatio-temporal structure of the excited waves as a function of the RMF and plasma parameters, and the decay of the wave magnetic field.

A RMF can be generated by an actually rotating permanent or superconducting magnet or by a system of polyphase coils with alternating currents (See Fig. 1.1). In the latter, alternating currents of the same amplitude and frequency but set $\pm 90^o$ out of phase in two orthogonal loops (See Fig. 1.1(b)) result in a magnetic moment which rotates clockwise or counterclockwise with respect to the

ambient magnetic field B_0 depending on the phase difference between the currents. Such RMF antenna provides good capability for controlling the magnetic moment magnitude and its polarization. In the case of a rotating permanent or superconducting magnet there are limitations depending on the ambient magnetic field. In the Earth's magnetosphere in the equatorial region of $L = 2$ the magnetic field is $\sim \mu T$, which yields a proton cyclotron frequency of tens of $Hertz$. (The L-shell, or L-parameter [91] is a parameter describing a particular set of planetary magnetic field lines. The L-value often describes the set of magnetic field lines which cross the Earth's magnetic equator at a multiple of Earth-radii equal to the L-value). In laboratory plasmas confined by an ambient magnetic field the typical value is order of $10^{-3} - 10^{-1}\ T$, which corresponds to an ion cyclotron frequency Ω_{ci} in the range $10^4 - 10^6\ Hz$. In order to generate whistler waves, distinct from the MHD waves, we need to drive the RMF at a rate ω much faster than the ion cyclotron frequency Ω_{ci}. It is obvious that one can rotate a permanent magnet at a rate of tens or even hundred of $Hertz$, but it is not practical to do that at kHz or higher rates.

In space experiments the generation of RMFs by an actually rotating permanent or superconducting magnet is preferable since it does not need powerful energy supply in order to drive significant currents. To a certain extent mechanical energy of rotation but not electric energy is used in this case to generate the waves in plasmas. The advantages of using of superconducting magnets are that they can produce stronger magnetic fields (up to tens of $Tesla$) than ordinary iron-core electromagnets or rare Earth permanent magnets, and can be cheaper to operate, since little power is lost to ohmic resistance in the windings. Another advantage

of using superconducting magnets is that they can be much lighter than equivalent permanent magnets, which is very important for a space experiment on RMF wave generation by a satellite-based source. In the laboratory experiments we are forced to use as a RMF source a system of alternating polyphase currents [35, 52].

In the study presented in this dissertation the interaction of RMFs with magnetized plasmas is considered from both the experimental and theoretical points of view. Experiments on generation of whistler and shear Alfvén waves by a RMF antenna were performed in UCLA's Large Plasma Device (LAPD). The experimental studies of the plasma waves generated by RMF were complemented by theoretical models and numerical simulations using three-dimensional semianalytical cold magnetized fluid models developed for simulations of waves generated by a RMF source in a wide range of regimes. A series of simulations with the parameters used in the experiments were performed to verify the accuracy of the model. This allowed us to study RMF generated plasma waves in the regimes that were not available in the LAPD experiments and apply the 3D models for space plasma parameters.

Although the interaction of RMFs with magnetized plasmas as a source of low-frequency waves is an interesting problem itself, the RMF generated waves have a potential applications to a control of populations of highly energetic charged particles in the Earth's inner radiation belts, which have hazardous effects on Low Earth Orbiting (LEO) satellites. The highly energetic electrons and protons are trapped by the Earth's magnetic field due to the conservation of the first adiabatic invariant. The RMF generated waves can produce the magnetic field perturbations with the transverse gradients of the normal component of the wave magnetic field. These

transverse magnetic field gradient can potentially lead to a breaking of the first adiabatic invariant and non-resonant pitch angle scattering of energetic particles to the loss cone. This problem is studied in this dissertation analytically and numerically by test-particle simulations of the interaction of trapped energetic electrons with RMF generated wave fields calculated using the 3D models.

This dissertation is organized as following: Chapter 2 focuses on generation of plasma waves by a RMF source in the whistler regime with the frequencies ω well above the ion cyclotron frequency Ω_{ci}. Chapter 2 provides a brief description of the Large Plasma Device (LAPD), a RMF radiation source and plasma diagnostics used in the experiments. The results of the experiments on the generation of whistler waves by a RMF antenna are presented in comparison with numerical results of a three-dimensional single-fluid electron magnetohydrodynamic (EMHD) model described in detail in Appendix A. The spatiotemporal structure and dispersion relation of the RMF generated whistler waves with finite transverse wave number are analyzed in Chapter 2.

Chapter 3 discusses the investigation of the shear Alfvén waves generated by the RMF rotating at rates $\omega < \Omega_{ci}$. It presents a comparison of the MHD wave parameters measured in the experiments and calculated using a 3D two magnetized fluid model, described in Appendix B. For the MHD waves the wave magnetic field structure, SAW dispersion relation, three-dimensional plasma current structure, amplitude dependence of the wave on the driving frequency, and wave energy analysis are presented. Good overall agreement of the experimental results and the 3D model was found for a wide range of the parameters of the plasma and RMF frequencies.

In both the whistler and shear Alfvén wave regimes the RMF source was found to be very efficient for generation of waves in magnetized plasma. The waves generated by the RMF have significant field aligned currents, which are well confined by the ambient magnetic field. These plasma currents provide the waves with capability to transport energy along the field lines efficiently, and decay at a slow rate in the direction of the ambient magnetic field. Another feature of the waves generated by the RMF antennas is that the waves have non-zero transverse component of wave number $k_\perp$, determined by the radiation source size. The non-zero transverse wave number gives high gradients of the wave magnetic field in the direction perpendicular to the ambient magnetic field. These gradients can lead to non-resonant pitch angle scattering of energetic trapped particles by breaking the first adiabatic invariant.

In Chapter 4 investigation of interaction of the RMF generated shear Alfvén waves with a population of highly energetic electrons trapped in a magnetic mirror configuration is presented. An experimental study of the interaction was conducted in the LAPD-machine. Chapter 4 provides summary of the experimental setup an the major findings. A numerical study of the interaction was done by test particle simulations of non-resonant pitch angle scattering of hot electrons in a magnetic mirror trap configuration in the setup similar to the experimental. The electromagnetic fields for the test particle simulations were produced by the 3D model. The effect of the RMF injected waves on detrapping energetic electron population was studied and compared to that of waves generated by a single magnetic loop antenna using test particle modeling. Both the LAPD experiment and the test par-

ticle simulations demonstrated that the waves generated by a RMF source are very efficient in pitch angle scattering of the trapped energetic electrons despite the lack of resonance conditions.

In Chapter 5 an overview of the work done in the frames of this dissertation is given. A brief description of the results of the study of the properties of the RMF generated shear Alfvén and whistler waves and their applications for the non-resonant pitch angle electron scattering by breaking the first adiabatic invariant is presented.

Chapter 2

Generation of whistler waves by a Rotating Magnetic Field (RMF) source

2.1 Introduction

In this chapter me first describe experiments conducted in the Large Plasma Device (LAPD) on generation of whistler waves by a RMF source created using poly-phased loop antennas. A brief description of the LAPD machine, the RMF source and plasma diagnostics used in the experiments on generation of whistler and shear Alfvén waves (See Chapter 3) are given. The experimental measurement results are presented in comparison with numerical simulation results obtained using three-dimensional Electron Magnetohydrodynamic (EMHD) model described in detail in Appendix A. The dependence of parameters of the whistler waves generated by RMF source on the plasma an the RMF source parameters and the whistler wave mode dispersion relation with finite transverse wave number determined by the radiating antenna size are analyzed.

2.2 Experiments on the generation of whistler waves by RMF source

The experiments on generating whistler waves in magnetized plasmas by a RMF source were performed in the upgraded large plasma device LAPD-U [29]

operated by the Basic Plasma Science Facility at the University of California, Los Angeles. The device is an 18 m long and 1 m in diameter stainless steel cylindrical vacuum chamber surrounded by 56 pancake electromagnets with DC currents placed at 32 cm intervals (See Figs. 2.1, 2.2). The currents in the electromagnet coils can be adjusted independently, thus providing the capability to create a solenoidal stationary magnetic field with arbitrary profile along the device. There are 488 ports evenly distributed along the device to provide access to various diagnostics inside the plasma column. 65 of these ports at 32 cm interval along the device are equipped with ball joints and gate valves which allows for insertion and two-dimensional movement of diagnostic probes [56] (See Fig. 2.3).

The LAPD generates a highly reproducible, magnetized DC discharge plasma in noble gases (He, Ne, Ar) of low pressure ($\sim 10^{-4} Torr$). The discharge occurs between a heated barium-oxide coated nickel cathode and a molybdenum mesh anode (See Fig. 2.4) separated by 52 cm and placed on the very left of the device shown in Fig. 2.2. The plasma generation repetition rate is 1 Hz. The plasma density is measured by a microwave interferometer placed in the middle of the device. Two typical interferometer traces measured for two different discharges are shown in Fig. 2.5. Note a very high reproducibility of the plasma density profile. The measurements of the wave parameters with the frequencies of hundreds of Hz are usually performed in the afterglow of the discharge and take about $0.1 - 0.2$ ms. During that time the plasma density is nearly constant. Because of electron-ion recombination the density decays exponentially in time, and by conducting experiments in the afterglow it is possible to collect data for various plasma densities.

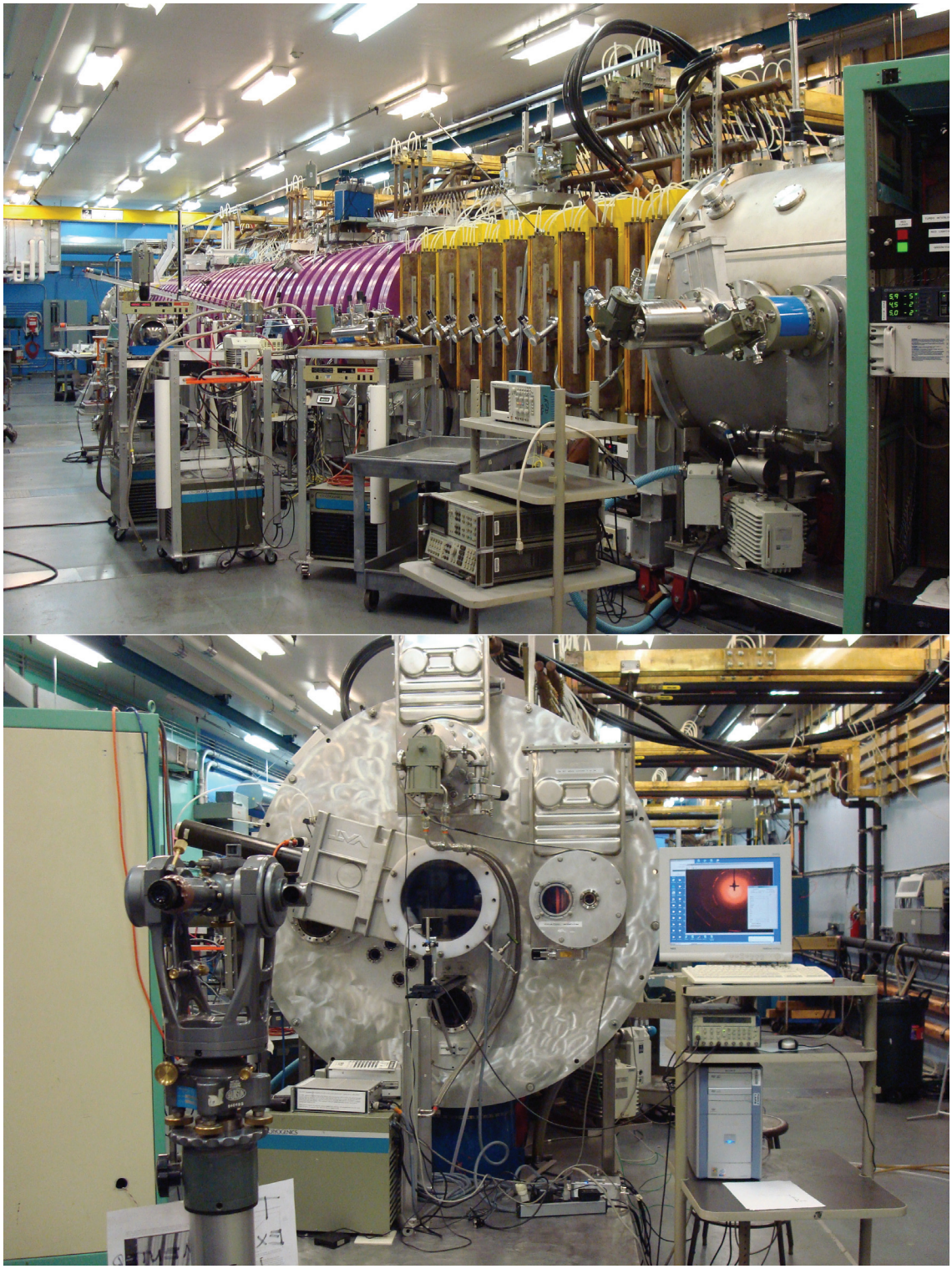

Figure 2.1: General view of the LAPD machine - 18 m long and 1 m in diameter stainless steel cylindrical vacuum chamber surrounded by 56 pancake electromagnets with DC current placed at 32 cm interval, which provide stationary ambient magnetic field of arbitrary profile along the device.

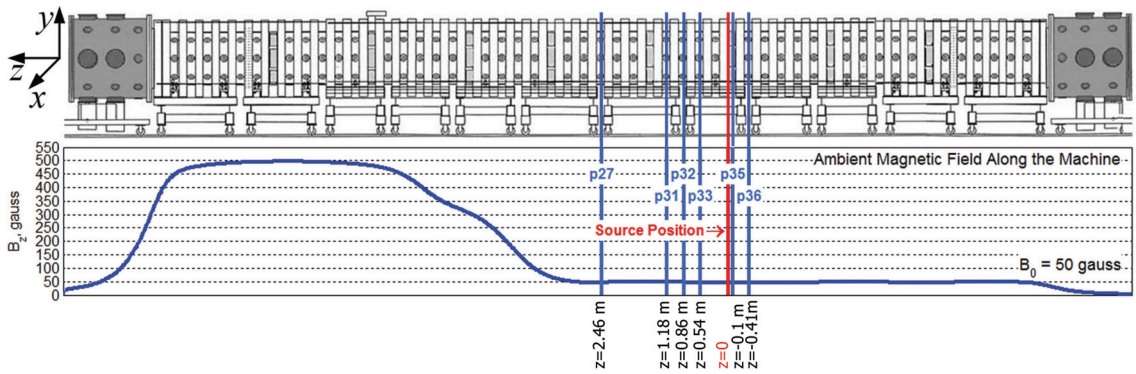

Figure 2.2: Ambient magnetic field profile along the chamber. p27, p31, p32, p33, p35, p36 are the measurement planes. Red line is the position of radiation source.

Figure 2.3: LAPD machine port equipped with ball joint and gate valve, which allows for insertion and two-dimensional movement of diagnostic probes.

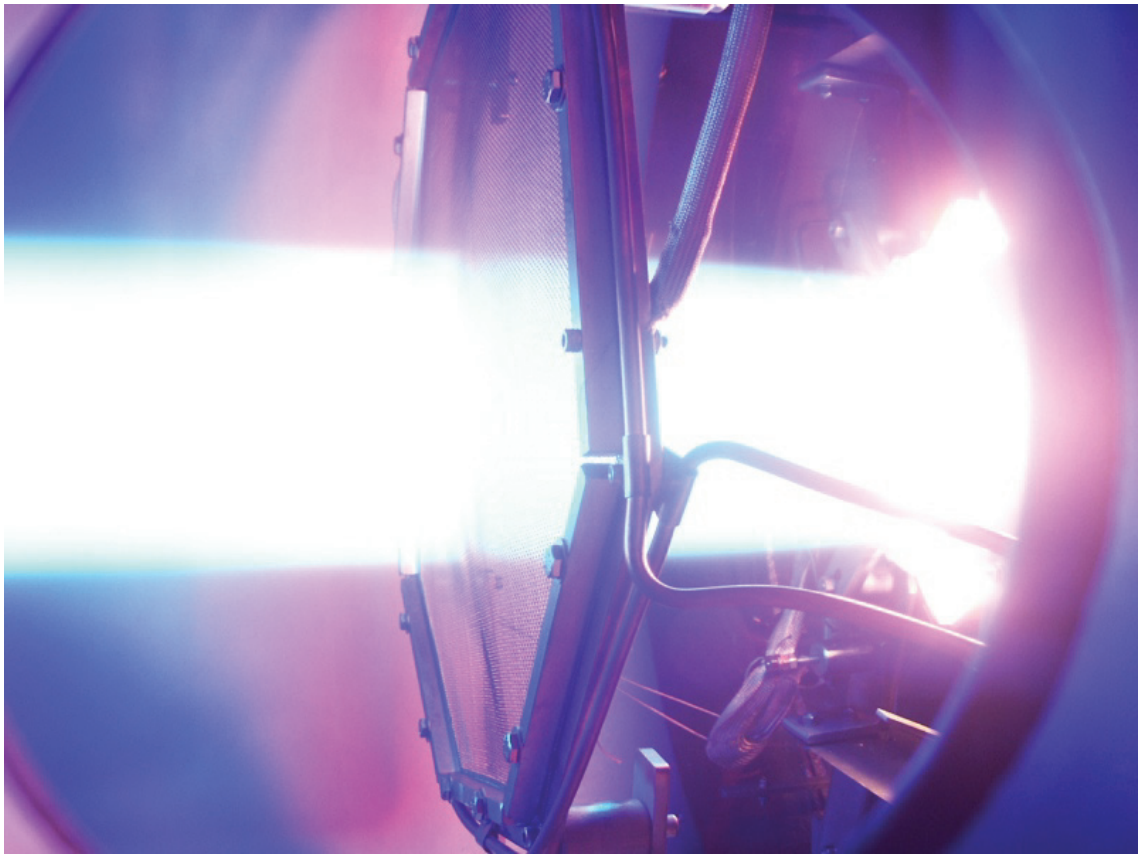

Figure 2.4: Development of helium plasma column in LAPD machine. The DC discharge occurs between a heated barium-oxide coated nickel cathode and a molybdenum mesh anode separated by 52 *cm* (Credit: Walter Gekelman, UCLA)

The ambient magnetic field profile used in the experiment for generating whistler waves by the RMF source, and the location of the probes and radiation source are shown in Fig. 2.2. The laboratory reference frame is oriented with the z-axis along the axis of the chamber, and the y-axis pointing vertically upwards. Using a computer controlled data acquisition system in several cross sections of the machine (See Fig. 2.2), measurements of the three components of the induced magnetic field using three axis inductive loop magnetic pickup coils [25] were per-

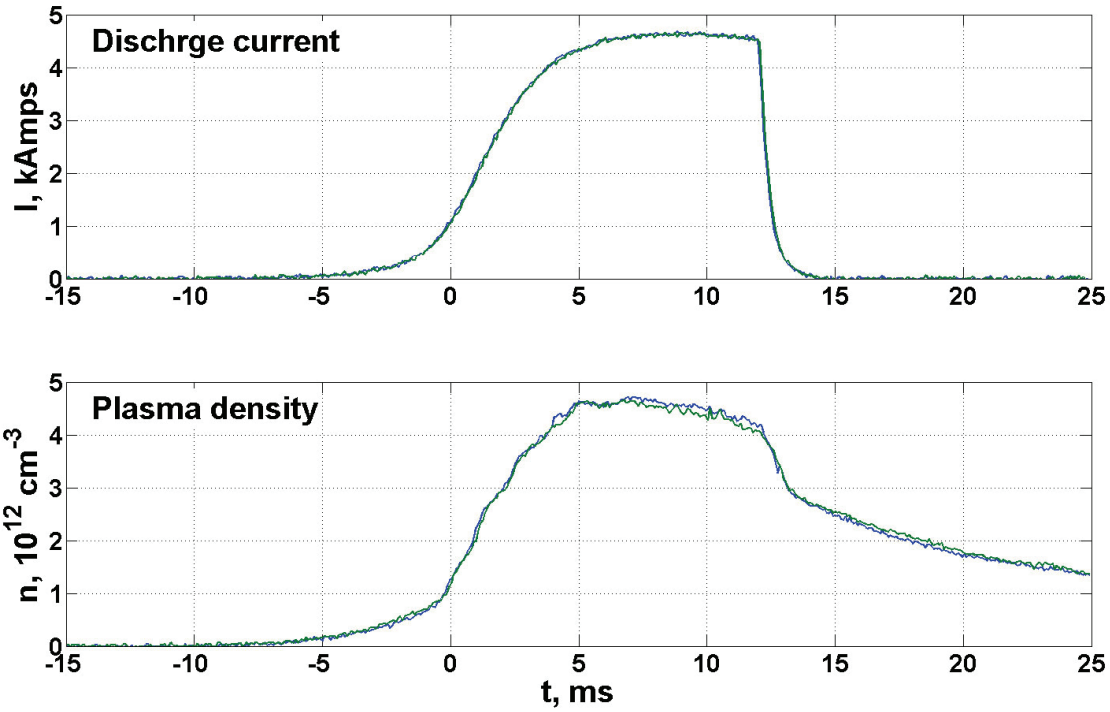

Figure 2.5: Discharge current and corresponding generated plasma density measured by microwave interferometer for two different discharges. Note the high reproducibility of the plasma density profiles.

formed on a square area with 25×25 points with 1 cm spacing. The probe features differentially wound loops that eliminate electrostatic pickup when used in conjunction with a differential amplifier (See Fig. 2.6). The loops are wound around a 1 mm cube with 10 turns each. The cube is mounted within a glass tube and attached to a thin ceramic tube extending from the end of a stainless steel probe shaft. The measurements were made in the 50 $Gauss$ region, which corresponds to cyclotron frequencies $\Omega_{ce} = 8.7 \times 10^8 s^{-1}$ ($f_{ce} = 1.39 \times 10^8\ Hz$) for electrons and $\Omega_{ci} = 1.21 \times 10^5 s^{-1}$ ($f_{ci} = 19.3\ kHz$) for ions (in a He gas discharge). The measurements closest to the radiation source were performed at distance ~ 10 cm (p35 in

Fig. 2.2). The measurements farthest from the antenna were performed at distance $\sim 2.5\ m$ (p27 in Fig. 2.2). The average plasma density measured by a 56 GHz microwave interferometer was $n = 8.3 \times 10^{10} cm^{-3}$. That corresponds to plasma frequency $\omega_{pe} = 1.62 \times 10^{10} s^{-1}$ and electron skin-depth $d_e = c/\omega_{pe} = 1.85\ cm$.

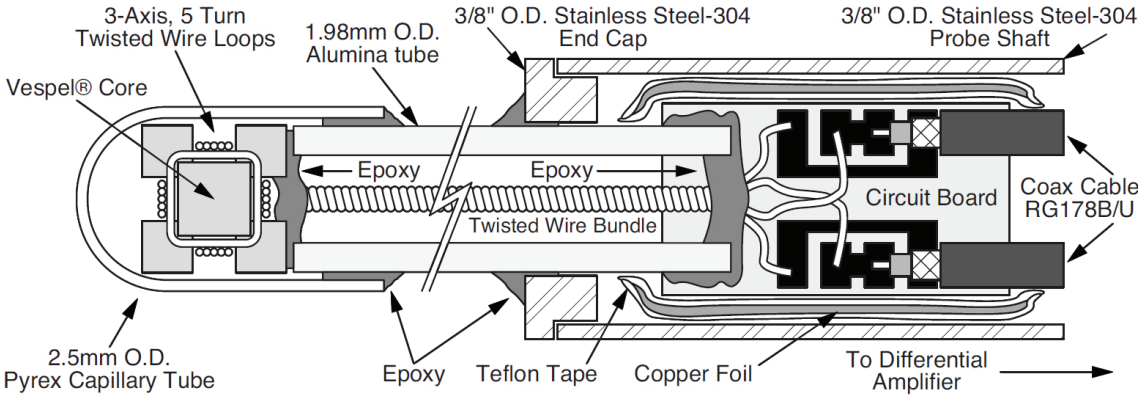

Figure 2.6: Cross-sectional view of the b-dot probe used in the experiments (Adopted from [25]).

A two-loop antenna (See Fig. 2.7) is placed inside the machine in such a way that the loops of the antenna are in the $x - z$ and $y - z$ planes, and centers of the loops were on the central axis of the chamber. The antenna consists of two independent coils $\sim 9\ cm$ in diameter ($\sim 5d_e$) and four turns each. Each coil has an independent power supply (resonant adjustable LRC circuits) that can drive an alternating current with frequencies $50 - 500\ kHz$ and current magnitude up to 500 *Amps*. The effect of mutual inductance between the coils is negligible. First of all the coils are at right angles, thus minimizing the mutual inductance. Further, the alternating currents in the orthogonal loops are independently adjusted (amplitude and phase) by two independent power supplies and two independent LRC driving

circuits. These currents are measured throughout the experiments along with the wave magnetic fields and do not change over a data run. Furthermore, the measurements of the currents in both coils even when one of the power supplies was turned off were performed. In that case when one of the currents was $\sim$ 130 *Amps* the second was less than 1 *Amp*. That is, the effect of mutual inductance was of order 1 %. The direction of rotation of the magnetic field created by the antenna can be changed by adjusting the relative phase of the currents in the loops. A driving frequency ($f_d = 293\ kHz$) was used so that $\Omega_{ci} \ll \omega \ll \Omega_{ce} \ll \omega_{pe}$.

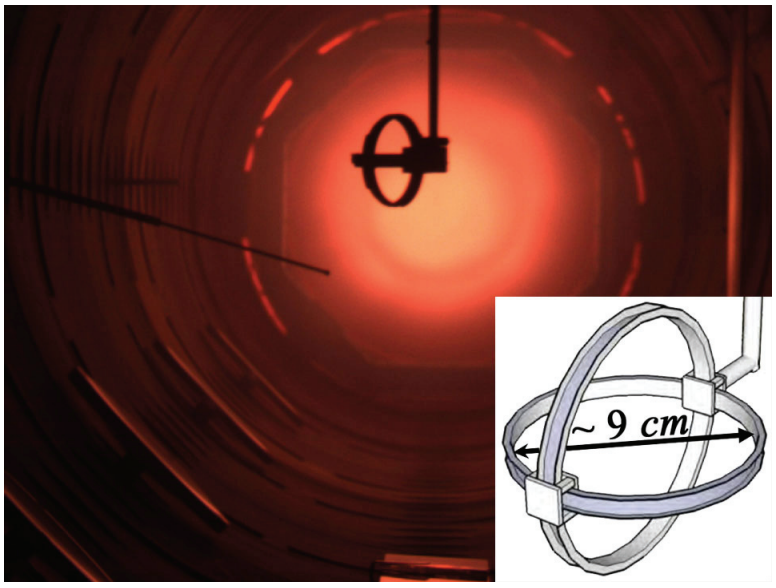

Figure 2.7: The RMF antenna consisting of two independent coils approximately 9 *cm* in diameter with four turns each, shown inside the LAPD chamber (The orientation of the antenna shown is not an actual orientation was used in the experiments). The three axis inductive magnetic pickup probe on the tip of the stainless steel shaft are also seen. Inset shows the design of the RMF antenna.

A typical input signal is shown in Fig. 2.8(a). The magnetic field components measured at the central axis of the machine at distance $\sim$ 86 *cm* away from the

antenna when both coils were driven with a phase difference $\pi/2$ to generate the RMF are shown in Fig. 2.8(b). Figure 2.8 (c) shows the output signal when the loop lying in $x - z$ plane was turned off. Two nearly identical currents with peak magnitude ~ 130 *Amps* were driven in the loops. In order to create right-handed or left-handed rotation of the magnetic field with respect to the ambient magnetic field direction the relative phase difference was set to either $\pi/2$ or $-\pi/2$. To compare the plasma response to the RMF with that of a one-loop antenna, experiments were performed with one current turned off. In both cases of the one-loop and two-loop antennas, the B_z component (along the ambient magnetic field) of induced magnetic field was much smaller than the perpendicular component. In the two-loop antenna case we get nearly steady induced magnetic field, which rotates around the z-axis clockwise or counterclockwise depending on the polarization of the RMF source. In contrast to this in the case of one loop-antenna we get oscillations of $B_{norm} = \sqrt{B_x^2 + B_y^2}$, and the wave has nearly plane polarization. These features are shown by the hodographs (insets) in Fig. 2.8.

Figure 2.9 illustrates the method used to determine the longitudinal phase velocity $v_{ph||}$ of the generated wave. In order to find $v_{ph||}$, the equal phase points of the induced magnetic field components at different z locations but with the same x and y coordinates were required. For this purpose, it is convenient to use the zeros of the magnetic field components (black circles in Fig. 2.9). Then these points were fitted with linear functions (black dashed inclined lines in Fig. 2.9), whose slope gives the longitudinal phase velocity, which was found to be $v_{ph||} = (7.74 \pm 0.76) \times 10^6 m/s$. That gives the wave numbers along the ambient magnetic field $k_{||} = 0.217-$

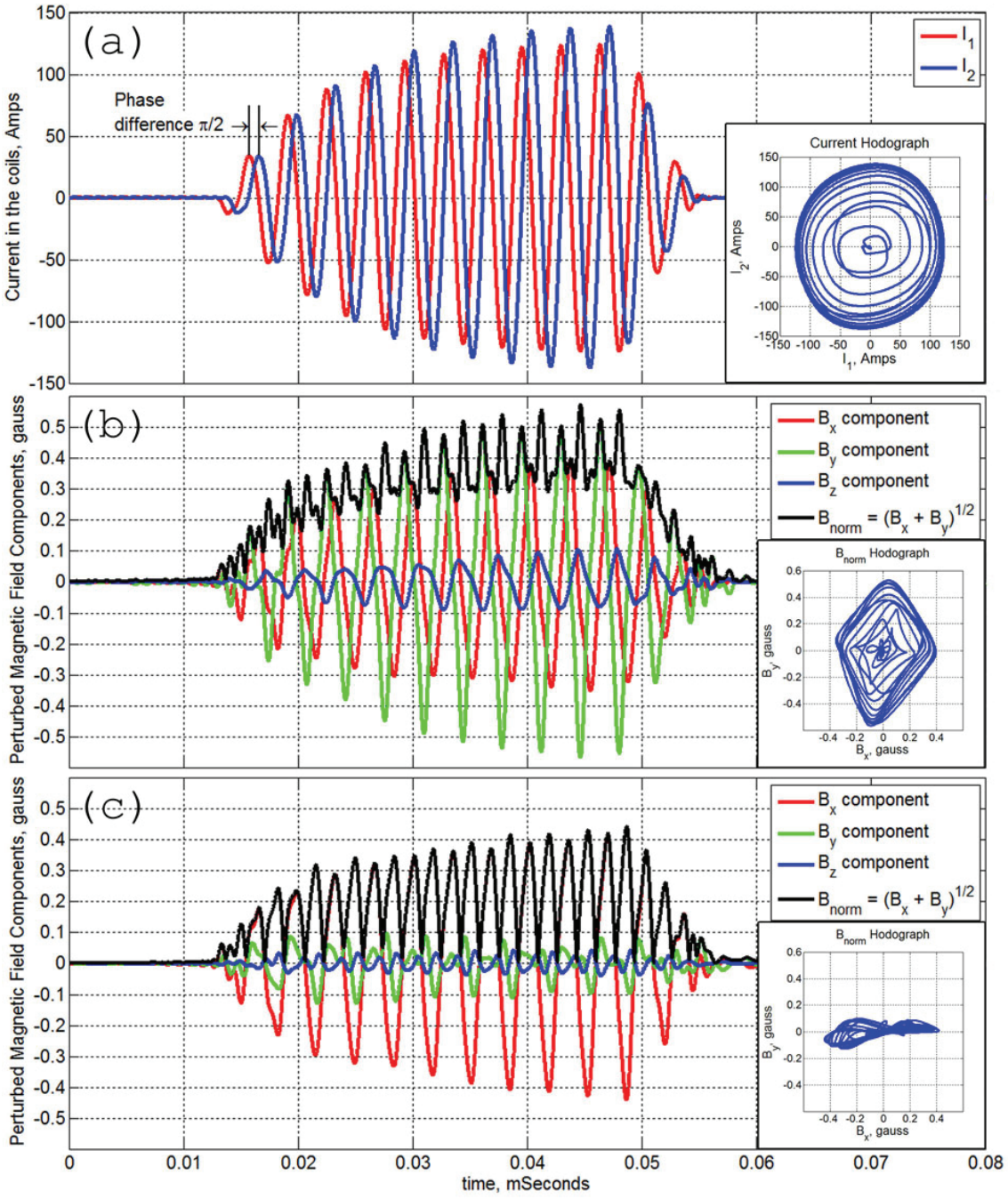

Figure 2.8: (a) Dependence of input current on time (two currents are on), (b) induced magnetic field components on the central line of the machine ~ 86 *cm* away from the radiation source (two currents are on), (c) induced magnetic field components on the central line of the machine ~ 86 *cm* away from the radiation source (one current is off).

$0.264m^{-1}$, which does not depend on the direction of rotation of the RMF or if it is a one-loop antenna. That corresponds to the longitudinal wave-length $\lambda_{||} = 23.8 - 29.0\ m$ which is much larger than the antenna size and is larger than the LAPD machine length.

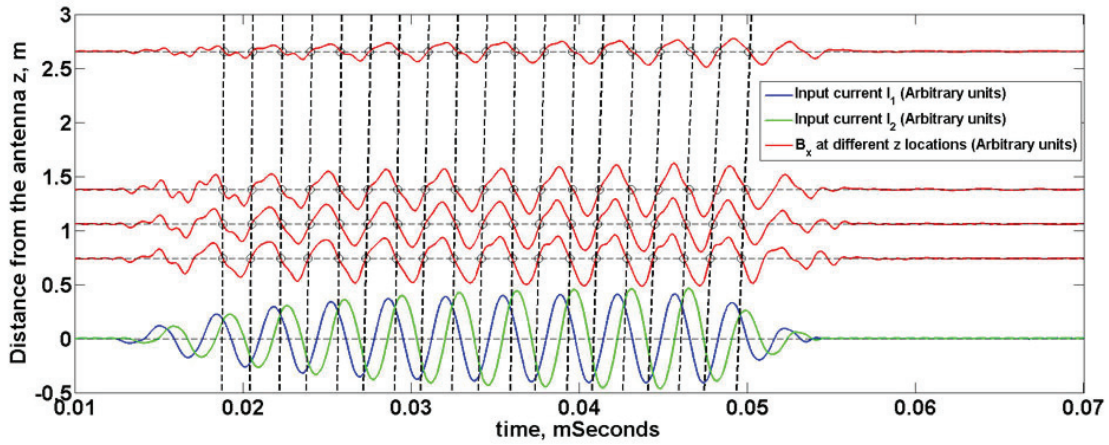

Figure 2.9: An illustration of how the longitudinal phase velocity is determined from the experiment measurements. Red lines represent B_x components of the induced magnetic field on the central axis of the LAPD machine at different z locations. Black circles represent the points of the equal phases (in this case zeroes of B_x) in different z locations. Inclined dashed lines are linear fit of the equal phases points, whose slope gives the phase velocity. The input currents are shown for a reference.

In Fig. 2.10 normalized spectra of input (Fig. 2.10(a)) and response (Fig. 2.10(b)) are presented. One can see that measured signals contain many harmonics of the main frequency, but with significantly smaller amplitudes. In Fig. 2.11 the wave structures in the plane perpendicular to the ambient magnetic field line for four different instants separated by $T/4 = \pi/(2\omega)$ are presented. The main feature of the plasma response is a two-vortex structure of the magnetic field, which corresponds to field aligned plasma currents. The distance between their centers is $\sim 14\ cm$, which

is ~ 1.5 times the diameter of the antenna loops. The measurements show that this distance does not depend on time and the distance from the radiation source along z-axis. It implies that in the plane transverse to the ambient magnetic field the wave has nearly constant characteristics and is well confined by the ambient magnetic field. The entire field structure rotates either clockwise or counterclockwise depending on the phase shift between the two input currents. In the one-loop case the radiation pattern does not rotate but oscillates with frequency ω. It means that the circularly polarized whistler wave generated by the RMF source is preferable for creating non-local magnetic field gradient than the plane polarized wave generated by the one-loop antenna.

2.3 Comparison of EMHD model and experiment

A three-dimensional electron magnetohydrodynamics (EMHD) code described in detail in Appendix A was used to simulate the experiment using the same parameters, *viz.* antenna loops size - 9 cm, current magnitude - 130 $Amps$, driving frequency - $f_d = 293\ kHz$, electron plasma density - $8.3 \times 10^{10} cm^{-3}$, and ambient magnetic field - 50 $Gauss$. A typical mesh size of $256 \times 256 \times 512$ grid points was used in the simulations. In Fig. 2.12 the magnetic field structure measured in the experiment (Fig. 2.12(a)) is compared to the simulations using the 3D EMHD model for the experimental parameters (Fig. 2.12(b)). This figure shows the field at the plane perpendicular to the ambient magnetic field for the same instant of time. One can see not only qualitative but also quantitative agreement between the 3D EMHD

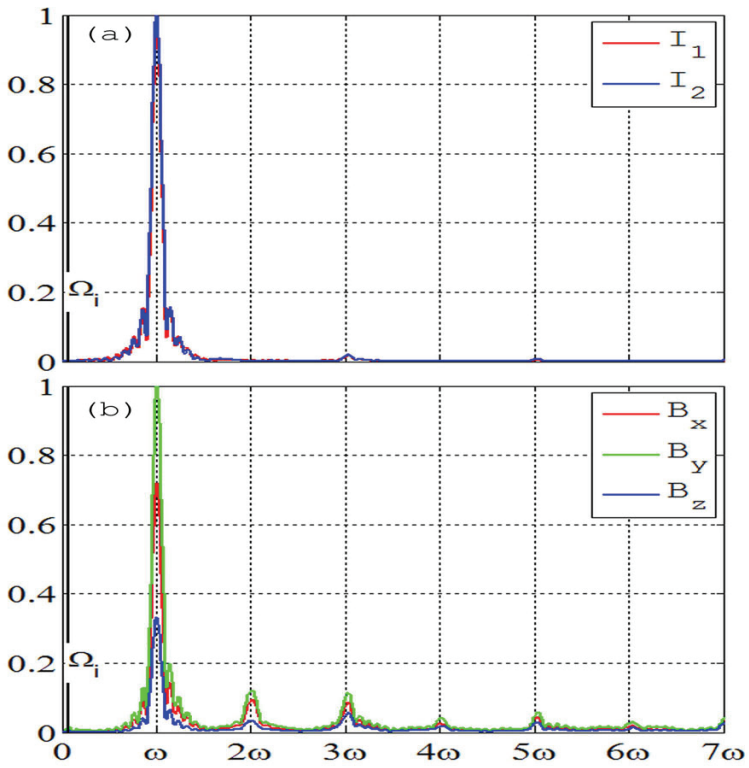

Figure 2.10: Input current (a) and typical response signal on the central axis of the LAPD machine ~ 86 *cm* away from the radiation source (b) normalized spectra.

model and the experiment. Once again I want to draw the reader's attention to the two vortex structure of the magnetic field corresponding to the field aligned plasma currents.

The radiation patterns (square of the normal component of the magnetic field averaged over a period of rotation, which is essentially the wave intensity) for one-loop (Fig. 2.13) and two-loop with right handed rotation (Fig. 2.14) cases measured in the experiment (a.1)-(a.6) and calculated using the 3D EMHD model (b.1)-(b.6) are presented. Also in Figs. 2.13 and 2.14 the comparison of experimental and model dependence of the amplitude of the induced magnetic field along the trans-

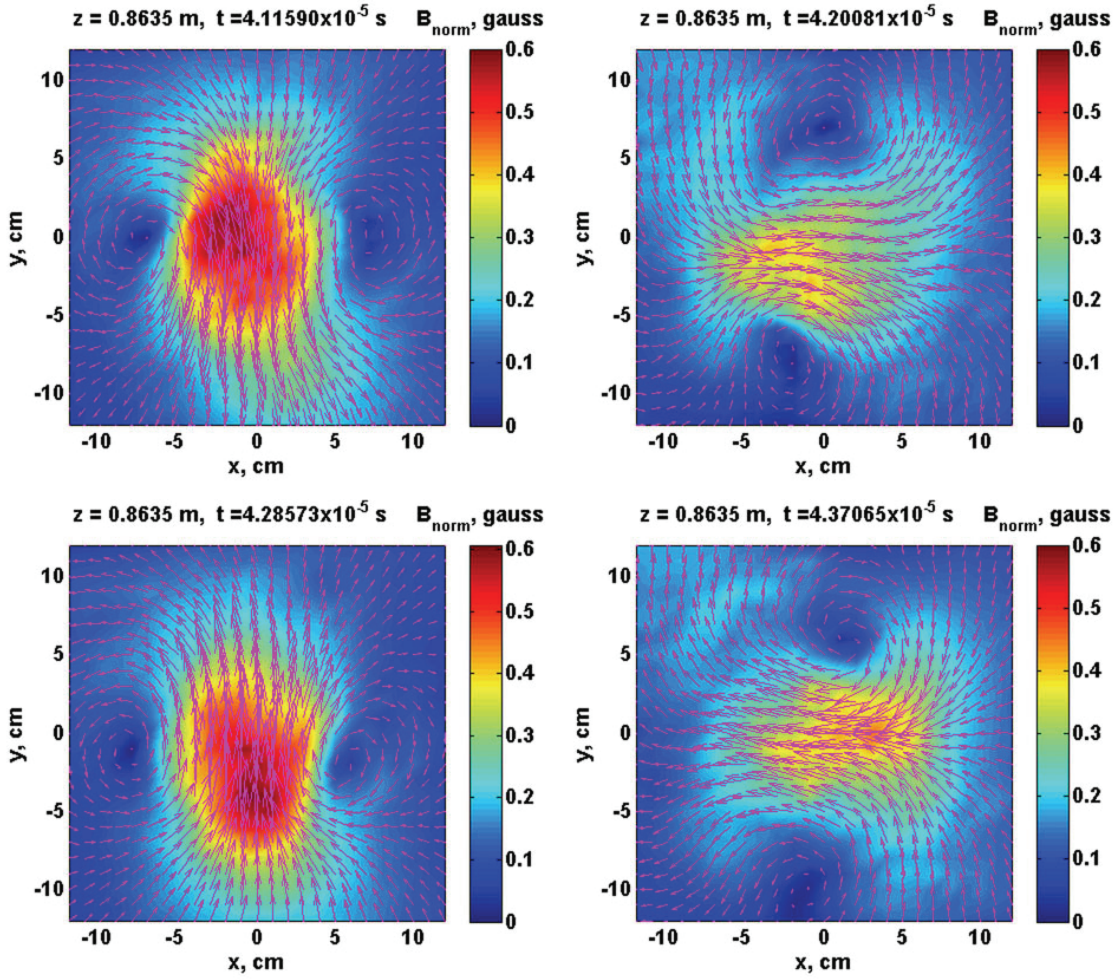

Figure 2.11: Magnetic field structure at the plane perpendicular to the ambient magnetic field lines at the distance $z = 86.35\ cm$ from the radiation source for four different instants of time separated by one quarter of the period ($\mathbf{B}_{norm}$ is the normal to the ambient magnetic field component of the induced magnetic field, arrows represent magnetic field vectors $\mathbf{B}$).

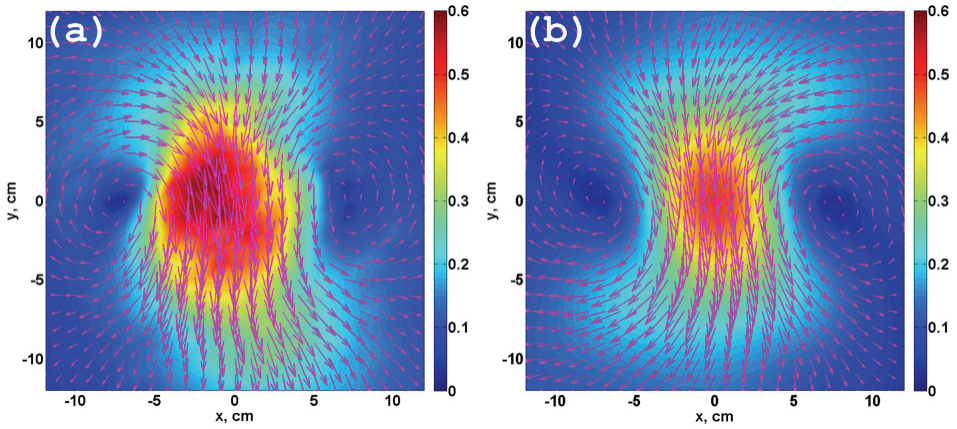

Figure 2.12: Magnetic field structure in the plane perpendicular to the ambient magnetic field lines at the distance $z = 86.35\ cm$ from the radiation source at some instant of time: (a) - measured in the experiment, (b) - 3D linear EMHD calculations (Color palette shows the magnitude of $\mathbf{B}_\perp$ - normal to the ambient magnetic field component of induced magnetic field in $Gauss$)

verse coordinate (c.1)-(c.6) is presented. One can see good overall agreement of the experimental results and the ones calculated using the 3D EMHD model for both the one-loop and two-loop antenna cases. The main feature of the radiation pattern for both cases is that the characteristic size of the spot in the direction transverse to the ambient magnetic field does not depend on the distance from the antenna along the field line, while the amplitude of the wave magnetic field perpendicular to the ambient magnetic field decreases due to energy leakage away from it and due to the effect of collisions. This effect will be discussed later in this Chapter.

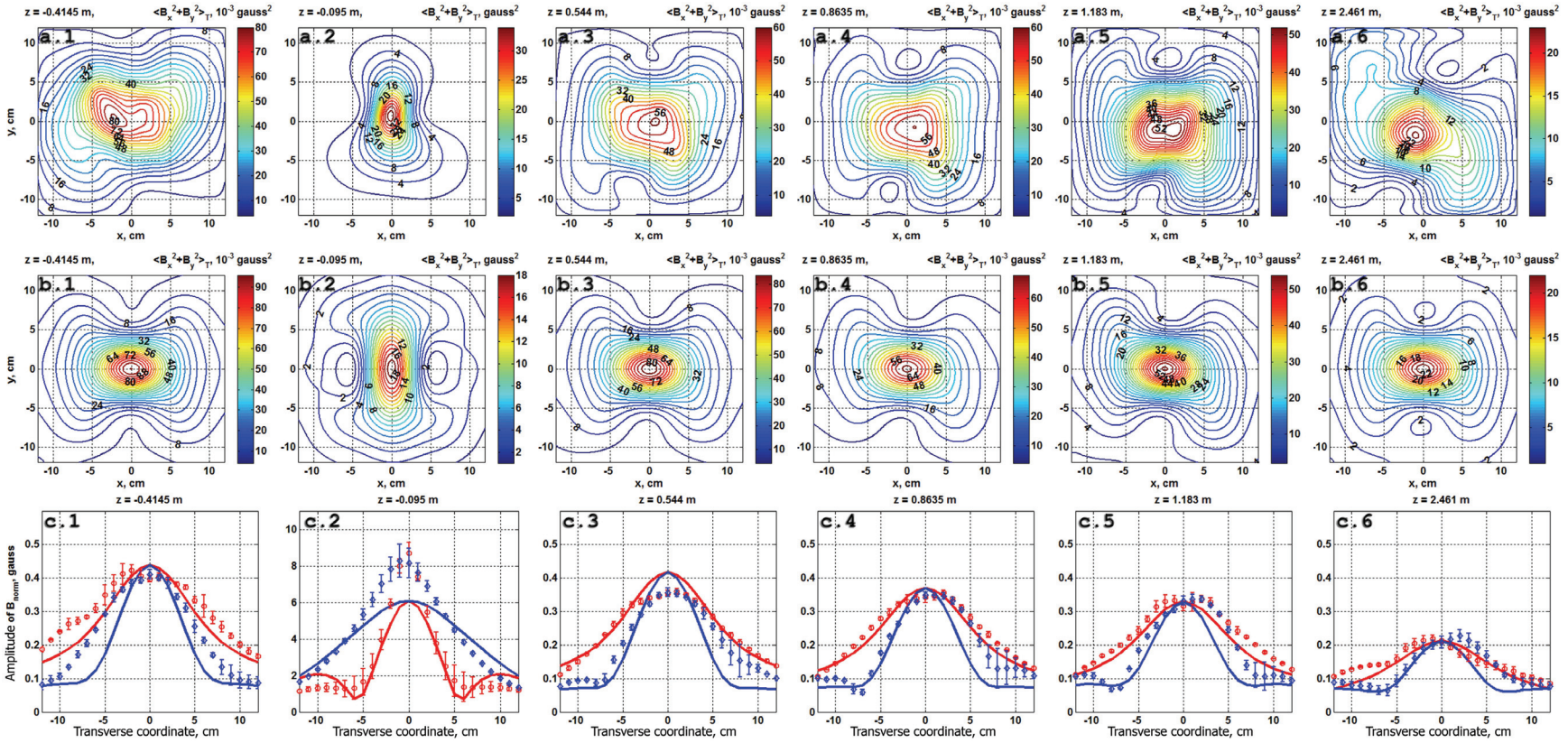

Figure 2.13: The radiation pattern ($\langle B_x^2 + B_y^2 \rangle$ averaged over a period $T = 1/f_D$, that is wave intensity) for one loop case (loop lying in yz plane is turned on). (a.1)-(a.6) - experimental measurements, (b.1)-(b.6) - 3D EMHD model. (c.1)-(c.6) - comparison of experimental and EMHD calculated dependence of the amplitude of the normal component of the induced magnetic field along the transverse axes (dots - experimental measurements, solid lines - EMHD model, red - cross section in x direction, blue - cross section in y direction).

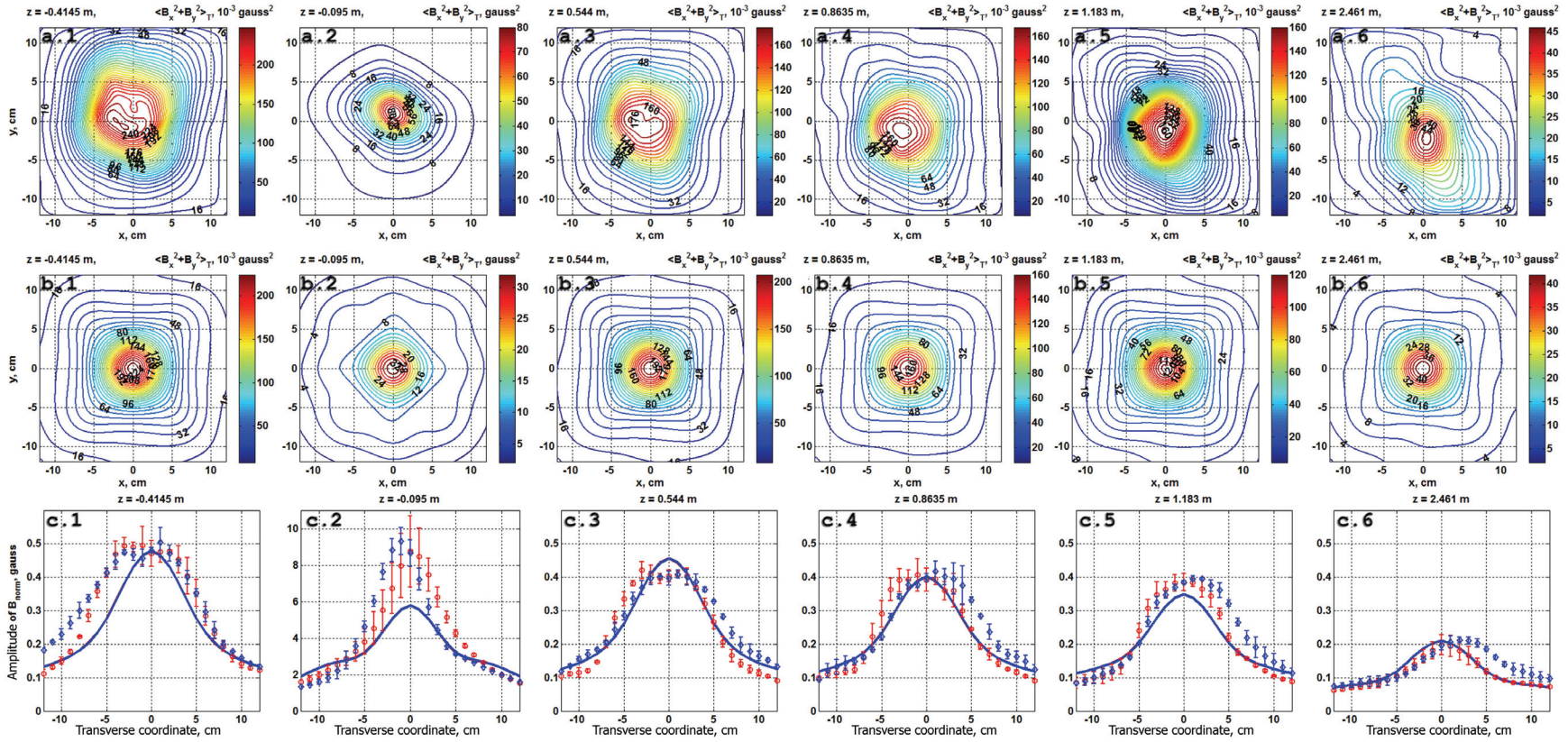

Figure 2.14: The radiation pattern ($\langle B_x^2 + B_y^2 \rangle$ averaged over a period $T = 1/f_D$, that is wave intensity) for two loop case (Right handed rotation of the RMF). (a.1)-(a.6) - experimental measurements, (b.1)-(b.6) - 3D EMHD model. (c.1)-(c.6) - comparison of experimental and EMHD calculated dependencies of the amplitude of normal component of the induced magnetic field along the transverse axes (dots - experimental measurements, solid lines - EMHD model, red - cross section in x direction, blue - cross section in y direction).

In Fig. 2.15 the dependence of the amplitude of the normal to the ambient magnetic field component of the induced magnetic field calculated using the EMHD model on the distance from the antenna along the z-axis is compared with the experiment (a) and fitting functions (b). The best agreement between the EMHD calculations and the experimental measurements were obtained for the effective collision frequency $\nu = 0.007\Omega_{ce} \approx 6.2 \times 10^6 s^{-1}$. Also in the Fig. 2.15 (a) and (b) the dependence of the amplitude of the induced magnetic field for the non-dissipative case is presented. For the non-dissipative case the amplitude dependence on the distance from the source z for $z > 0.5\ m$ was found that to be $\sim 1/\ln(az + b)$, indicates a very slow decay rate compared, for example, to $1/z$. This slow decay rate distinguishes the generation of the whistler waves by magnetic dipoles and the RMF source antennas from the generation of whistler waves by an electric dipole antenna, which has been studied by many authors theoretically, experimentally, and numerically [13, 76, 77, 79, 81, 88, 92, 93]. It was clearly demonstrated in Ref. [76] that small amplitude whistler waves driven by an electric dipole antenna decay very rapidly along the ambient magnetic field even for collisionless plasmas. This is due to the fact that the energy radiated is nearly evenly distributed inside the resonance cone. In order to force the self-ducting of the whistler waves along the abient magnetic field it is necessary to drive fairly large amplitude waves, which are able to modify the plasma itself due to non-linear wave-particle interaction. In our case of the whistler waves generated by the magnetic dipole and the RMF antennas, the amplitude of the induced magnetic field is small compared to the ambient magnetic field. Moreover, the model described in Appendix A is purely linear, and the plasma density

uniform. Nevertheless, we are able to generate a wave in which almost all the energy is guided along the ambient magnetic field, and only small portion of it goes to the periphery. The guided propagation of the wave energy gives the observed slow decay rate of the amplitude of the induced magnetic field along the ambient magnetic field. This efficient energy transfer is possible because of significant field aligned plasma currents. This feature becomes more important for the circularly polarized whistler wave generated by the RMF source. This means that we are able to create an induced magnetic field minimal attenuation in the case of collisionless space plasmas. For the dissipative case with effective collision frequency $\nu = 0.007\Omega_{ce}$, the best fit is with a function $\sim \exp(-z/d) / \ln(az + b)$ with characteristic decay distance $d = 3.704\ m$.

Although the overall agreement between the experimental measurements and the EMHD model results is good, the difference at the plane closest to antenna ($9.5\ cm$) is significant. At this location the model yields amplitudes nearly half of the experimental values. The reason for this is the way the simulation code is implemented. As one can see from Fig. 2.15 in the region close to the antenna the amplitude decays very fast from $\sim 10\ Gauss$ to $\sim 0.5\ Gauss$ at $10\ cm$ distance, and thus its spectrum has very high harmonics. But in our model we are forced to reduce the number of harmonics in the Fourier domain which is determined by the grid size.

Using the parameters of the experiment such as gas pressure, temperature of neutrals, electrons, and ions and plasma density we can estimate the effective electron-neutral ν_{en} and electron-ion ν_{ei} collision frequencies. For electron-neutral

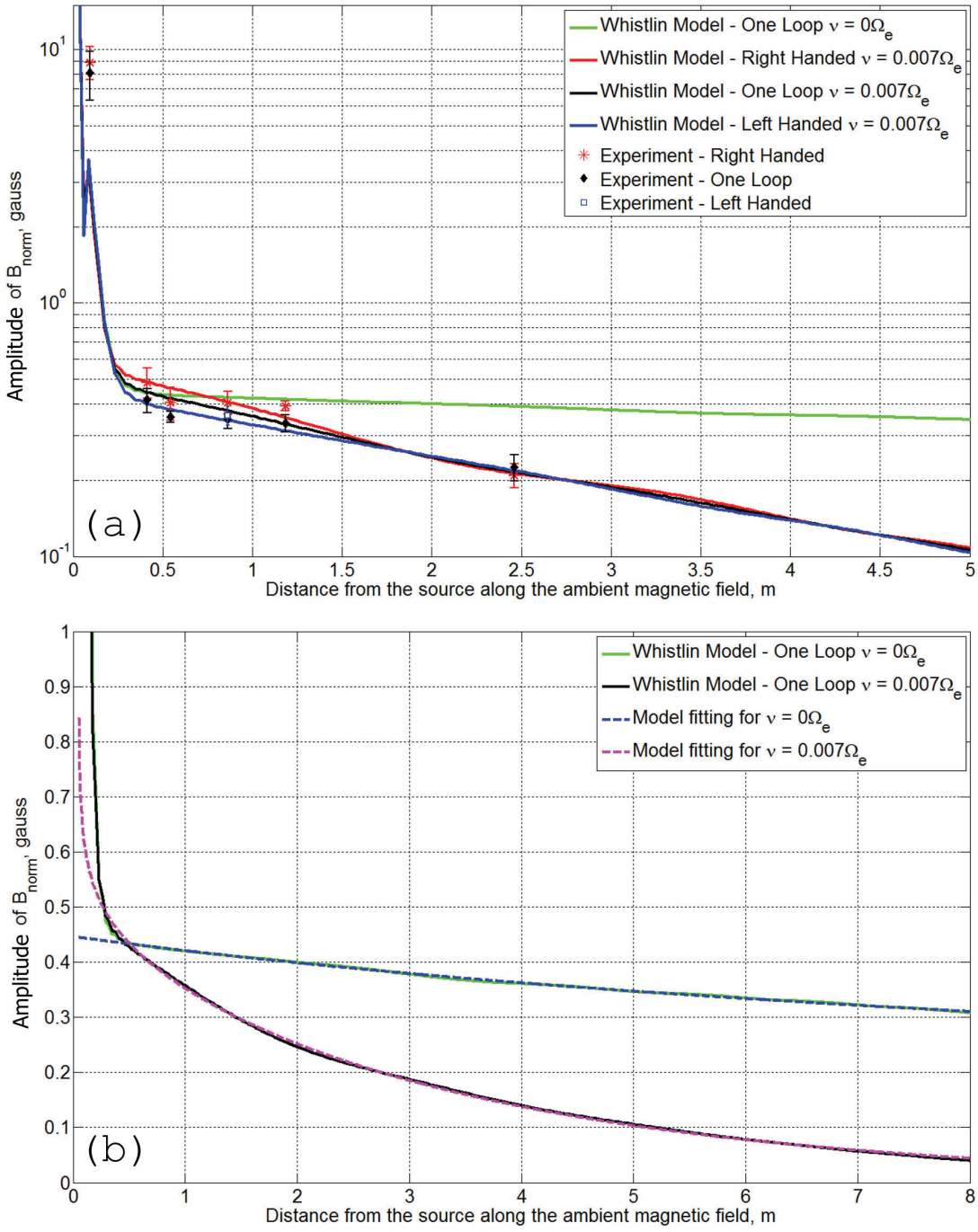

Figure 2.15: Dependence of the amplitude of the component normal to the ambient magnetic field of the induced magnetic field along the horizontal axis: (a) comparison of the EMHD model with the experiment, (b) fitting of the EMHD model results by a functions $\sim 1/\ln(az+b)$ for collisionless case ($\nu = 0$) and $\sim \exp(-z/d)/\ln(az+b)$ for the collisional case ($\nu = 0.007\Omega_{ce}$).

collision frequency the empirical formula from Ref. [10] gives $\nu_{en} \approx 5.6 \times 10^4 s^{-1}$, which is two orders of magnitude lower than the collision frequency in the model. For electron-ion collision frequency the estimate [8] is $\nu_{ei} \approx 5.8 \times 10^6 s^{-1}$, which is very close to the value $\nu = 0.007\Omega_{ce} \approx 6.2 \times 10^6 s^{-1}$ obtained from EMHD model for the best match with the experimental measurements. This implies that, the experimental results along with the 3D EMHD model can be used to estimate the electron collision frequency.

2.4 Whistler wave dispersion relation with finite perpendicular wave number

In this section the properties of the whistler wave dispersion relation with finite perpendicular wave-number are discussed. For the experimental parameters the plasma $\beta = nk_BT/(B_0^2/2\mu_0) \sim 10^{-3} \ll 1$ and thus cold magnetized fluid model approach is applicable. The general dispersion relation from the cold fluid model is [78]

$$\tan^2\theta = \frac{n_\perp^2}{n_{||}^2} = -\frac{P\left(n^2-R\right)\left(n^2-L\right)}{\left(Sn^2-RL\right)\left(n^2-P\right)}, \tag{2.1}$$

where θ is the angle between the direction of the ambient magnetic field $\mathbf{B}_0$ and wave vector $\mathbf{k}$, $\mathbf{n} = c\mathbf{k}/\omega$, $n_\perp = ck_\perp/\omega$, and $n_{||} = ck_{||}/\omega$, where $k_\perp$ and $k_{||}$ are the components of the wave number normal and parallel to the ambient magnetic field ($k_\perp = k\sin\theta$, $k_{||} = k\cos\theta$). The terms R, L, P, S are given by

$$R = 1 - \sum_s \frac{\omega_{ps}^2}{\omega^2} \frac{\omega}{\omega + i\nu_s + \Omega_{cs}}, \tag{2.2a}$$

$$L = 1 - \sum_s \frac{\omega_{ps}^2}{\omega^2} \frac{\omega}{\omega + i\nu_s - \Omega_{cs}}, \tag{2.2b}$$

$$P = 1 - \sum_s \frac{\omega_{ps}^2}{\omega^2} \frac{\omega}{\omega + i\nu_s}, \tag{2.2c}$$

$$S = \frac{R + L}{2}, \tag{2.2d}$$

where s denotes sum over all species (electrons and Helium ions in our case), ω_{ps}, Ω_{cs}, and ν_s are the plasma, cyclotron, and effective collision frequencies of the specie s, respectively. Resolving Eq. (2.1) with respect to n^2 we get

$$n_{1,2}^2 = \frac{\left(PS\left(1 + \cos^2\theta\right) + RL\sin^2\theta\right) \pm \sqrt{\left(PS - RL\right)^2 \sin^4\theta + P^2\left(R - L\right)^2 \cos^2\theta}}{2\left(S\sin^2\theta + P\cos^2\theta\right)} \tag{2.3}$$

as a function of the wave vector direction. Setting the parameters used in the experiment, we get the relation between the longitudinal wave number $k_{||}$ and the transverse wave number $k_\perp$ (See Fig. 2.16).

We first consider the collisionless plasma case ($\nu_S = 0$). For whistler wave mode neglecting the ion motion, the dispersion relation Eq. (2.1) reduces to the quasi-longitudinal whistler wave dispersion relation Eq. (A.42). The EMHD model relation is represented by the blue solid line in Fig. 2.16. The presence of ion motion modifies the whistler wave refraction index surface. Particularly, for the experimental frequency $\omega = 0.002093\Omega_{ce}$ the relation between the longitudinal $k_{||}$ and transverse $k_\perp$ wave numbers behaves fundamentally differently (red solid line

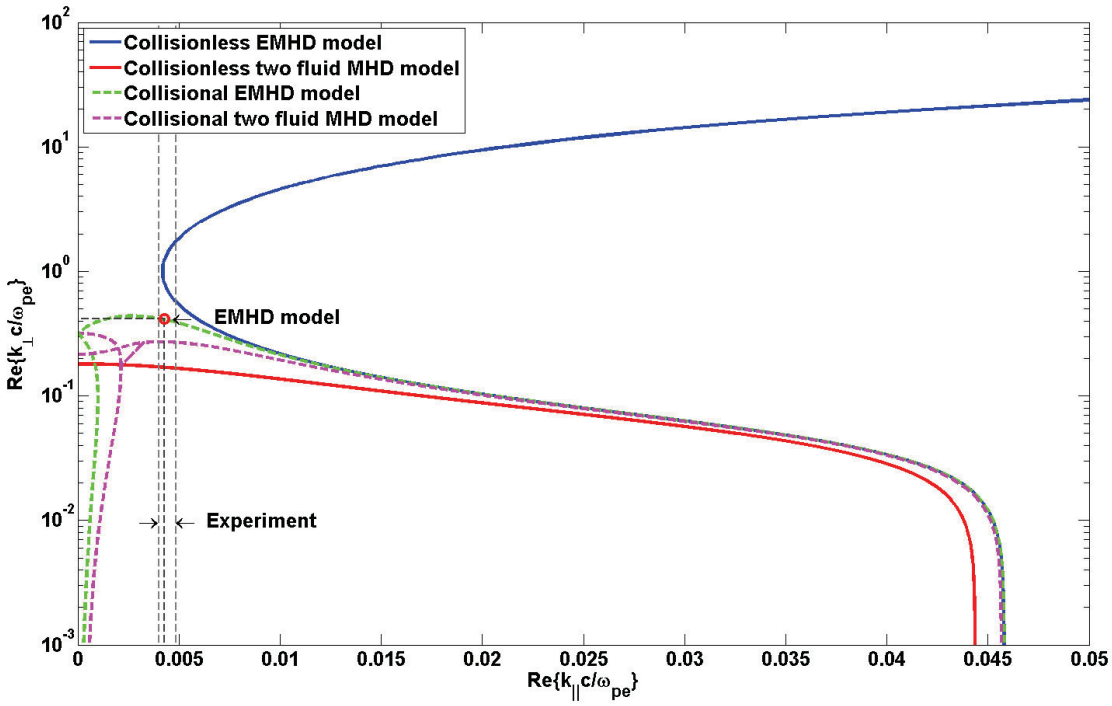

Figure 2.16: Relation of the transverse wave number $k_\perp$ to the longitudinal wave number $k_{||}$ for the whistler wave with frequency $\omega = 0.002093\Omega_{ce}$ (used in the experiment).

in Fig. 2.16). For the experimental frequency in the two fluid model the transverse wave number $k_\perp$ has a cutoff above which the whistler wave mode is evanescent, while in the EMHD model the refractive index surface is unbounded. It has been shown [54, 94] that the frequency which separates these two regimes is the lower-hybrid resonance $\omega_{LH} = \sqrt{\Omega_{ci}\Omega_{ce}} = 1.03 \times 10^7\ s^{-1}$. Moreover, the EMHD model is applicable to the collisionless cold plasma only if the driving frequency ω is well above the lower hybrid resonance ω_{LH} [54]. In our case the experimental driving frequency ω lies below the ω_{LH}, and, in general, the EMHD approach is not applicable. However, the inclusion of the finite effective collision frequencies ν_s in Eq. (2.1)

changes the picture.

We estimated the the collision frequencies for the electrons to be $\nu_{en} \approx 5.6 \times 10^4\ s^{-1}$ (electron-neutral collisions) and $\nu_{ei} \approx 5.8 \times 10^6\ s^{-1}$ (electron-ion collisions). The experimental parameters yield the ion-neutral collision frequency order of $10^2\ s^{-1}$. Thus, for both species, electrons and ions, the collisions are dominated by the Coulomb collisions. Strictly speaking, the dispersion relation Eq. (2.1) is not valid because of the rate of momentum exchange between the two species, and more accurate expressions should be used. However, to a first approximation the effect of ion-electron collisions in the two fluid model could be included by using as the effective ion collisions rate the value $\nu_i = (m_e/m_i)\,\nu_{ei}$ in Eq. (2.1) [37]. Using this value of the collision frequency we find the relation of the real parts of longitudinal and transverse wave numbers in the EMHD (green dashed line in Fig. 2.16) and collisional two fluid (magenta dashed line in Fig. 2.16) models. One can see that bellow a certain transverse wave number the dispersion relations from all three models, *viz.* the collisionless EMHD, the collisional EMHD, and the collisional two fluid model, essentially yield the same mode. From the simulations we found the longitudinal wave number to be $k_{||} = 0.2312\ m^{-1}$ ($\lambda_{||} = 27.18\ m$), which corresponds to a transverse wave number $k_{\perp} = 22.40\ m^{-1}$ ($\lambda_{\perp} = 28.05\ cm$) on the collisional EMHD dependence (red circle in Fig. 2.16). This transverse wave length is two times the distance between the vortices in the field structure corresponding to the field aligned currents. This result does not depend on the driving frequency ω or the distance from the antenna along the ambient magnetic field, but is determined by the size of the antenna. We did a series of simulations using the 3D EMHD model with

varying diameters of the antenna loops, and found that the distance between the vortices in the magnetic field structure (which is half of the transverse wave-length $\lambda_\perp/2$) is roughly the size of antenna, to within a couple of electron skin-depths. Again I emphasize here that the distance between two vortices in the wave picture corresponding to the field aligned plasma currents does not depend on the distance from the antenna along the ambient magnetic field. The range of the experimentally measured longitudinal wave length $\lambda_{||} = 23.8 - 29.0\ m$ corresponds to the transverse wave length $\lambda_\perp \approx 42\ cm$ in the frames of the two-fluid MHD model, which is 1.5 times larger than the value in the frames of the EMHD model.

In Fig. 2.17 the dispersion relation for $\lambda_\perp = 28.05\ cm$ is presented. The solid black line represents the analytic dispersion relation (A.42) in the collisionless limit. The green dashed line represents the analytic dispersion relation in the EMHD model taking into account the finite collision frequency $\nu_e = 0.007\Omega_{ce}$. Results of the 3D EMHD modeling (blue circles and blue pentagram) lie on top of the theoretical curves. The experimental point (red diamond) is also in good agreement with the analytic dispersion relation.

2.5 Wave structure from the dispersion relation

In this section some general properties of the dispersion relation (A.42) and the corresponding wave structures generated by magnetic loop and RMF antennas in three dimensions are presented. First of all the effect of finite transverse wave number $k_\perp$ makes the dispersion relation (A.42) very different from the well-known

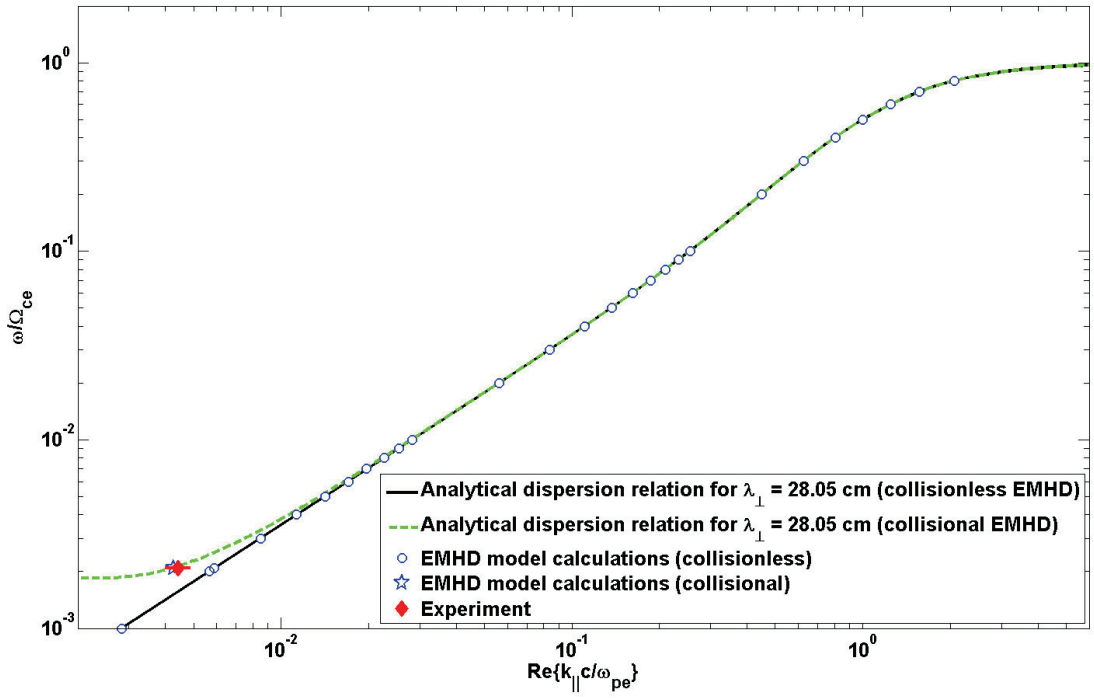

Figure 2.17: Comparison of analytical dispersion relation, EMHD model calculations and the experiment for $\lambda_\perp = 28.05\ cm$.

dispersion relation (A.43) for the plane whistler wave propagating along the ambient magnetic field with zero $k_\perp$. For example, in the three dimensional case, whistler waves generated by a finite size antenna can have a polarization different from the plane whistler wave with zero $k_\perp$ (which is right-handed circularly polarized).

In Fig. 2.18 the dependence of $k_\perp$ on $k_{||}$ given by Eq. (A.42) for frequency $\omega = 0.05\Omega_{ce}$ is presented. The main feature of the dependence is that above the value ~ 0.1 and below ~ 0.225 for every $k_{||}$ there are two corresponding values of $k_\perp$. That is, for the same $k_{||}$, two waves with different $k_\perp$ can be generated. The vertical solid line in Fig. 2.18 represents the longitudinal wave number $k_{||}$ found using the

3D EMHD model for the frequency $\omega = 0.05\Omega_{ce}$ and the current loop diameter $\sim 4.9d_e$. For this longitudinal wave number $k_{||}$ there are two corresponding transverse wave numbers (blue circles). The lowest of them corresponds to the distance $\sim 14.0\ cm$ between the centers of two vortexes in the magnetic field structure (See Fig. 2.11 and 2.12), corresponding to the field aligned plasma currents.

The relationship of $k_{||}$ to $k_{\perp}$ determines the direction of the wave vector $\mathbf{k}$, which is the direction of the phase velocity. The angle between this wave vector $\mathbf{k}$ and the z-axis is 85.13^o and the corresponding wave front has slope 4.87^o with respect to the z-axis. In Fig. 2.19 the dependence of the B_x component (perpendicular to the plane of the picture) of induced magnetic field in the plane containing the current loop for the driving frequency $\omega = 0.05\Omega_{ce}$ is presented. One can see the two wave structure of the whistler wave exited by the finite size antenna. Both waves share the same longitudinal wave number $k_{||}$, but they have different transverse wave numbers $k_{\perp}$ determined by the dispersion relation (A.42). The wave vector corresponding to higher transverse wave number $k_{\perp}$ is shown and has angle 85.13^o with respect to the z-axis.

In Fig. 2.20 the plasma current structure in the plane containing the loop with the current, corresponding to the wave shown in Fig. 2.19, is presented. The colors show the J_x component of the plasma current and the black curves represent plasma current flow-lines in the plane of the picture. Again one can see the two wave structure of the excited whistler wave in the plasma current structure. It should, furthermore, be emphasized that in Fig. 2.20 the dominant plasma current is concentrated near the z-axis, and the width of the current loops on the symmetry

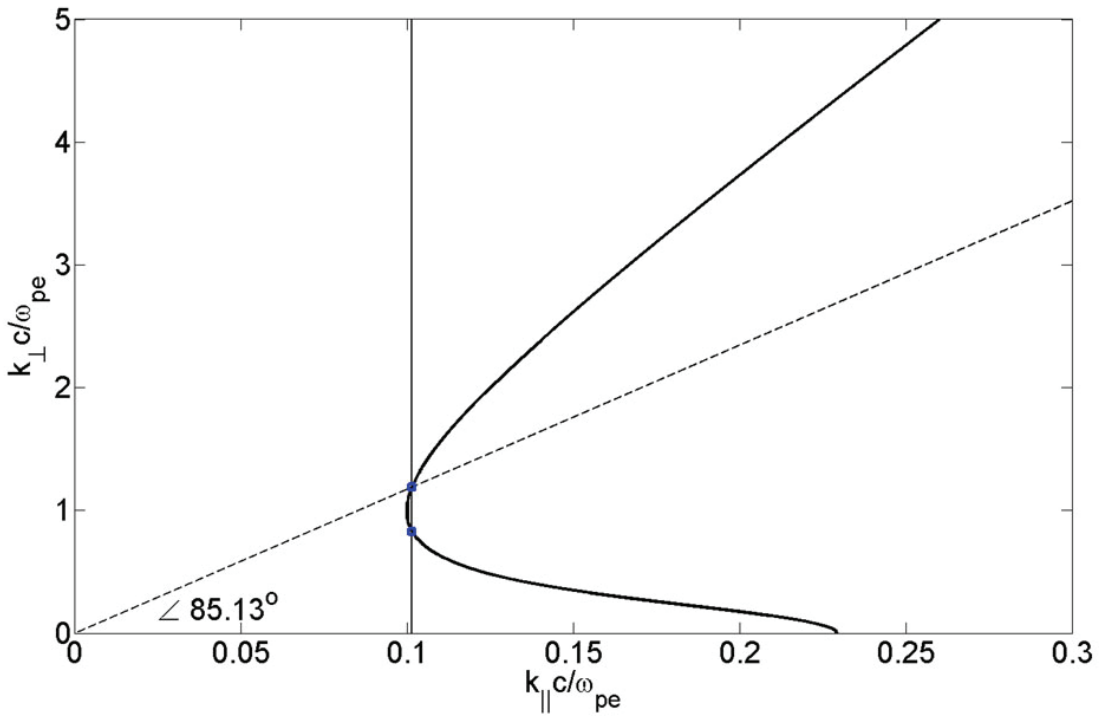

Figure 2.18: Dependence of the transverse wave number $k_\perp$ on on the longitudinal wave number $k_{||}$ for frequency $\omega = 0.05\Omega_{ce}$.

axis does not change with the distance from the antenna. The plasma current forms a chain-like structure whose characteristic size (that is, the transverse wave length) is determined by the size of the antenna, and does not depend on the distance from the antenna along the ambient magnetic field line. The maxima of the field aligned currents correspond to the centers of the vortices in the magnetic field structure in the plane perpendicular to the ambient magnetic field. The length of the "chain segments" is determined by the dispersion relation (A.42) and becomes longer when the driving frequency ω decreases. In the case of the two-loop antenna generating the RMF this chain structure has right or left handed helicity depending on the phase difference in the antenna currents. So the major part of the plasma current

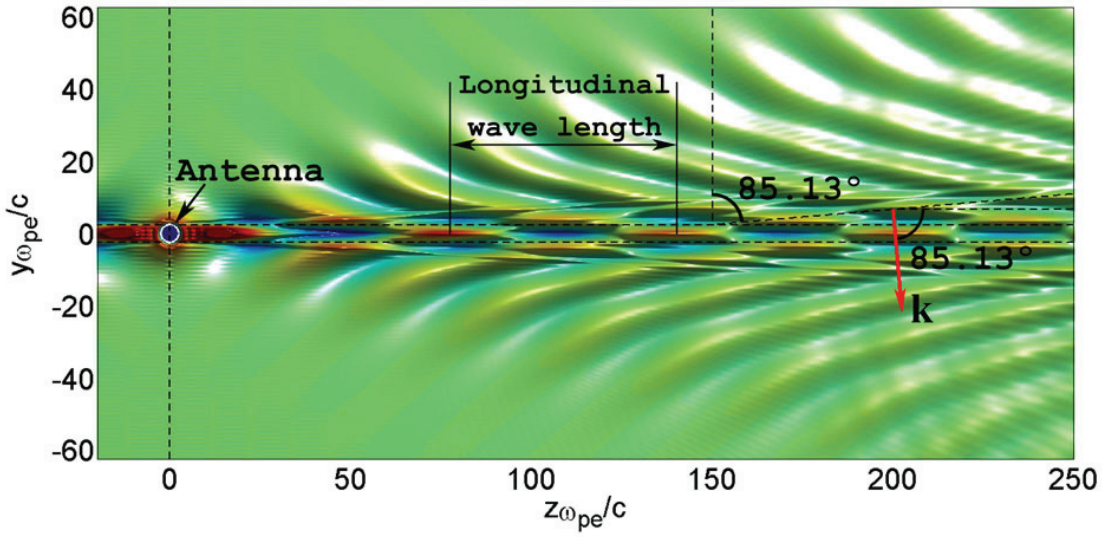

Figure 2.19: B_x component (perpendicular to the plane of the picture) of the induced magnetic field in the plane containing the loop with the current (ring at the origin) for the frequency $\omega = 0.05\Omega_{ce}$.

is field aligned and well confined by the ambient magnetic field. It explains the very slow decay rate of the whistler waves generated by the magnetic dipole and the two-loop antennas.

2.6 Difference between the one-loop antenna and the two-loop RMF source cases

In this section the difference between the whistler waves generated by the one-loop antenna and the two-loop RMF source is discussed. In Fig. 2.21 a distribution of the induced magnetic field component B_{norm} normal to the ambient magnetic field at an instance of time of the whistler wave driven in a collisionless plasma with frequency $\omega = \Omega_{ce}/50$ by one-loop (Fig. 2.21(a)) and two-loop (Fig. 2.21(b))

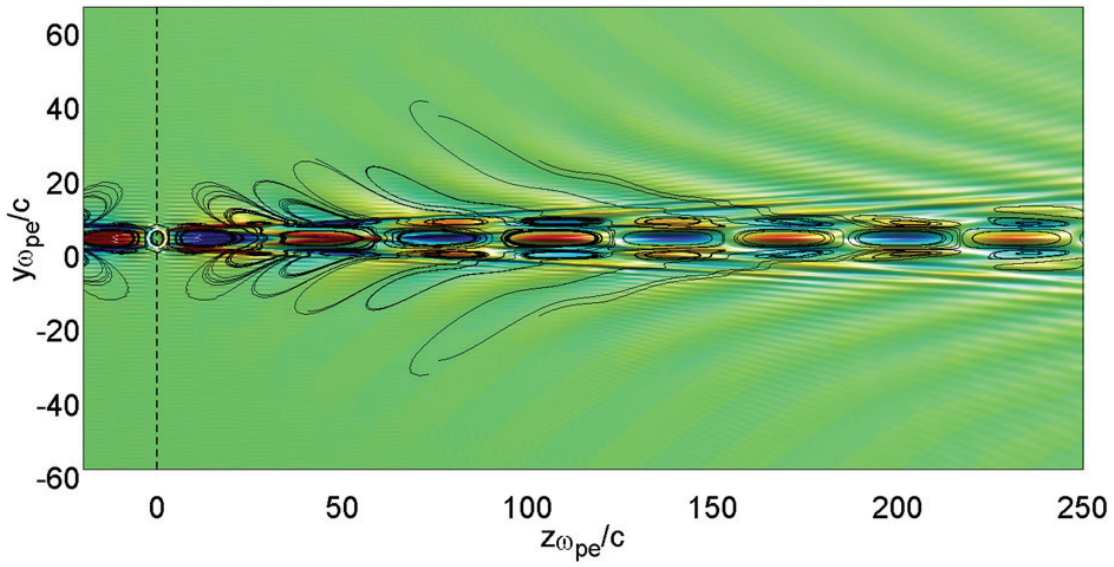

Figure 2.20: Plasma current structure in the plane containing the loop with the current (ring in the origin) for the frequency $\omega = 0.05\Omega_{ce}$ (Color shows J_x component (perpendicular to the plane of the picture) of the current. The black curve lines represent plasma current flow-lines in the plane of the picture (The current flow lines only for the region close to the symmetry axis are shown).

antennas is presented. The insets feature the polarization of the wave in the central symmetry axis. In the one-loop antenna case the polarization is right-handed elliptical, and nearly plane. In the two-loop antenna case the wave is right-handed (or left-handed, depending on the phase difference of the driving currents) circularly polarized. The ellipticity in the one-loop case depends on the driving frequency ω. For low frequencies $\omega \ll \Omega_{ce}$ the ellipticity is nearly 1, and the waves generated by the one-loop antenna have nearly plane polarization. This is consistent with the experiment (See inset on Fig. 2.8(c)). When the frequency increases approaching $\omega = 0.5\Omega_{ce}$ the polarization of the wave generated by the one-loop antenna becomes more circular. One can see that in both the one-loop and two-loop RMF antenna

cases, the wave front is very narrow corresponding to the antenna size, and decays slowly along z-direction due to peripheral leakage of energy. From the simulations it was estimated that the amount of the wave energy inside the central channel within the radius of $\lambda_\perp/2$ relative to all the energy radiated was

$$\epsilon(z) = \frac{\int_0^{\frac{\lambda_\perp}{2}} \rho B^2_{norm}(\rho, z) d\rho}{\int_0^{\infty} \rho B^2_{norm}(\rho, z) d\rho} \tag{2.4}$$

where B_{norm} is the amplitude of the normal component of the wave field. We found that the wave energy which stays within the $\lambda_\perp/2$ radius is of order $75 - 85$ % (depending on the driving frequency) of the entire energy radiated. This means that the magnetic dipole and RMF source antennas are very efficient for transferring radiation along the ambient magnetic field. The other feature that distinguishes the one-loop antenna from the two-loop antenna case is that in the two-loop antenna case the normal component of the induced magnetic field is sufficiently non-zero along the central symmetry axis while in the one-loop antenna case it oscillates in space. This is consistent with the experiment (See Fig. 2.8). This feature is important for the generation of non-local field gradients and non-resonant scattering of energetic particles.

2.7 Conclusion

The concept of a new type of RMF-based antenna/active device for generation whistler waves was demonstrated. We investigated the interactions of the RMF (for the frequency $\Omega_{ci} \ll \omega \ll \Omega_{ce} \ll \omega_{pe}$) with magnetized plasma in experiments and three-dimensional EMHD simulations. We found very good agreement of the linear

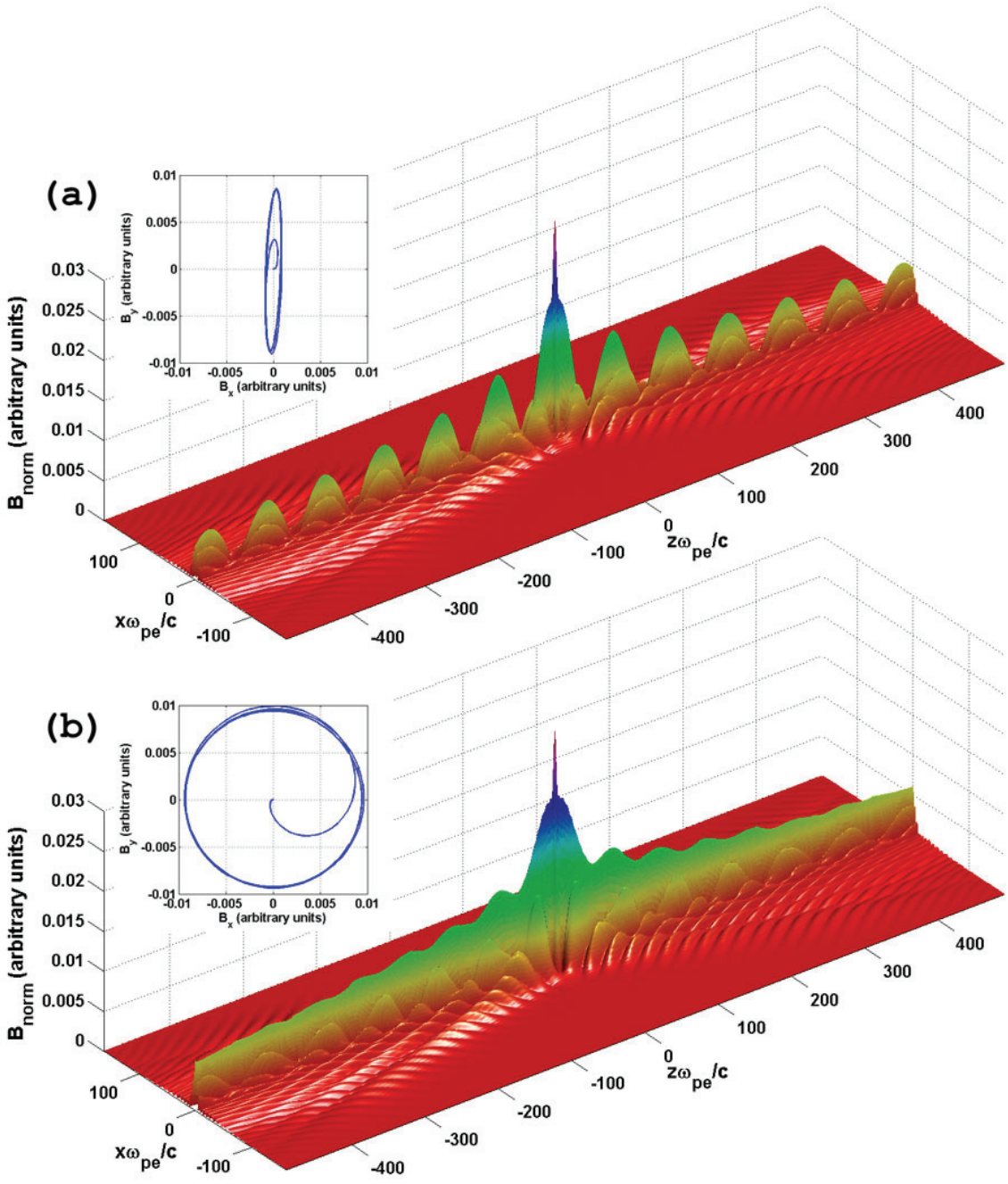

Figure 2.21: Distribution of the normal component of the wave magnetic field for some instance of time generated by one-loop (a) and two-loop antenna with right-handed polarization (b). The one loop antenna lays in xz plane at the origin. The loops of two-loop antenna lay in xz and xy planes at the origin. (Antenna loop diameter - 4.9 electron skin-depth, driving frequency - $\omega = \Omega_{ce}/50$, collisionless case)

3D EMHD model with the experiment, both qualitatively and quantitatively. It was found that whistler waves generated by both the one-loop and two-loop antennas are confined by the ambient magnetic field without requiring non-linear wave particle interaction and/or plasma density ducts. The wave structures generated by the RMF source have significant field aligned plasma currents confined by the ambient magnetic field. This allows an efficient to transfer of the radiation along the ambient magnetic field. In the collisional plasma the wave decay rate is determined by collisions. In the collisionless case very slow decay rate is determined by the leakage of the wave energy from the central axis to the periphery. The whistler wave generated by the RMF has sufficiently non-zero normal component along the central symmetry axis while in the one-loop antenna case the the normal component of the wave magnetic field oscillates along the the ambient magnetic field. The analytic dispersion relation for whistler waves in cold plasmas, Eq. (A.42), is in very good agreement with the results of the 3D EMHD simulations and the experimental measurements. The whistler wave generation by the magnetic dipole along with the 3D EMHD model was used to estimate the effective electron collision frequency in the LAPD experiment.

Chapter 3

Generation of polarized shear Alfvén waves by a rotating magnetic field source

3.1 Introduction

Shear Alfvén wave (SAW) is an electromagnetic mode wave that propagates in magnetized plasmas at frequencies below the ion cyclotron frequency, $\omega < \Omega_{ci}$. The shear Alfvén waves propagate nearly parallel to the ambient magnetic field $\mathbf{B}_0$ with the wave magnetic field $\mathbf{B}$ almost perpendicular to the background $\mathbf{B}_0$, while the wave electric field is nearly perpendicular to both $\mathbf{B}$ and $\mathbf{B}_0$ [31, 38, 40]. In the case of SAWs with finite transverse wave number $k_\perp$, SAWs have small compared to perpendicular $E_\perp$ parallel to $\mathbf{B}_0$ component of the electric field $E_{||}$ ($E_{||} \ll E_\perp$) [31]. The parallel component of electric field provides the SAW with the ability to accelerate electrons and drive field aligned plasma currents. In the direction perpendicular to the ambient magnetic field $\mathbf{B}_0$, the plasma currents of SAWs are carried by ions through their polarization drift [64]. In general the propagation of SAWs across the ambient magnetic field lines is much slower than the field aligned propagation [32,60,61]. As a result, the SAWs are confined by the ambient magnetic field to a fixed range of field lines.

SAWs can be found in a wide variety of magnetized plasma environments.

They have been observed in a number of laboratory experiments [28] and in different magnetized space plasma configurations such as the solar corona [44], Jupiter's [21], and Earth's [59, 87] magnetospheres, *etc.* Because of its field aligned propagation, SAW can transport energy efficiently. SAWs can drive extensive plasma currents. In fact, one can think of almost any low frequency current system in magnetized plasmas as an Alfvénic wave system.

SAWs were observed by satellites, such as FAST [19], Cluster [5] and Helios [44] and are now thought to play a major role in particle acceleration in the auroral zone [41,46], magnetospheric bow shock [5], the solar corona [44], *etc.* Measurements of the incoming Poynting flux of shear waves toward the auroral region ionosphere by the Polar satellite indicate that their energy is sufficient to excite certain types of auroras [96].

There have been many SAW experiments [28], however the basic physics of the interaction of the rotating magnetic field (RMF) with magnetized plasmas in the frequency range below the ion cyclotron frequency Ω_{ci} remains unexplored. The following experimental and theoretical study of the interaction of RMF with magnetized plasma addresses the spatio-temporal structure, properties of the propagation and the dispersion relation of the induced waves as a function of the RMF and plasma parameters.

3.2 Experiments on the generation of shear Alfvén waves by RMF source

Two sets of the experiments on generating of the SAWs by the RMF source were performed on the LAPD [29]. The experimental setup of them was similar to that described in Chapter 2 for the experiments on generating of whistler waves. The general plasma parameters in the experiments performed are presented in Table 3.1. The first experiment [35] was mainly focused on the measurements of the spatiotemporal structure of SAW generated by the RMF source. In that experiment the three components of the induced magnetic field were measured in planes perpendicular to the ambient magnetic field at different z-locations, providing three-dimensional volumetric data of the wave magnetic field and current structures over the course of ~ 2.5 parallel SAW wavelengths for frequency $\omega = 0.54\Omega_{ci}$. The main goal of the second experiment set was measurement of the dependence of the generated wave parameters on the driving frequency. The major difference between the plasma parameters in the two experiments is that in the second setup the plasma density was smaller ($n = 1.3 \times 10^{12} cm^{-3}$ compared to $n = 2.3 \times 10^{12} cm^{-3}$ in the first setup), and the electrons were colder ($T_e = 1.5\ eV$ compared to $T_e = 6\ eV$). As a result in the second experiment we measured higher values of the wave amplitude at the same locations and input current parameters in the second experiment than in the first one.

The RMF source used in the experiment was a phased, orthogonal two loop antenna (See Fig. 3.1) similar to the one described in Chapter 2 The antenna was

Table 3.1: Parameters of the experiment on generating SAW by the RMF source.

Parameter	Experiment set 1 [35]	Experiment set 2
Ions	He^+	He^+
Gas pressure	$\sim 10^{-4}\ Torr$	$\sim 10^{-4}\ Torr$
Ambient magnetic field	$10^3\ Gauss$	$10^3\ Gauss$
Plasma density (microwave interferometer)	$2.3 \pm 0.3 \times 10^{12} cm^{-3}$	$1.3 \pm 0.2 \times 10^{12} cm^{-3}$
Electron temperature	$6 \pm 1\ eV$	$1.5 \pm 0.5\ eV$
Ion temperature (Langmuir probe)	$1 \pm 0.5\ eV$	$0.5 \pm 0.3\ eV$
Electron plasma frequency	$8.6 \times 10^{10} s^{-1}$	$6.4 \times 10^{10} s^{-1}$
Electron skin-depth	$3.5\ mm$	$4.7\ mm$
Electron cyclotron frequency	$1.76 \times 10^{10} s^{-1}$	$1.76 \times 10^{10} s^{-1}$
Ion cyclotron frequency	$2.4 \times 10^{6} s^{-1}$	$2.4 \times 10^{6} s^{-1}$
Electron-neutral collision frequency [10]	$2.8 \pm 0.2 \times 10^{5} s^{-1}$	$8.9 \pm 0.1 \times 10^{4} s^{-1}$
Ion-neutral collision frequency	$\sim 10^{2} s^{-1}$	$\sim 10^{2} s^{-1}$
Coulomb collision frequency [8]	$4.75 \pm 1.15 \times 10^{6} s^{-1}$	$1.75 \pm 0.4 \times 10^{7} s^{-1}$

composed of two independent coils of 0.25 cm diameter solid copper wire with three turns each. The diameter of the coils were roughly 8 cm and 9 cm, corresponding to $\sim$ 23 and $\sim$ 26 electron skin-depth $\lambda_e = c/\omega_{pe}$ (ω_{pe} is the electron plasma frequency) for the first experimental parameters. The coils were driven by two independent high power resonant LRC circuits utilizing the inductance of the antenna and the inherent line resistance, whose resonance frequencies can be adjusted with the capacitance in a matched circuit, set $\pm 90^o$ out of phase. Thus, the total magnetic moment generated by the two coils could have left-handed or right-handed circular polarization. The antenna was oriented with its center located on the symmetry axis of the LADP-machine, and one of the loops lying in the xz-plane, while the second in the yz-plane. The coordinate system was oriented with the z-axis along the ambient magnetic field (the central axis of the machine) and the y-axis

pointing upwards. The driving frequency used in the experiment was in the range $80 - 355\ kHz\ (0.21 - 0.93 f_{ci})$. The magnitude of the current in the coils was up to $\sim 600\ Amps$.

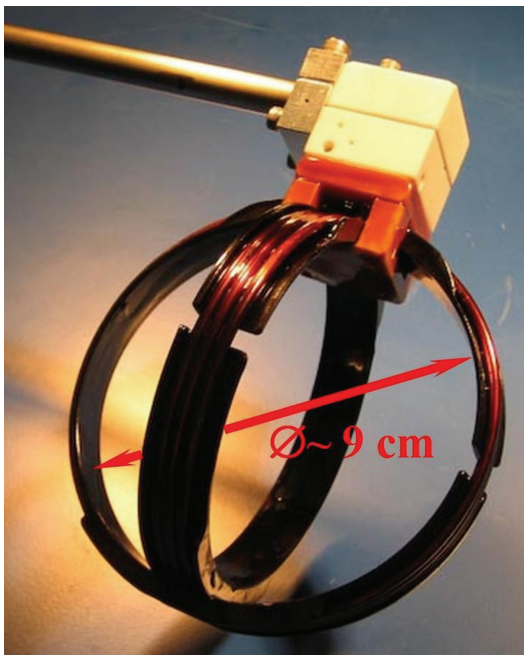

Figure 3.1: The RMF antenna used in the experiment on generating of SAWs. Each coil has three turns of enameled solid copper wire. The outer coil has diameter of $\sim 9\ cm$, and the inner coil has diameter $\sim 8\ cm$.

The primary diagnostic used in the experiment was a three-axis magnetic pickup coil [25]. The probe features differentially wound loops that eliminate electrostatic pickup when used in conjunction with a differential amplifier. The loops of the probe are wound around 1 mm cube with ten turns each. The cube was mounted within a glass tube and attached to a thin ceramic tube extending from the end of a stainless steel probe shaft. Using a computer controlled data acquisition system the measurements of three components of perturbed magnetic field on a square area

41×41 points with 0.75 cm spacing at several cross sectional planes perpendicular to the ambient magnetic field were performed for different driving frequencies and polarizations of the RMF source.

A typical input signal for the right-handed polarization of the RMF source with the frequency $f = 206\ kHz$ is shown in Fig. 3.2(a.1). The induced magnetic field components measured at the central axis of the machine at distance $z = 3.83\ m$ away from the antenna are shown in Fig. 3.2(b.1). Two nearly identical currents with peak magnitude $\sim 600\ A$ with $\pi/2$ relative phase difference were driven in the loops, resulting in the right-handed rotation with respect to the ambient magnetic field of the magnetic momentum of the antenna. To compare the plasma response to the RMF with that of a single loop antenna, experiments were performed with one of the currents turned off (See Fig. 3.3). In both cases of the one-loop and two-loop antennas, the B_z component parallel to the ambient magnetic field of the induced magnetic field was much smaller than the perpendicular components. In the two-loop antenna case a nearly steady value of the perpendicular magnetic field rotates around z-axis counterclockwise, while in the case of the one-loop antenna the normal component $B_{norm} = \sqrt{B_x^2 + B_y^2}$ oscillates and in this case the wave has nearly linear polarization. These features of the waves generated by two-loop and one-loop antennas are shown in Fig. 3.2(b.2) and Fig. 3.3(b.2), respectively.

In Fig. 3.4 the three-dimensional structure of the SAW magnetic field measured in the experiment in nine different planes perpendicular to the ambient magnetic field is shown for the instant $t = 0.06ms$. Each plane consists of $41 \times 41 = 1681$ points. In each location the measurements are averaged over 10 discharges. Thus

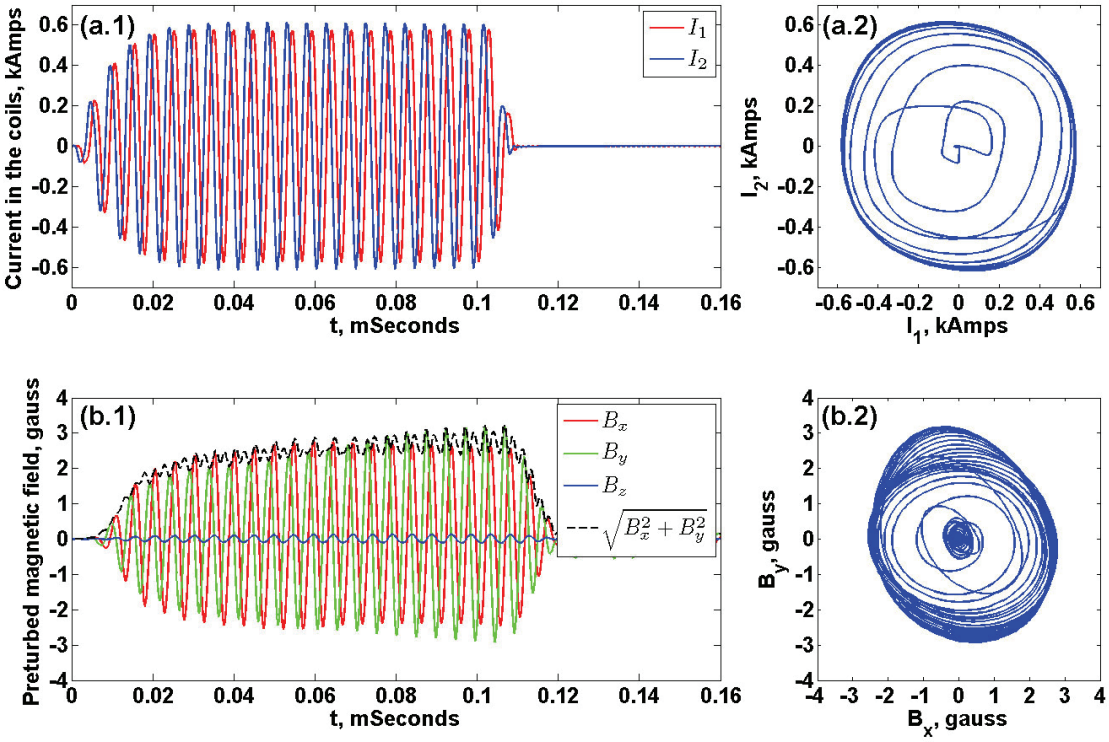

Figure 3.2: Time dependence of input currents (a.1) and induced magnetic field components (b.1) measured on the central axis of the device at the distance $z = 3.83\ m$ away from the antenna for the right-handed polarization at a driving frequency $f_d = 206\ kHz$. The graphs on the right show the hodographs of the input currents (a.2) and B_x, B_y components of the induced magnetic field (b.2).

the data for Fig. 3.4 is collected over the course of more than 150,000 discharges, which is possible because of highly reproducible parameters of the plasma on the device and the computer controlled robotic data acquisition system.

Figure 3.5 illustrates a method used to determine the longitudinal phase velocity $v_{ph||}$ of the SAW generated by the RMF. In order to find $v_{ph||}$ the equal phase points of the perturbed magnetic field components at different z-locations but with the same x and y coordinates were found. It is convenient to use as such equal phase

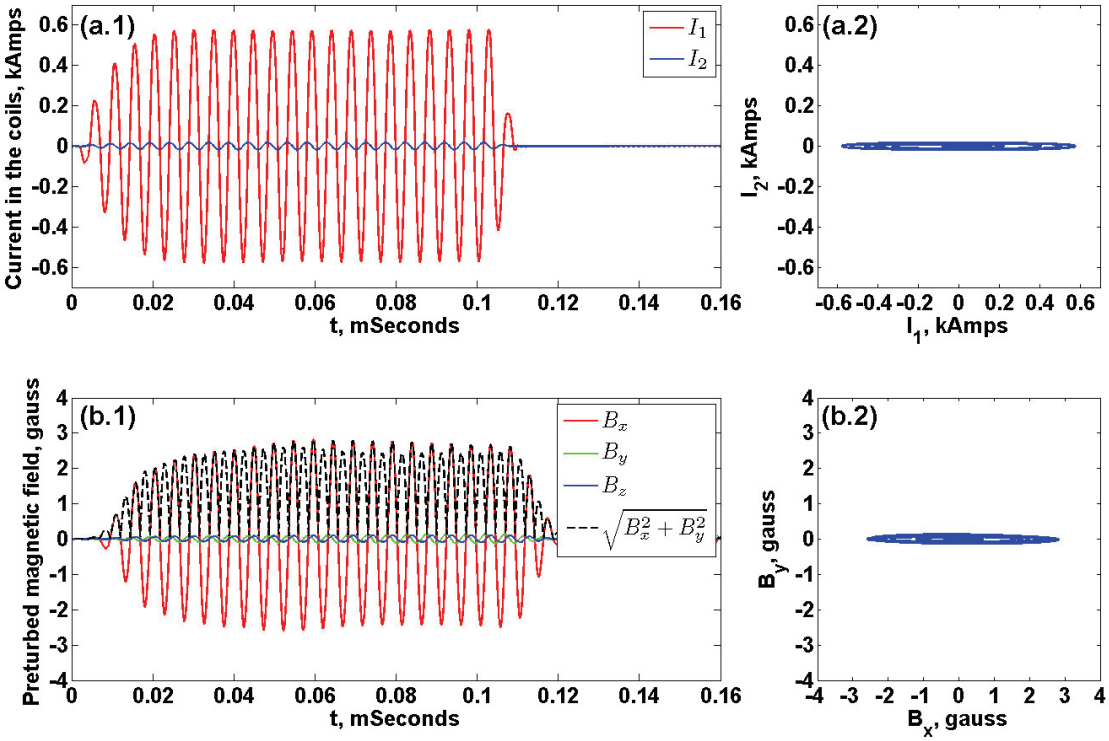

Figure 3.3: Time dependence of input currents (a.1) and induced magnetic field components (b.1) measured at the central axis of the device at distance $z = 3.83\ m$ away from the antenna for single-loop antenna (The loop laying in the xz-plane was turned off). Driving frequency $f_d = 206\ kHz$. The graphs on the right show the hodographs of the input currents (a.2) and B_x, B_y components of the perturbed magnetic field (b.2).

points zeros (black circles in Fig. 3.5) or maxima and minima of the magnetic components.Then these points were fitted with linear functions (inclined dashed lines in Fig. 3.5), whose slope gives the longitudinal phase velocity.

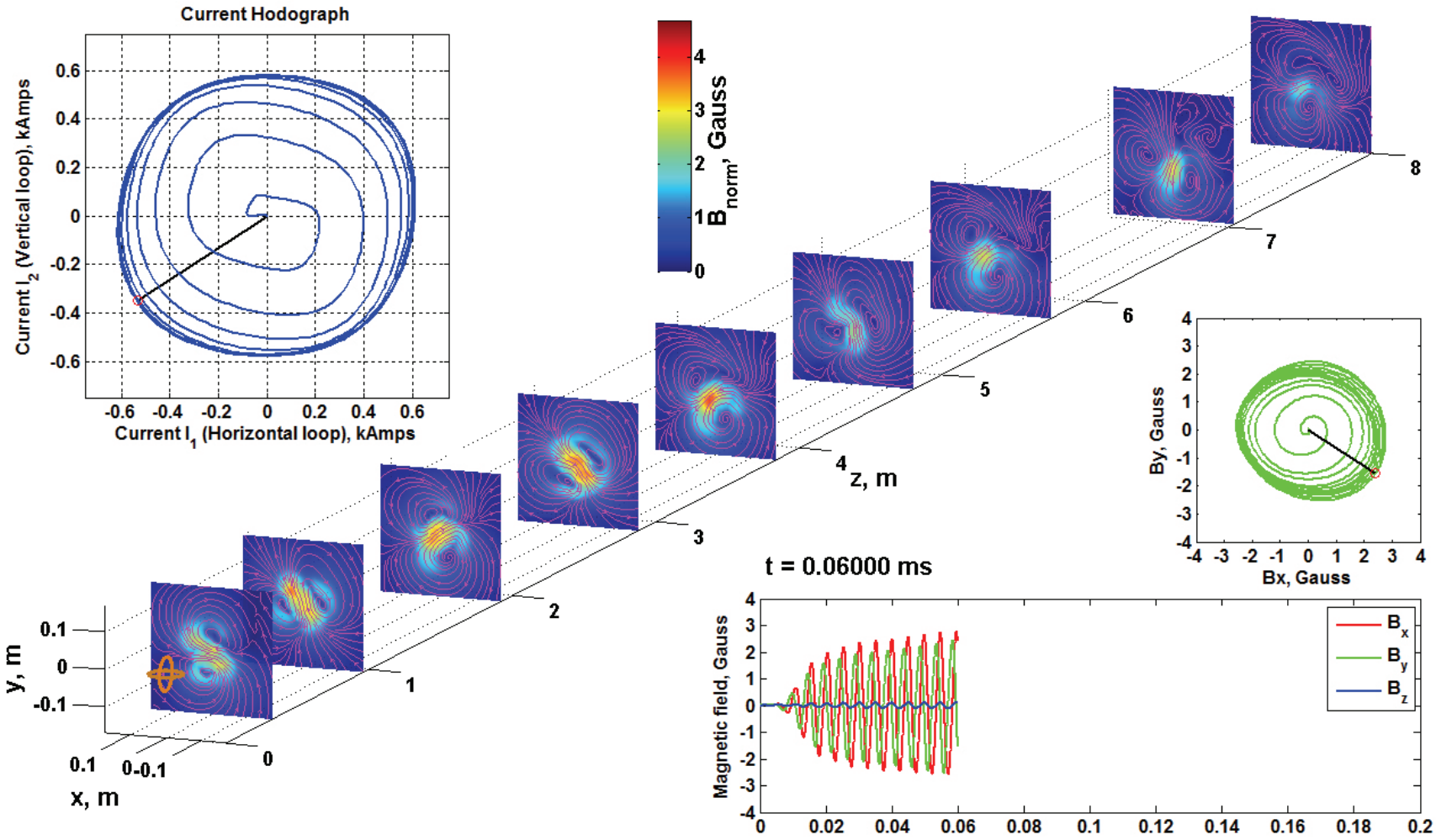

Figure 3.4: The SAW volumetric magnetic field structure measured in the experiment for nine different planes for the instant $t = 0.06\ ms$. The case presented is left-handed polarization of the RMF with driving frequency $f_d = 206\ kHz$. The driving antenna is shown in the origin. The inset in lower right corner shows time series of the wave magnetic field components in the center of the plane $z = 3.83\ m$.

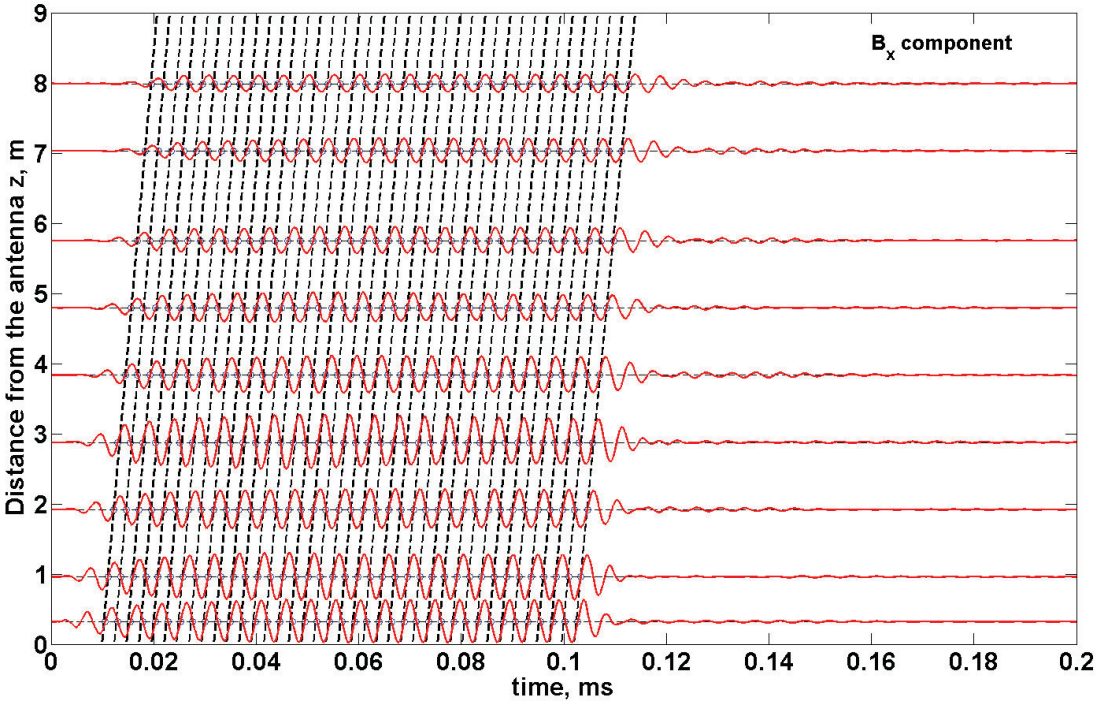

Figure 3.5: An illustration how the longitudinal phase velocity is determined from the experimental measurements. Red lines represent B_x components of the perturbed magnetic field on the central axis of the LAPD machine at different z locations. Black circles represent the points of the equal phases (in this case zeroes of B_x) in different z locations. Inclined dashed lines are linear fit of the equal phases points, whose slope gives the phase velocity.

3.3 Comparison of two magnetized fluid model and the experiment

3.3.1 Magnetic field structure

In the experiments it was found that the RMF source is capable of driving relatively large magnitude field shear Alfvén waves with the peak amplitudes up to $10 - 20$ *Gauss* for input current magnitudes 600 *Amps* with arbitrary polar-

ization. Although the wave field amplitudes were ~ 10 $Gauss$ (a large amplitude for Alfvén waves produced in the LAPD) in absolute value they were only 1 % of the background magnetic field $B_0 = 10^3$ $Gauss$. It has been shown [22] that large enough amplitude SAWs can lead to wave current filamentation and modification of the plasma density due to the ponderomotive force. However, in order for this nonlinear effect to be important the wave magnitude should be of order 10 % or higher of the background magnetic field [22]. In our case of ~ 1 % magnetic field perturbations the linear approximation is justified for a wide range of frequencies, with the exception of narrow frequency regions near resonances, such as the ion cyclotron frequency.

A three-dimensional (3D) cold two magnetized fluid code, described in detail in the Appendix B, was developed and implemented using the MATLAB environment to simulate the experiments with the parameters presented in Table 3.1 and a variable driving frequency. A typical mesh of $180 \times 180 \times 1000$ (32.4×10^6) grid points varying linear sizes of the computational domain was used in the simulations of Alfvén waves generated by the RMF source.

In both the experiments and 3D simulations the observed wave magnetic field generated by the RMF antenna lies primarily in the plane perpendicular to the ambient magnetic field (the magnitudes $B_x \approx B_y \gg B_z$). In the 3D simulations we found that the wave electric field is nearly normal to both the background magnetic field and the induced magnetic field. The wave electric field component perpendicular to the ambient magnetic field is much bigger than the parallel (the magnitudes $E_x \approx E_y \sim 100E_z$), which is consistent with the properties of the kinetic

SAW [31, 38, 40] radiated from a source with small transverse size (that is high perpendicular wave number $k_\perp$) [61].

Figures 3.6, 3.7, and 3.8 show the magnetic field structures in one of the planes perpendicular to the ambient magnetic field measured in the experiment (Experiment set 2) and calculated using 3D two-fluid model for different polarizations of the radiation source. The ambient magnetic field points outwards of the plane of the figures.

In Fig. 3.6(a.1)-(a.5) the induced magnetic field structure measured in the experiment for left-handed polarization of the RMF source at the plane $z = 2.88\ m$ away from the antenna for five different instants of time separated by 1/8 of the wave period (driving frequency $f_d = 80\ kHz$) are presented. Fig. 3.6(b.1)-(b.5) show the same plane magnetic field for the same time instants calculated from the 3D two-fluid model. As the time evolves (from left to right) the magnetic field in the plane rotates clockwise around the ambient magnetic field.

Figure 3.7(a.1)-(a.5) shows the induced magnetic field structure measured in the experiment for case of a one-loop antenna (the current laying in the $x-z$-plane was turned off) for the five different instants of time. Fig. 3.7(b.1)-(b.5) show the magnetic field in the same plane for the same times in Fig. 3.7(a.1)-(a.5) from the simulations. The induced magnetic field has nearly linear polarization in this case, and as the time progresses (from left to right) the magnetic field in the center of the plane oscillates in the x-direction.

Figure 3.8 is similar to Figs. 3.6, 3.7 graphs except the polarization of the RMF source was set to be right-handed. In this case the magnetic field rotates

counterclockwise around z-axis. One can see good agreement of the 3D simulations and the experiment for all the cases. Note also a good agreement of the phase between the model and the experiment, which confirms that parallel phase velocities in the experiment and the simulations are very close.

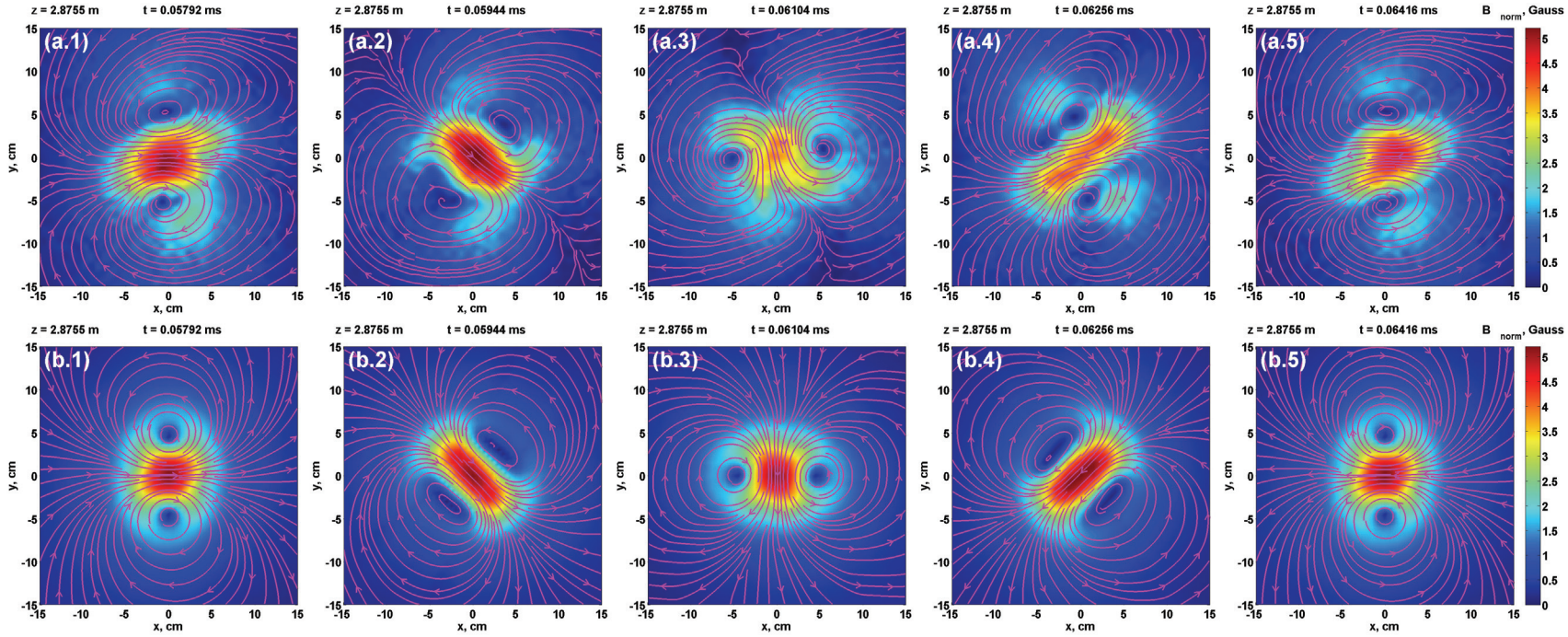

Figure 3.6: Comparison of the magnetic field structure in the plane $z = 2.88\ m$ away from the radiating antenna for five instants of time ($t_1 = 0.05792\ ms$, $t_2 = 0.05944\ ms$, $t_3 = 0.06104\ ms$, $t_4 = 0.06256\ ms$, and $t_5 = 0.06416\ ms$) separated by 1/8 of the wave period (driving frequency $f_d = 80\ kHz$) measured in the experiment (Experiment set 2) ((a.1) - (a.5)) and calculated using 3D model ((b.1) - (b.5)) for the left-handed polarization case. The ambient magnetic field $B_0 = 1000\ Gauss$ points outward of the plane of the picture.

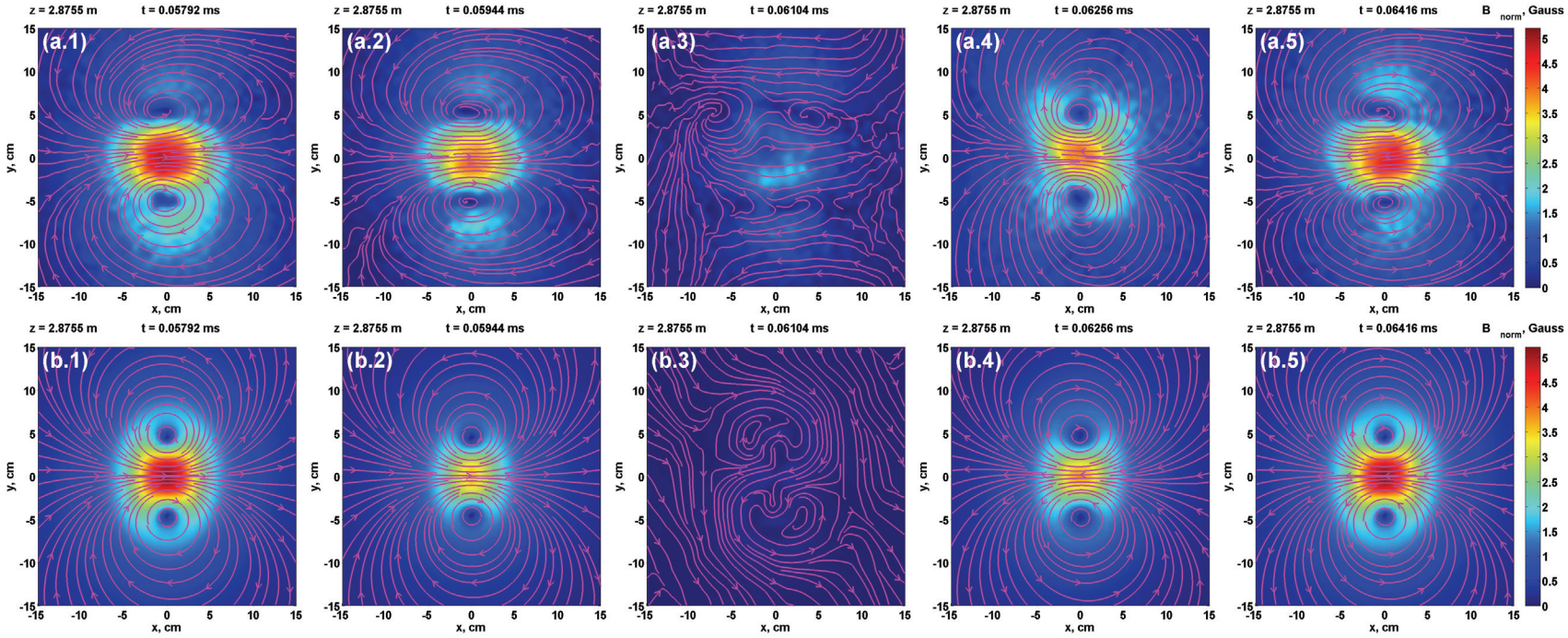

Figure 3.7: Comparison of the magnetic field structure in the plane $z = 2.88\ m$ away from the radiating antenna for five instants of time ($t_1 = 0.05792\ ms$, $t_2 = 0.05944\ ms$, $t_3 = 0.06104\ ms$, $t_4 = 0.06256\ ms$, and $t_5 = 0.06416\ ms$) separated by 1/8 of the wave period (driving frequency $f_d = 80\ kHz$) measured in the experiment (Experiment set 2) ((a.1) - (a.5)) and calculated using 3D model ((b.1) - (b.5)) for single loop antenna case. The antenna loop in the xz-plane is turned off. The ambient magnetic field $B_0 = 1000\ Gauss$ points outwards of the plane of the picture.

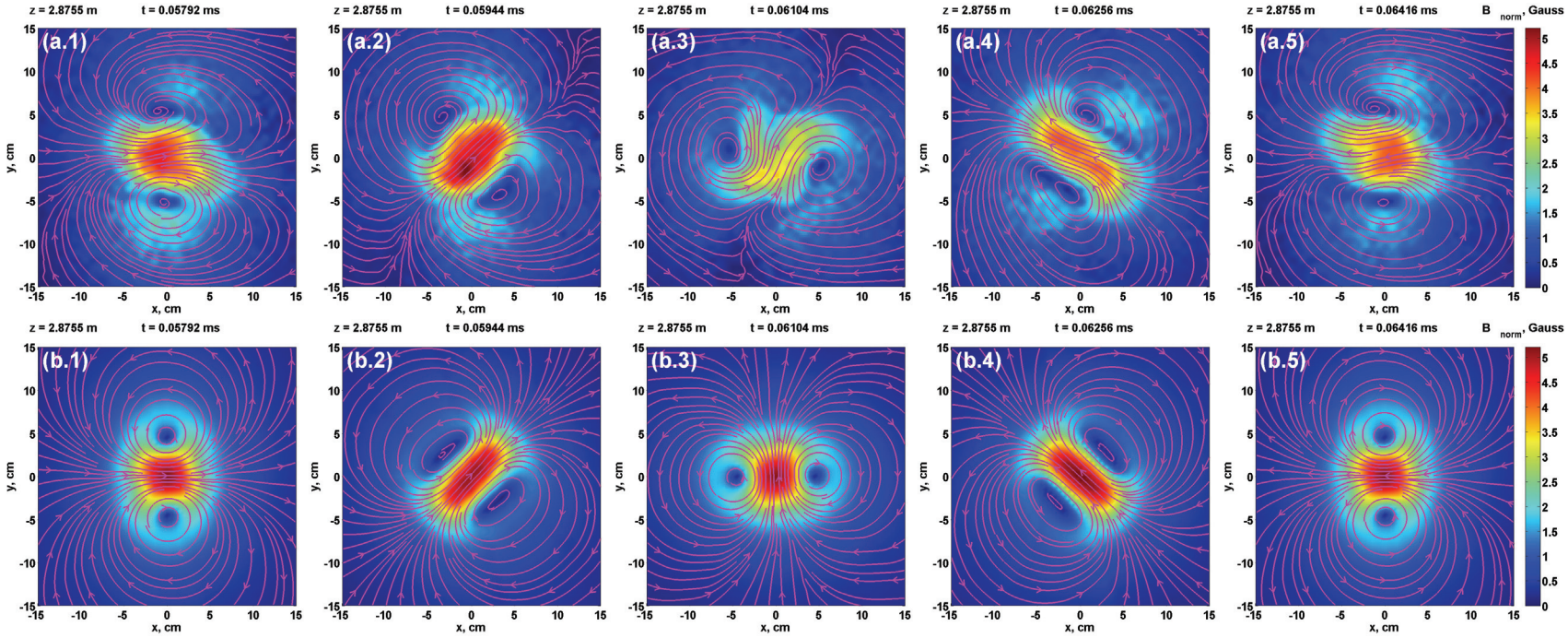

Figure 3.8: Comparison of the magnetic field structure in the plane $z = 2.88\ m$ away from the radiating antenna for five instants of time ($t_1 = 0.05792\ ms$, $t_2 = 0.05944\ ms$, $t_3 = 0.06104\ ms$, $t_4 = 0.06256\ ms$, and $t_5 = 0.06416\ ms$) separated by 1/8 of the wave period (driving frequency $f_d = 80\ kHz$) measured in the experiment (Experiment set 2) ((a.1) - (a.5)) and calculated using 3D model ((b.1) - (b.5)) for the right-handed polarization case. The ambient magnetic field $B_0 = 1000\ Gauss$ points outwards from the plane of the picture.

The amplitude of the induced magnetic field has its maximum on the center of the plane, that is on the symmetry axis of the machine, for all cases. The maximum amplitude is found to be independent of the polarization of the RMF source and on whether one or two loops are used. The characteristic transverse size of the wave propagating along the ambient magnetic field is about 20 cm in extent, which is approximately twice the diameter of the antenna loops, does not depend on the frequency or distance from the antenna along the z-axis. One more feature of the magnetic field structure is the two vortex structure with nearly constant distance between the centers of these vortices ~ 9 cm, determined by the antenna size. Using $\boldsymbol{\nabla} \times \mathbf{B} = 4\pi/c\mathbf{J}$, the centers of the vortices are found to correspond to the maxima of field aligned currents. This is similar to a pattern of Alfvén waves produced by two oscillating current channels and with a helical antenna [30, 34].

Figure 3.9 shows the dependence of the wave magnetic field amplitude along the ambient magnetic field measured in the experiment (Experiment set 1) by diamonds with uncertainty margins for the left-handed polarization of the RMF and driving frequency $f_d = 206\ kHz \sim 0.54 f_{ci}$. Approximate of the experimental data matched to an exponentially decaying function $A \exp(-k_i z)$ (A is the amplitude at $z = 0$, and k_i is imaginary part of the longitudinal wave number $k_{||}$) is shown by dashed line. The dependence calculated in the 3D simulations is shown by solid line, and calculated using analytical dispersion relation Eq. (3.1) by dash-dotted line. All of the curves shown have exponential decay with the rates $k_i = 0.101\ m^{-1}$ for the experiment, $k_i = 0.106\ m^{-1}$ for the model and $k_i = 0.083\ m^{-1}$ for the analytical dispersion relation, respectively, which are very close.

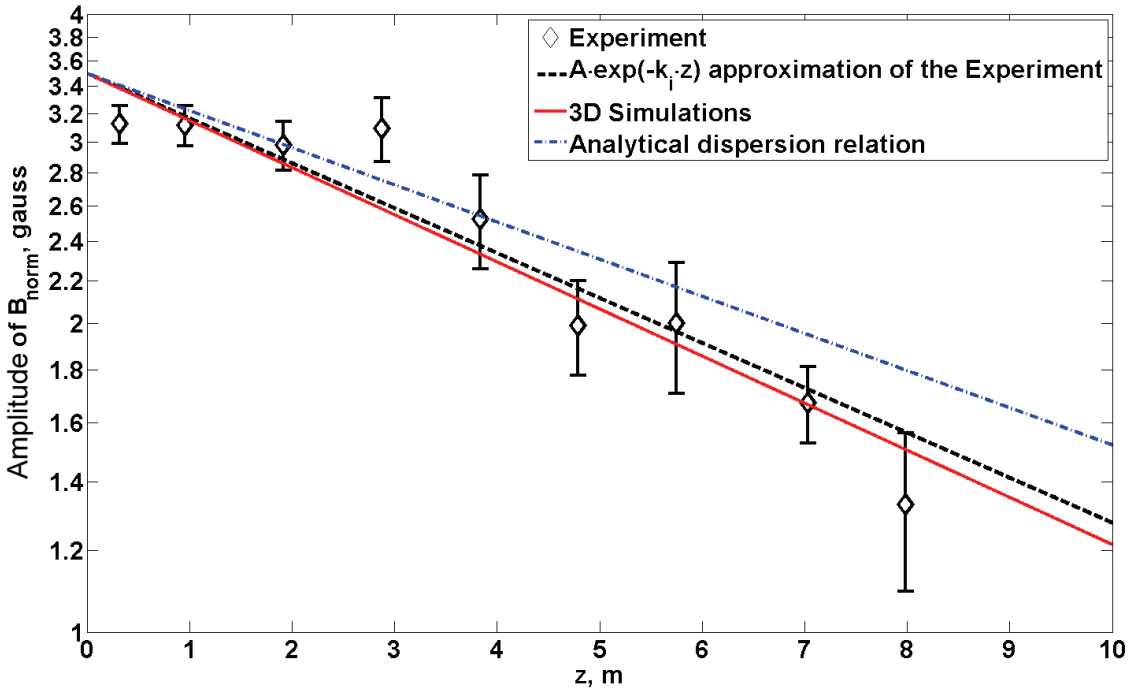

Figure 3.9: Dependence of the amplitude of induce magnetic field on distance z from the radiating antenna along the ambient magnetic field measured in the experiment (Experiment set 1) and calculated using 3D model. The amplitude dependence predicted by analytical dispersion relation Eq. (3.1) is plotted as well. Driving frequency $\omega = 0.54\Omega_{ci}$, left-handed polarization of the RMF.

Figure 3.10 shows the dependence of the wave magnetic field amplitude as a function of the transverse coordinate x for four different locations along z-axis calculated using the 3D model and measured in the experiment (Experiment set 1). One can see good quantitative agreement of the 3D model results with the experimental measurements.

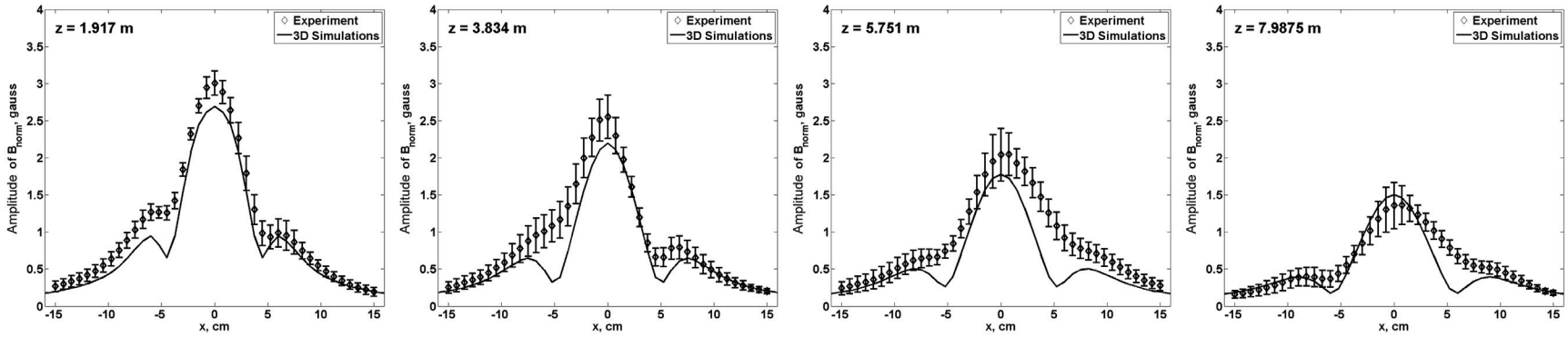

Figure 3.10: Dependence of the amplitude of induced magnetic field on x-coordinate perpendicular to the ambient magnetic field for different cross sections ($z = 1.917\ m$, $z = 3.834\ m$, $z = 5.751\ m$, and $z = 7.9875\ m$) measured in the experiment (Experiment set 1) and calculated using 3D model. Driving frequency $\omega = 0.54\Omega_{ci}$, left-handed polarization of the RMF.

3.3.2 Shear Alfvén wave dispersion relation

The SAW is an electromagnetic mode of magnetized plasmas and propagates nearly parallel to the background magnetic field in the frequency range below the ion cyclotron frequency $\omega < \Omega_{ci}$. For the parameters of the experiment the dispersion relation for the kinetic SAW including the effects of finite frequency and collisions can be written as [86]

$$\omega^2 - k_{||}^2 V_A^2 \left(1 - \frac{\omega^2}{\Omega_{ci}^2} + (\rho_s k_\perp)^2\right) + i\omega\nu_e k_\perp^2 \lambda_e^2 = 0, \tag{3.1}$$

where $\lambda_e = c/\omega_{pe}$ is the electron skin-depth, $\rho_s = c_s/\Omega_{ci}$ is the ion sound gyroradius, $c_s = (T_e/m_i)^{1/2}$ is the sound speed, T_e is the electron temperature, $k_\perp$ and $k_{||}$ are wave vector components perpendicular and parallel to the ambient magnetic field, $V_A = B_0/\left(4\pi n_i m_i\right)^{1/2}$ is the Alfvén speed, and ν_e is the effective electron collision frequency. In general, the propagation of the SAW across the ambient magnetic field is much slower than along the ambient field ($v_{ph\perp} = \omega/k_\perp \ll v_{ph||} = \omega/k_{||}$) [32,60,61] especially for the case when the wave is generated by a source with small transverse size. As a result, the SAW is well confined by the ambient magnetic field to a fixed flux tube.

Introducing the angle θ between the direction of the wave vector $\mathbf{k}$ and ambient magnetic field we can write $k_\perp = k\sin\theta$ and $k_{||} = k\cos\theta$, where k is the magnitude of the wave vector. Substituting $k_\perp$ and $k_{||}$ into Eq. (3.1) we can solve it for k as a function of ω and θ as

$$k_{1,2}^2 = \frac{i\frac{\omega\nu_e\lambda_e^2}{V_A^2}\tan^2\theta - \left(1 - \frac{\omega^2}{\Omega_{ci}^2}\right) \pm \sqrt{\left(i\frac{\omega\nu_e\lambda_e^2}{V_A^2}\tan^2\theta - \left(1 - \frac{\omega^2}{\Omega_{ci}^2}\right)\right)^2 + 4\frac{\omega^2\rho_s^2}{V_A^2}\tan^2\theta}}{2\rho_s^2\sin^2\theta} \tag{3.2}$$

In Fig. 3.11 the dependences between the perpendicular $k_\perp$ and parallel $k_{||}$ wave numbers calculated using Eq. (3.2) for collisional and collisionless cases, and those obtained from the numerical solution of the 3D model are presented for the driving frequency $\omega = 0.54\Omega_{ci}$. The parallel wave numbers corresponding to the parallel phase velocity measured in the experiment are represented by two vertical dashed lines. The general features of the curves calculated from Eq. (3.2) and obtained numerically using the 3D model are very similar, and they are particulary close to each other in the region of interest.

In Fig. 3.12 the dispersion relation ($k_{||}$ as a function of ω) is presented. Solid curves represent the dispersion relation found using the 3D model for collisionless ($\square$) and finite collision ($\circ$) cases. The dashed line represents the $k_{||}$ on ω dependence found using Eq. (3.1) assuming $Re\,(\lambda_\perp) = 18\ cm$. The symbols with uncertainty margins represent experimental measurements. One can see good qualitative agreement of the theory, simulations and the experiment, although the difference between the experiment and the 3D model predictions becomes significant for the higher frequencies approaching the ion cyclotron frequency.

In Fig. 3.13 the dependence of parallel phase velocity on frequency found using 3D model, calculated from Eq. (3.1) and measured in the experiment is presented. There is good agreement between them.

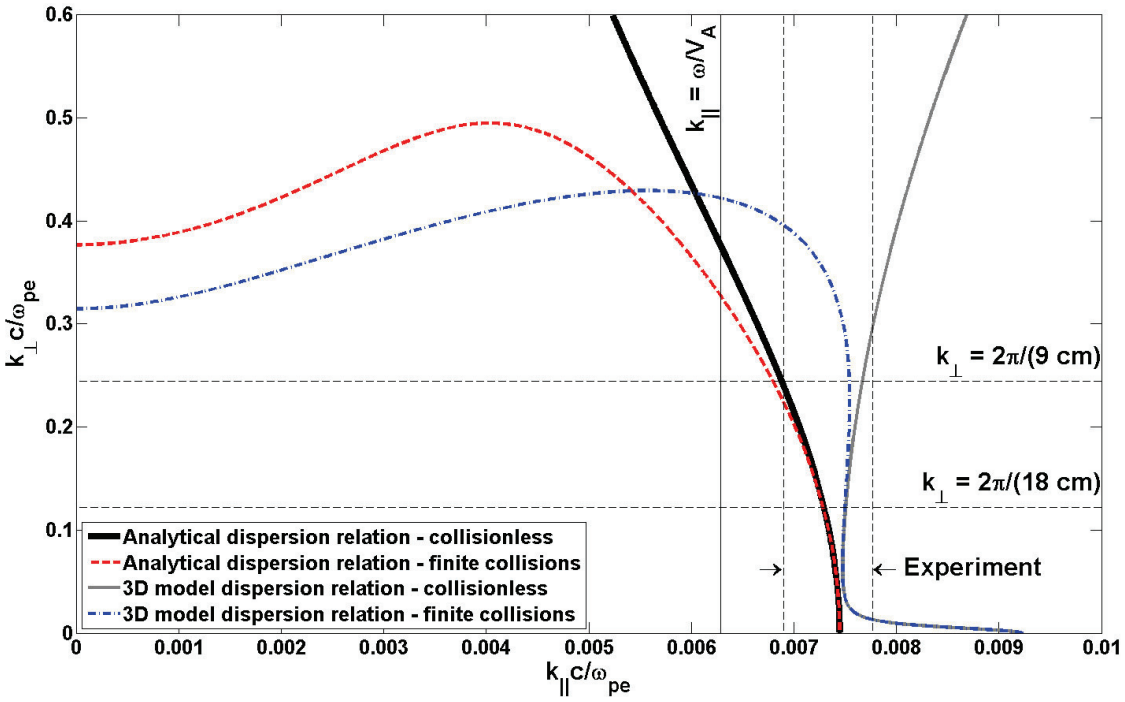

Figure 3.11: Dependence of transverse wave number $k_\perp$ on the longitudinal wave number $k_{||}$ for frequency $\omega = 0.54\Omega_{ci}$ given by analytical dispersion relation (Eq. (3.1)) and embedded in the 3D model for collisionless and collisional cases. The longitudinal wave number $k_{||}$ in the experiment are presented by two vertical dashed lines. Solid vertical line represents wave number corresponding to Alfvén speed. Two horizontal dashed lines represent transverse wave numbers corresponding to $\lambda_\perp = 9\ cm$ and $\lambda_\perp = 18\ cm$.

3.3.3 3D plasma current structure

Using the 3D two fluid model we found the plasma current structure for the parameters of the experiment (See Table 3.1) for driving frequency $f_d = 0.54\Omega_{ci}$. In Fig. 3.14 the 3D current structures for left-handed polarization (Fig. 3.14(a)), single loop antenna (Fig. 3.14(b)), and right-handed polarization of the RMF source (Fig. 3.14(c)) are presented.

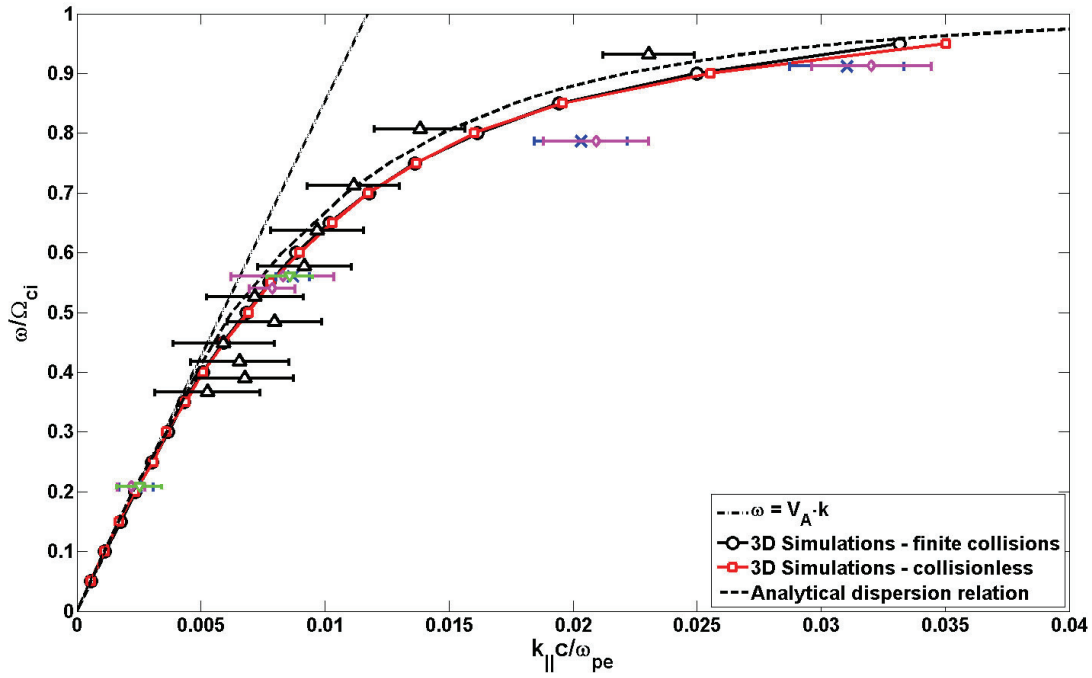

Figure 3.12: The RMF SAW dispersion relation obtained using 3D model for collisionless case (□) and the case with finite collisions given in the Table 3.1 (○). The analytical dispersion relation Eq. (3.1) is shown by dashed line. Experimental data: ▽ - one-loop antenna, × - right-hand polarization, ◇ - left-hand polarization, △ - reference [35].

The picture features isosurfaces of the total current. The color indicates the direction of the J_z component (red - J_z is positive, blue - J_z is negative). The black streamlines show the induced magnetic field in the planes perpendicular to the z-axis, which has a two vortex structure. The centers of the vortices correspond to the maxima of the current crossing the plane. For all the cases the current is very well confined by the ambient magnetic field. The current structure found in the 3D simulations is very similar to one found from the experimental measurements using $\mathbf{J} = c/(4\pi)\,\boldsymbol{\nabla} \times \mathbf{B}$ (See Fig. 3.15).

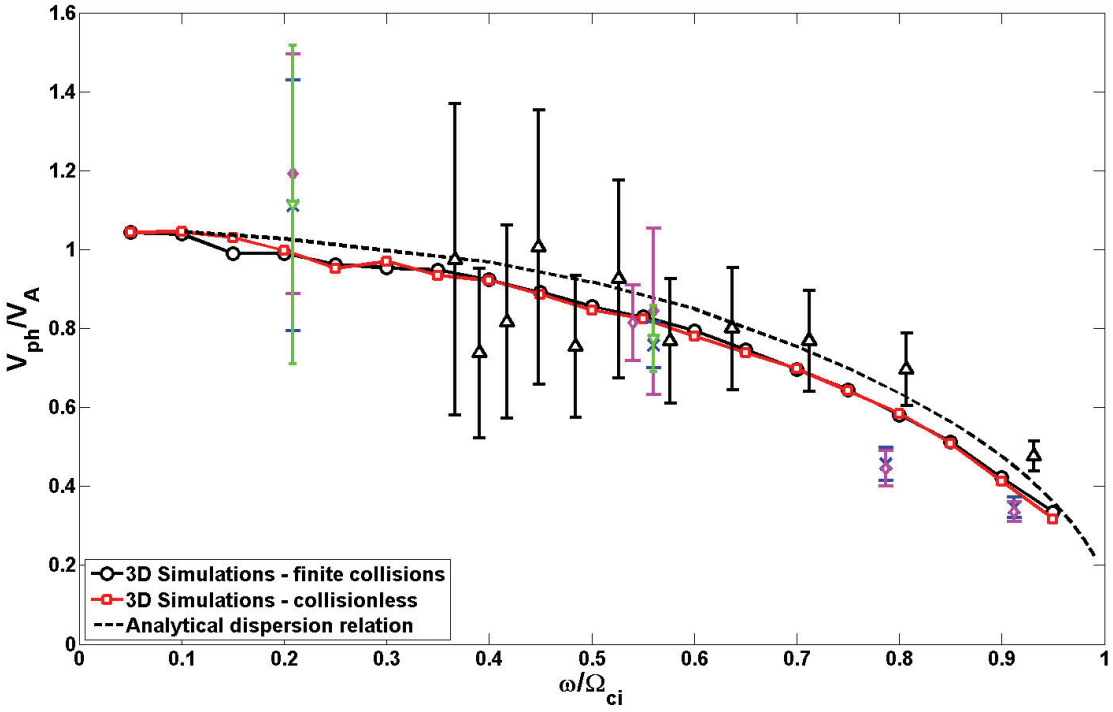

Figure 3.13: The RMF SAW phase velocity dependence on driving frequency obtained using 3D model for collisionless case (□) and the case with finite collisions given in the Table 3.1 (○). The analytical dispersion relation Eq. (3.1) is shown by dashed line. Experimental data: ▽ - one-loop antenna, × - right-hand polarization, ◇ - left-hand polarization, △ - reference [35].

3.3.4 Amplitude of perturbation as a function of frequency

In this subsection the dependence of the amplitude of the induced magnetic field on the driving frequency ω is discussed. In Fig. 3.16 the dependence measured in the experiment (◇) and calculated using the 3D model in collisionless and collisional cases for the plasma parameters of experiment set 2 (See Table 3.1) are presented. The currents in the loops were $I_1 = I_2 = 500$ *Amps*. One can see a very good agreement between the first four experimental points and the 3D model

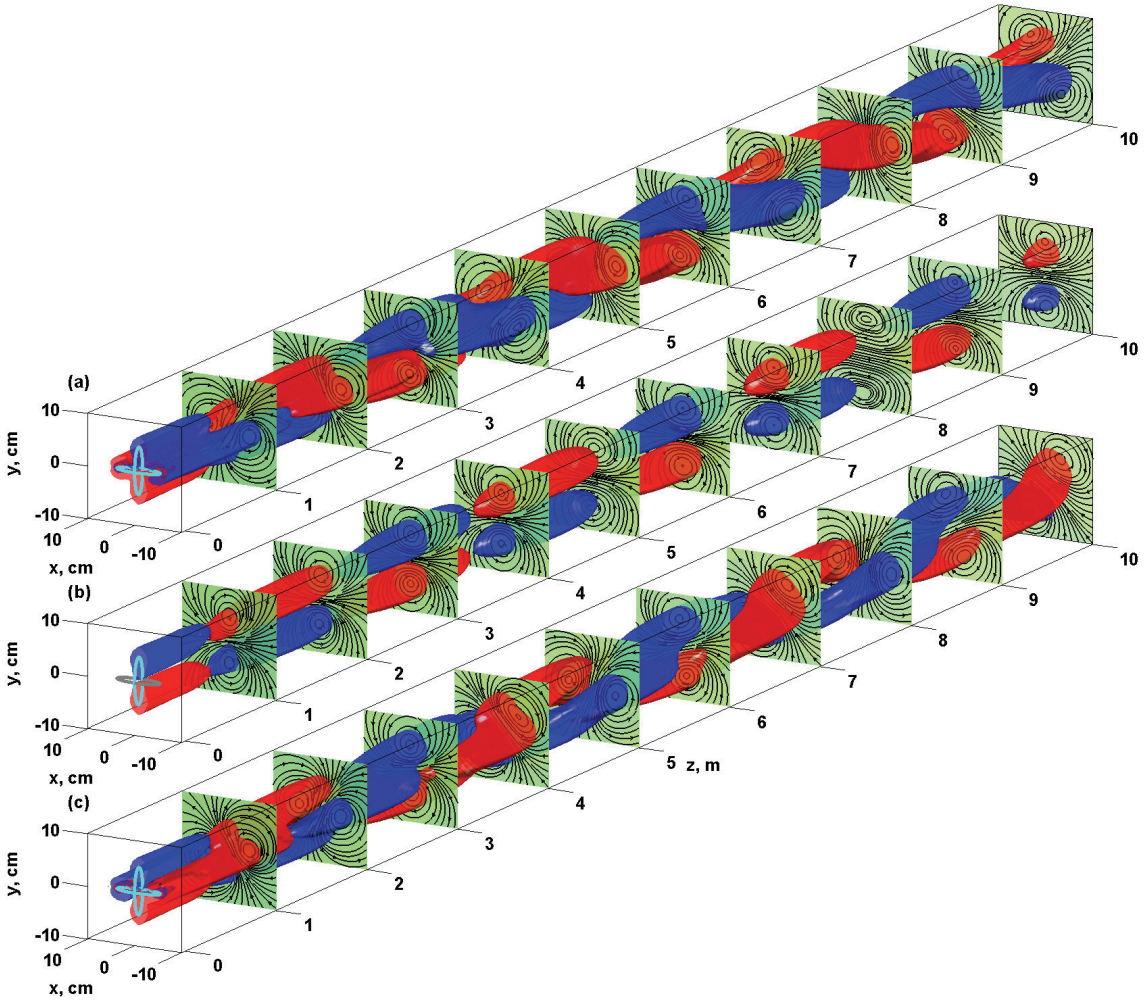

Figure 3.14: Isosurfaces of total plasma current ($J = \sqrt{J_x^2 + J_y^2 + J_z^2}$) the same time instant calculated using 3D model for left-hand polarization (a), one-loop antenna (b) (the current laying in xz-plane is turned off), and right-hand polarization cases (c). Red color corresponds to the isosurface with positive J_z-component of the plasma current, and blue - with negative J_z-component. The structures of the perturbed magnetic field in the planes perpendicular to z-axis are shown by black stream lines. The ambient magnetic field $B_0 = 1000$ *Gauss* is directed along z-axis. The radiating antenna is shown at the origin. Driving frequency $\omega = 0.54\Omega_{ci}$. Note that the length of the box shown is 10 m, and the size across z-axis is only 20 cm.

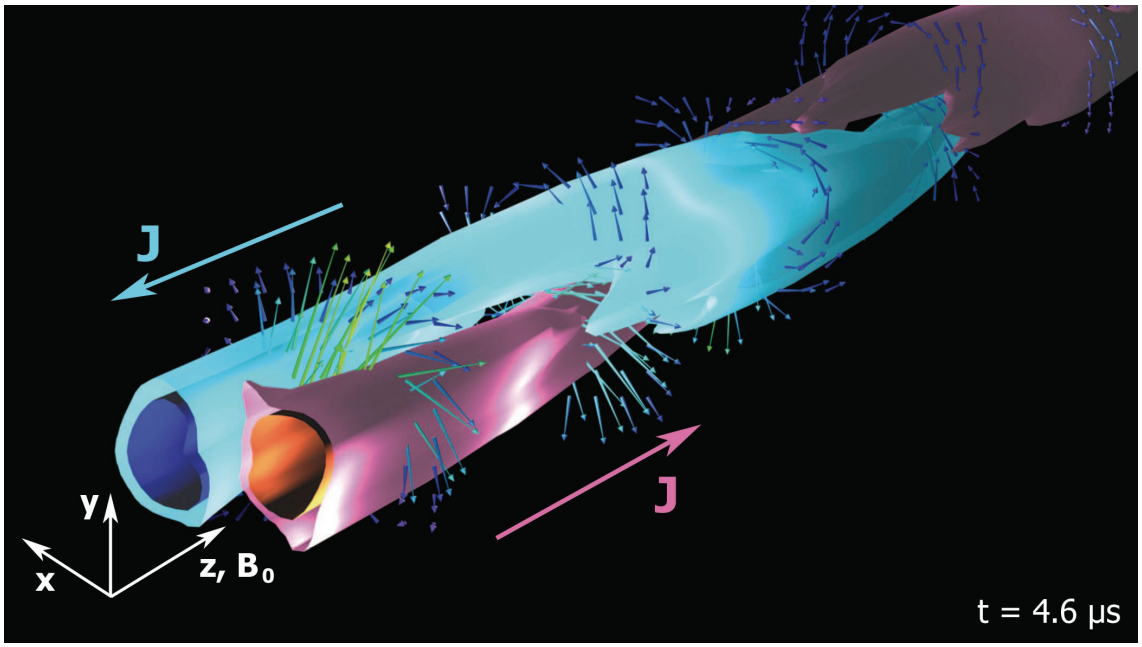

Figure 3.15: Isosurfaces of total plasma current density ($J = \sqrt{J_x^2 + J_y^2 + J_z^2}$) at $t = 4.6\mu s$. The surfaces begin 33 cm to the right of the antenna and end approximately 8 m away. Two rotating, counterpropagating helical current channels can be seen flowing in z-direction along $\mathbf{B}_0$. As time advances the currents rotate in a left-handed sense. The outer isosurface represents a current density 0.25 A/cm^2 and the inner surface - a current density of 0.5 A/cm^2, where red color denotes current flow in the positive z-direction and blue - in the negative z-direction. Magnetic field vectors are also shown. (Credit: A. Gigliotti, W. Gekelman, S. Vincena, UCLA).

results. The dependence of the amplitude of the wave magnetic field measured in the the experiment and calculated using the 3D model is in a good agreement with another experiment performed in the LAPD [85]. In that experiment the SAWs were launched by a small (1 cm in diameter) circular copper mesh antenna and propagated in the varying along the axis of the machine background magnetic field $B_z(z)$, which is equivalent to varying ω/Ω_{ci} ratio.

The difference between the model and the experiment for the frequency $\omega = 0.93\Omega_{ci}$ can be explained by the following argument. As the driving frequency approaches the ion cyclotron frequency the ion resonant heating by the wave starts to play an important role and the wave transfers its energy to the ions. Besides that, because of the ion heating the SAW energy can be transferred also to another wave mode, namely, magnetosonic wave, which propagates omnidirectionally unlike SAWs. This processes can lead to a dramatic decay of the wave amplitude and are not included in the 3D model. The last one can be included in the model by adding to the equation of motion of electrons (Eq. (B.1c)) and ions (Eq. (B.1d)) of $-\nabla p_e$ and $-\nabla p_i$ terms, respectively, where p_e and p_i are electron and ion pressures. The p_e and p_i are determined by the densities n_e and n_i through equations of states. Then the system of equations (B.1) can be closed by including the continuity equations for electron and ion fluids.

For both the collisional and collisionless cases the SAW mode does not propagate above the ion cyclotron frequency, which explains the drop to zero of the 3D model curves for the frequencies higher than ion cyclotron frequency. The increase of the wave magnitude with the driving frequency can be explained by the fact that

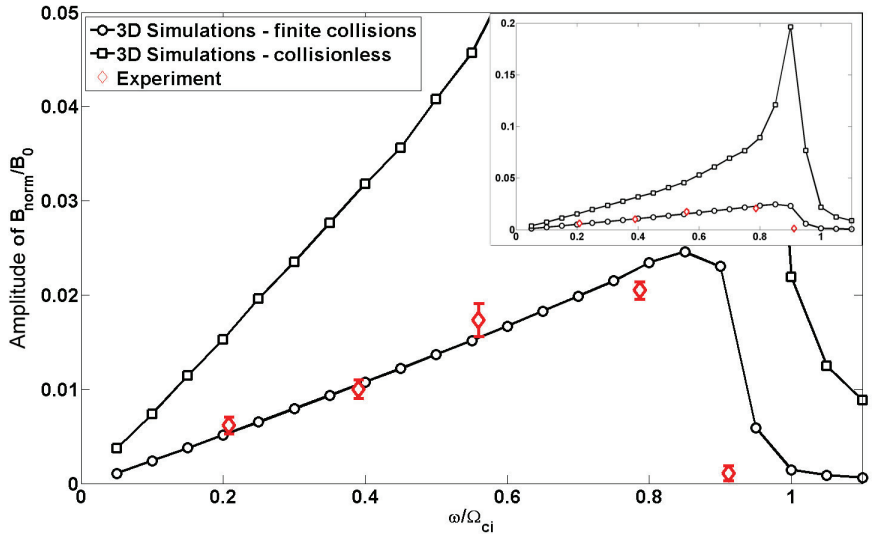

Figure 3.16: Dependence of the amplitude of induced magnetic field at $z = 2.88\ m$ away from the antenna obtained using 3D model for collisionless case ($\square$) and the case with finite collisions ($\circ$) and measured in the experiment ($\diamond$) (Experiment set 2) for two-loop antenna case with left-hand polarization on the driving frequency. Magnitude of currents in the loops $I_1 = I_2 = 500\ Amps$. The large graph and the inset show the same dependencies but with different scale on amplitude of B_{norm} axis.

the parallel group velocity $v_g = \partial\omega/\partial k_{||}$ of the SAW, that is the wave energy propagation parallel to the ambient magnetic field, decays as the frequency increases (See Fig. 3.12). This means that the wave energy density and the wave magnitude increase. The maximum of the wave energy in the collisionless 3D model curve corresponds to the parallel wave length nearly matching the diameter of the antenna $D_a \approx \lambda_{||}/2$. The difference in the slopes of the collisional and collisionless 3D model curves is due to the dependences presented are for $z = 2.88\ m$ (Fig. 3.16), and the spatial decay rate along the ambient magnetic field due to collisions increase with frequency increasing.

3.3.5 Energy balance of the wave

The total energy generated by the RMF antenna which couples to the plasma wave is shared by four effects: the energy of the magnetic field $u_M = \frac{1}{2\mu_0} B_w^2$, energy of the electric field $u_E = \frac{1}{2}\varepsilon_0 \varepsilon_\perp E_w^2$, and the kinetic energy of electrons u_{Ke}, and ions u_{Ki}. Here $\varepsilon_\perp$ is the perpendicular component of the plasma dielectric permittivity tensor, which is in general a function of plasma parameters and the wave frequency. To first order the magnetic and electric field components of the electromagnetic mode wave energy in the absence of charge separation are approximately equal. From the experimental measurements we can quite accurately derive the value of u_M. In Ref. [35] the wave magnetic field power was estimated as

$$P = V_A \frac{\delta B_w^2}{\mu_0} A, \tag{3.3}$$

where V_A is Alfvén speed δB_w is the amplitude of the induced magnetic field, and A is the characteristic cross section of the wave. The wave power for the Experiment set 1 estimated using Eq. (3.3) was $\sim 200\ W$. The wave power can be obtained more accurately using the Poynting vector crossing the plane perpendicular to the ambient magnetic field, given by

$$S = \frac{1}{2}\left(\varepsilon_0 \varepsilon_\perp E_w^2 + \frac{1}{\mu_0} B_w^2\right) v_{g||} \approx \frac{1}{\mu_0} B_w^2 v_{g||}, \tag{3.4}$$

where $v_{g||} = \frac{\partial \omega}{\partial k_{||}}$ is the parallel component of the wave group velocity. From Fig. 3.12 one can see that for the frequency $\omega = 0.54\Omega_{ci}$ the group velocity $v_{g||} \lesssim v_{ph||}$. Thus, the total energy passing trough the plane perpendicular to the ambient magnetic

field per unit time is

$$P = \int \mathbf{S} d\mathbf{A} \approx \frac{v_{ph||}}{\mu_0} \int B_w^2 dA. \tag{3.5}$$

The power calculated from the experimental data using Eq. (3.5) as a function of the distance from the antenna is presented in Fig. 3.17 as diamonds. the Dashed line in Fig. 3.17 represents the $A \exp(-bz)$ approximation of the experimental points. The exponential decay rate is determined by the collisions and is consistent with the exponential decay of the magnetic field magnitude (See Fig. 3.9). The antenna power which couples to the wave magnetic field is $2P_M(z=0) \approx 250\,W$ (2 is for the propagation in two directions along positive and negative z-directions) and the total electromagnetic energy of the wave is $\sim 500\ W$. There are no experimental measurements of the kinetic energies of the electrons and ions, but we expect that will be of the same order as the magnetic field energy.

Using the 3D model we can calculate all components of the wave energy and the total power of the wave. The components of the wave energy as a function of time we calculate as

$$E_M(t) = \frac{1}{2\mu_0} \int_V |\mathbf{B}(t,x,y,z)|^2 dV, \tag{3.6a}$$

$$E_{Ke}(t) = \frac{nm_e}{2} \int_V |\mathbf{v}_e(t,x,y,z)|^2 dV \tag{3.6b}$$

$$E_{Ki}(t) = \frac{nm_i}{2} \int_V |\mathbf{v}_i(t,x,y,z)|^2 dV \tag{3.6c}$$

where V is the whole computational domain, n is the plasma density, m_e, m_i and $\mathbf{v}_e$ and $\mathbf{v}_i$ are electron and ion masses and velocities, respectively. Taking the time derivatives of Eqs. (3.6) we get the components of the power corresponding to the electric and magnetic fields and the electron and ion fluids. In the collisional case

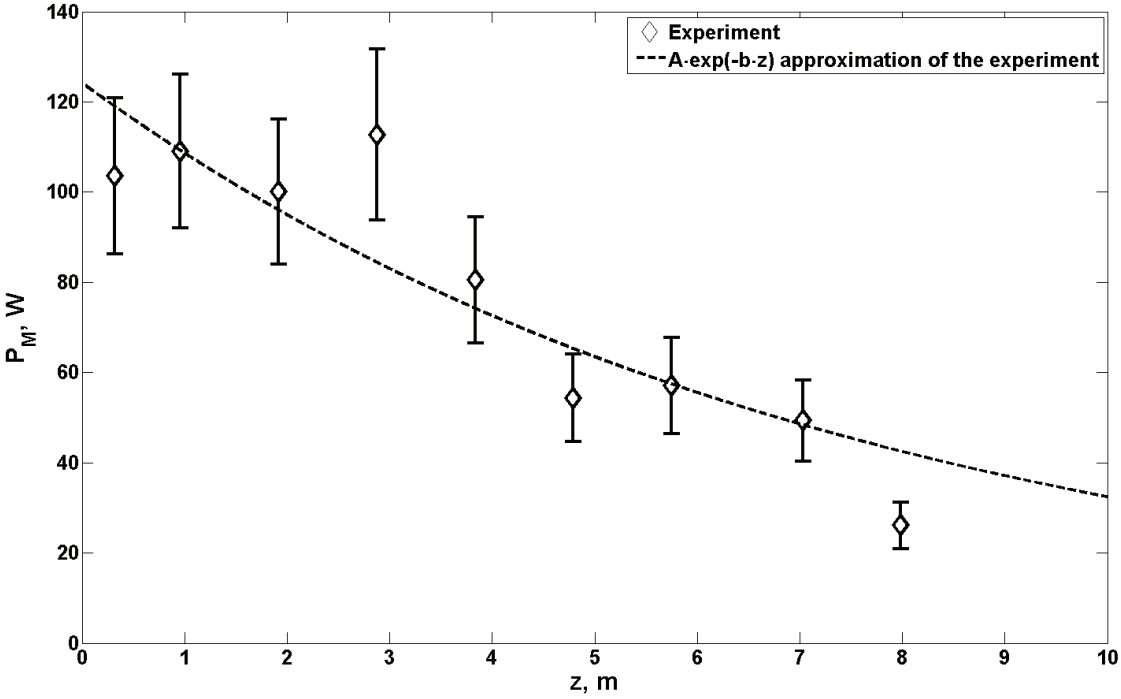

Figure 3.17: Dependence of the magnetic component of the wave power propagating along the ambient magnetic field as a function of the distance from the antenna calculated from the experimental data ($\diamond$). Dashed line represent $A\exp(-kz)$ of the experimental points. (Experiment set 1, driving frequency $\omega = 0.54\Omega_{ci}$, magnitude of the currents $I_1 = I_2 \approx 600\ A$).

for a propagating mode there are no sinks of the energy in the model and the power injected by the antenna is equal to the sum of the wave power components.

In Fig. 3.18 the components of the wave energy as a functions of time for collisionless (Fig. 3.18(a)) and collisional (Fig. 3.18(b)) cases with experimental parameters (Experiment set 1) are shown. The time derivatives of the dependences of the energy components give the corresponding powers. From the 3D simulation in the collisionless case we found that the magnetic field power is $P_M = 253.0\ W$ (compared to $250\ W$ - the magnetic power estimated from the experimental data). The power which couples to the motion of ions is $P_{Ki} = 500.3\ W$, which is $1.98 P_M$, and the power which couples to the motion of electrons is $P_{Ke} = 26.19\ W$. The total power radiated by the antenna in this case was found to be $\sim 1030\ W$ and during the $100\ \mu s$ pulse $103\ mJ$ was injected by the antenna. Thus, for the driving frequency $\omega = 0.54\Omega_{ci}$ the antenna power which couples to the wave is nearly equally distributed between the electromagnetic component and kinetic energy of ions, and the kinetic energy of electrons is of order $\sim 2.5\%$ of total wave energy.

In the collisionless case the wave energy grows linearly with time, as all energy injected by the antenna is conserved, while in the presence of the collisions the energy has a sink. This results in the decay of the time derivatives of the component energy dependencies with time. As the time progresses the propagating wave occupies larger volume, and larger parts of the ion and electron fluids are involved in motion. As a result the amount of energy lost due to the collisions increases. Asymptotically the wave comes to an energetic equilibrium with the media, when the power injected by the antenna is equal to the energy lost due to collisions per unit time.

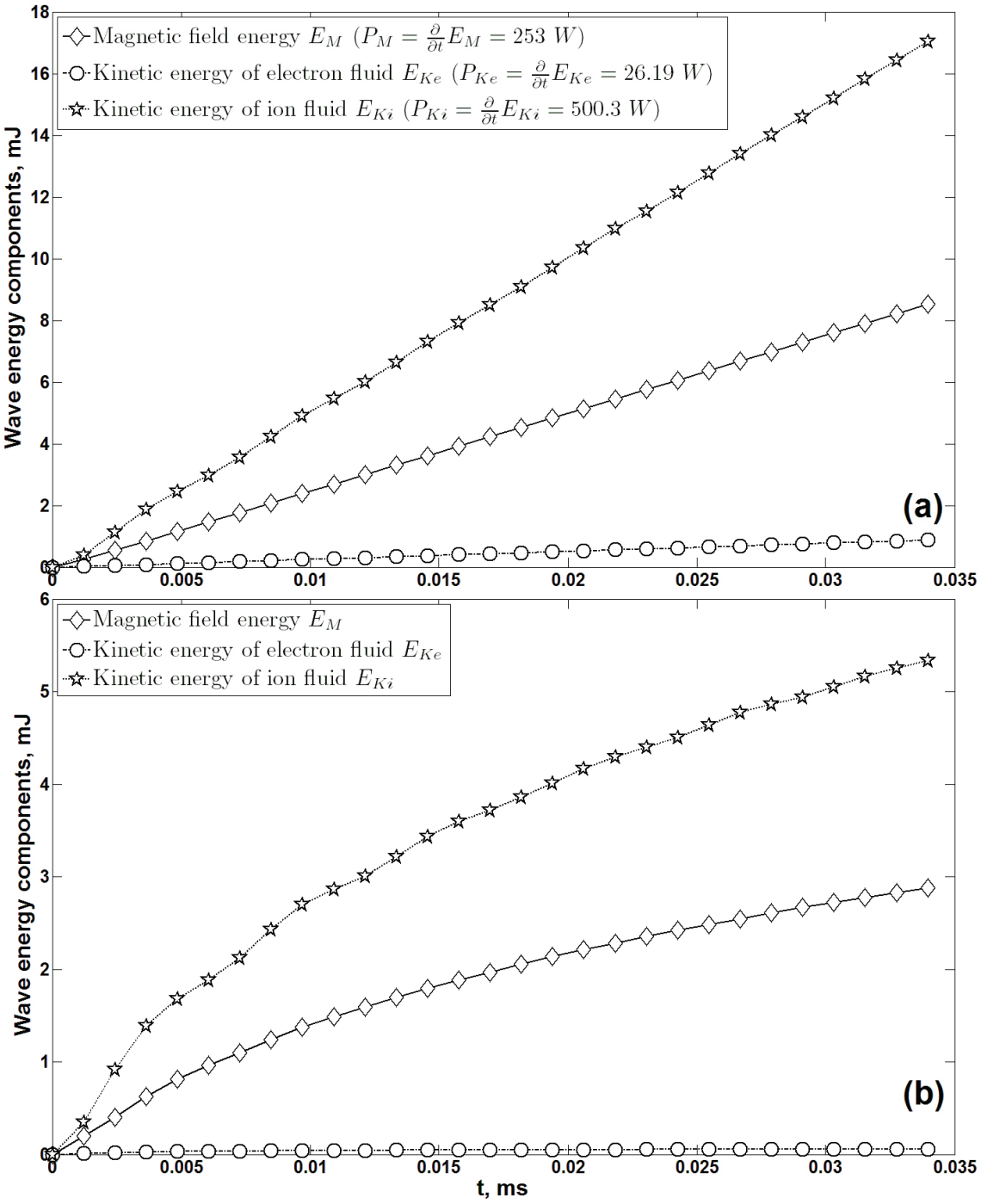

Figure 3.18: Dependences of the components of the wave energy on time calculated using 3D model for collisionless (a) and collisional (b) cases. The time derivatives give the power corresponding to each component (Experiment set 1, driving frequency $\omega = 0.54\Omega_{ci}$, magnitude of the currents $I_1 = I_2 \approx 600\ A$).

In Fig. 3.19 dependencies of the power corresponding to the wave components on the driving frequency calculated using the 3D model for the Experiment set 1 parameters and magnitudes of driving currents $I_1 = I_2 = 600\ A$ for all frequencies are presented. For the entire frequency range the electric field power is negligible to the others, and electron fluid carries only small (order of %) portion of the wave energy. For low frequencies ($\omega \lesssim 0.3\Omega_{ci}$) the magnetic field power and the power of the ion fluid are essentially equal. When the driving frequency goes up the energy which couples to the ion fluid motion grows up fast. The magnetic field power grows much slower than the power of ion fluid, reaches its maximum at about $0.8\Omega_{ci}$ and than start to decrease. For high frequencies almost all the power radiated by the RMF antenna couples to the kinetic energy of the ions. The dashed line shows the approximation of the calculated using the 3D model values of the total power by a function $P \sim \omega^2$. One can see that for the frequencies below the half of the ion cyclotron frequency the points lie on top of the $P \sim \omega^2$ curve. As the frequency approaches the ion cyclotron resonance the energy starts to couple to the ion fluid motion more efficiently.

3.4 Conclusion

It is demonstrated in the experiments and three-dimensional cold two-fluid magnetohydrodynamics simulations that the rotating magnetic field antenna composed of two independent coils with alternating currents set $\pm 90^o$ out of phase can efficiently generate shear Alfvén waves with high transverse wave number with arbi-

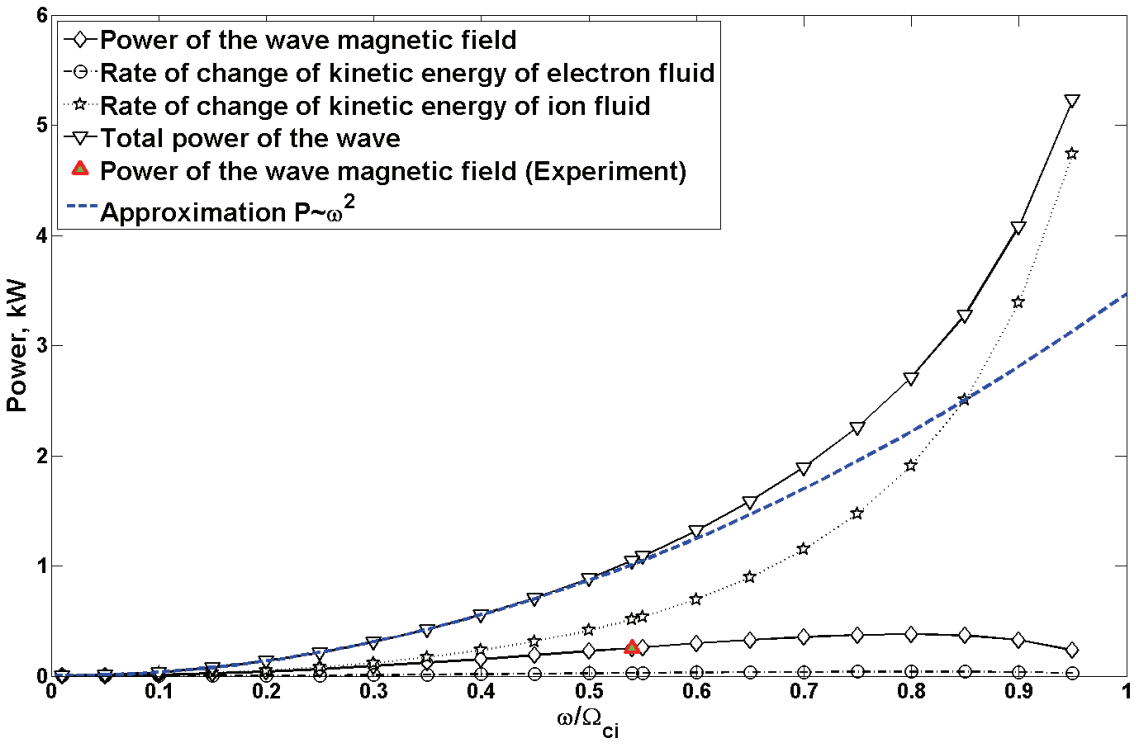

Figure 3.19: Dependence of the wave power on the driving frequency calculated using 3D model for the Experiment set 1 parameters and magnitudes of driving currents $I_1 = I_2 = 600\ A$ for all frequencies.

trary polarization depending on the polarization of the RMF antenna. The results of semi-analytical 3D model simulations were compared with the measurements in the LAPD experiments and found to be in a good agreement for wide rage of the parameters.

The spatio-temporal wave structures calculated from the simulations are very close to those measured in the experiments. It is shown in the experiment [35] and calculated using the 3D model that the SAWs generated by the RMF carry significant field aligned currents which propagate parallel to the ambient magnetic field lines without noticeable spreading in the transverse direction.

The theoretical dispersion relation of the SAW, the dispersion relations calculated using 3D model and measured in the experiment are very close for a broad frequency range. The exponential decay rate of the wave along the ambient magnetic field is determined by the collisions.

The dependence of the amplitude of the wave magnetic field on the driving frequency measured in the experiment and calculated from 3D model are very close to each other except for the frequencies very close to the ion cyclotron frequency. This can be explained by the fact that the resonant wave-particle interaction and magnetosonic wave mode are not included in the model.

The power of the magnetic filed of the generated wave is calculated from the experimental data (Experiment set 1) and found to be $\sim 250\ W$ for the driving frequency $\omega = 0.54\Omega_{ci}$, and the current magnitudes $I_1 = I_2 = 600\ A$. The power found in 3D simulations for the magnetic field for the experimental parameters is 253 W, which differs from the experimental value only by $\sim 1\%$. The wave power

corresponding to the other components of the wave, namely, the kinetic energy of electron and ion fluid calculated from 3D simulations are $P_{Ke} = 26.19\ W$, and $P_{Ki} = 500.3\ W$, respectively. Thus, the energy of the wave is distributed as: $\sim 1/2$ - electromagnetic field energy, $\sim 1/2$ - the kinetic energy of ions, and $\sim 2.5\%$ - the kinetic energy of electrons. The fraction of the wave energy carried by the electrons gives an estimate of the error we would make for the experimental parameters if we considered the electrons as massless and modeled the plasma by single-fluid MHD.

Thus, the 3D two-fluid model was verified using the experimental results. Good overall agreement of the 3D model results with the experimental measurements for wide ranges of the experimental parameters shows good predictive capability of the 3D model, and it can be used for the parameters that hard to achieve in laboratory plasmas or space plasma configurations.

Chapter 4

Pitch angle scattering of electrons by the waves generated by RMF source

4.1 Experiments on pitch angle scattering of energetic electrons by waves generated by RMF source

The sharp transverse magnetic field gradients of the RMF generated whistler and shear Alfvén waves indicate the potential for breaking of the first adiabatic invariant and pitch angle scattering of charged particles into the loss cone. This could be an important process for RMF wave injection in the magnetosphere given the fact that the highly energetic trapped electron gyroradii in the radiation belts are of the order hundreds of meters and can be comparable or even exceed the characteristic scale of the wave magnetic field in the transverse direction. An experiment on the scattering of hot electrons by RMF generated shear Alfvén wave conducted in LAPD machine [33,36] showed a strong effect of the latter. I present here summary of the experiment and the major findings.

The LAPD-machine is a vacuum chamber surrounded by 56 DC magnets (Fig. 2.1) in which currents can be adjusted independently, providing the device with the capability of generation ambient stationary magnetic fields with arbitrary profiles along the machine. In this experiment the DC currents in the magnets were

set to provide a magnetic trap configuration (See Fig. 4.1). The loss cone angle for a magnetic mirror can be estimated as

$$\theta_{LC} = \pi - \arctan\left(\sqrt{\frac{B_{max}}{B_{min}} - 1}\right), \tag{4.1}$$

which in the experiment configuration gives $\theta_{LC} \approx 55^o$.

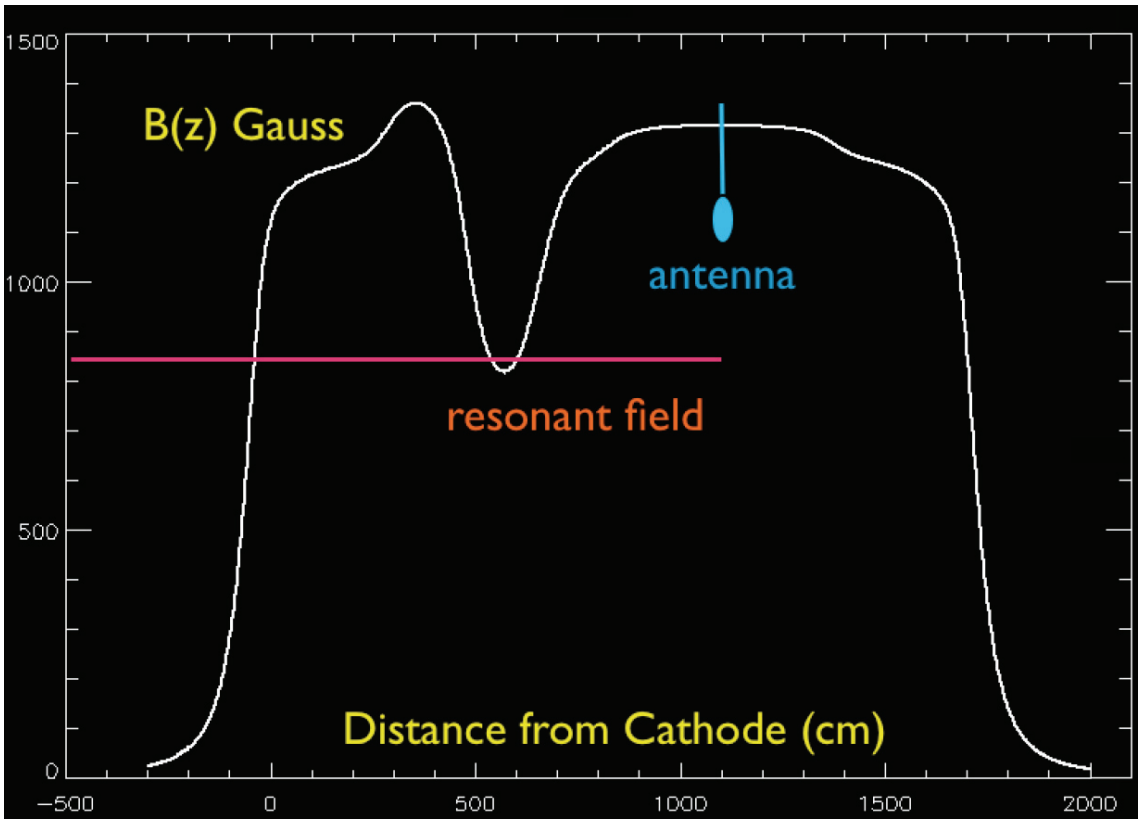

Figure 4.1: Ambient magnetic field profile in the experiments on pitch angle scattering of hot electrons by waves generated by RMF source. A magnetic field trap was created by adjusting the currents in the solenoidal DC magnets. The resonant location for ECRH is narrow, $dz \sim 2\ cm$. The RMF antenna used in the shear Alfvén experiments (See Chapter 3) was placed Approximately 5 m away from the magnetic trap (Adopted from [33, 36]. Credit: Walter Gekelman, Steve Vincena, UCLA).

An electron population with high perpendicular component of the velocities $v_\perp$

was introduced in the afterglow of the background LAPD plasma ($n \approx 2\times10^{11}\ cm^{-3}$, $T_e \approx 0.25\ eV$) by Electron Cyclotron Resonant Heating (ECRH). The heating source was 2.45 GHz microwaves generated by a pulsed magnetron and delivered to the resonant interaction region by a copper waveguide fed through a vacuum interlock on the side of the machine at the z-location corresponding to the minimum of the ambient magnetic field (See Fig. 4.2). A small ($\sim 2\ cm$ dia) electron hot spot was generated with the electron temperatures estimated at $\sim 1\ keV$.

Figure 4.3 shows hot electron currents in the magnetic trap generated by the microwave heating when no waves were launched (green curve in Fig. 4.3) compared to the case when the RMF generated shear Alfvén wave was launched (orange curve in Fig. 4.3). The microwave radiation was turned on at moment $t = 0$. One can see that the hot electron current builds up and reaches its maximum at $t \approx 0.8\ ms$. The energetic electron population with high transverse components of velocity is trapped by the magnetic mirror due to the conservation of the first adiabatic invariant and, in the absence of RFM injected waves, present in the system during the entire ECRH on period.

The shear Alfvén wave generated by RMF source with left-handed polarization and driving frequency $f_d = 192\ kHz$ was launched by the RMF two-loop antenna placed $\sim 5\ m$ away from the minimum of the ambient magnetic field. When this wave with amplitude of order $B_w \sim 2\ Gauss$ in the vicinity of the magnetic trap was launched the energetic electron population disappeared within 10 wave cycles. The RMF source was turned on at $t = 1.1\ ms$ launching shear Alfvén wave during $0.1\ ms$. During the period when the shear Alfvén wave source was turned on the

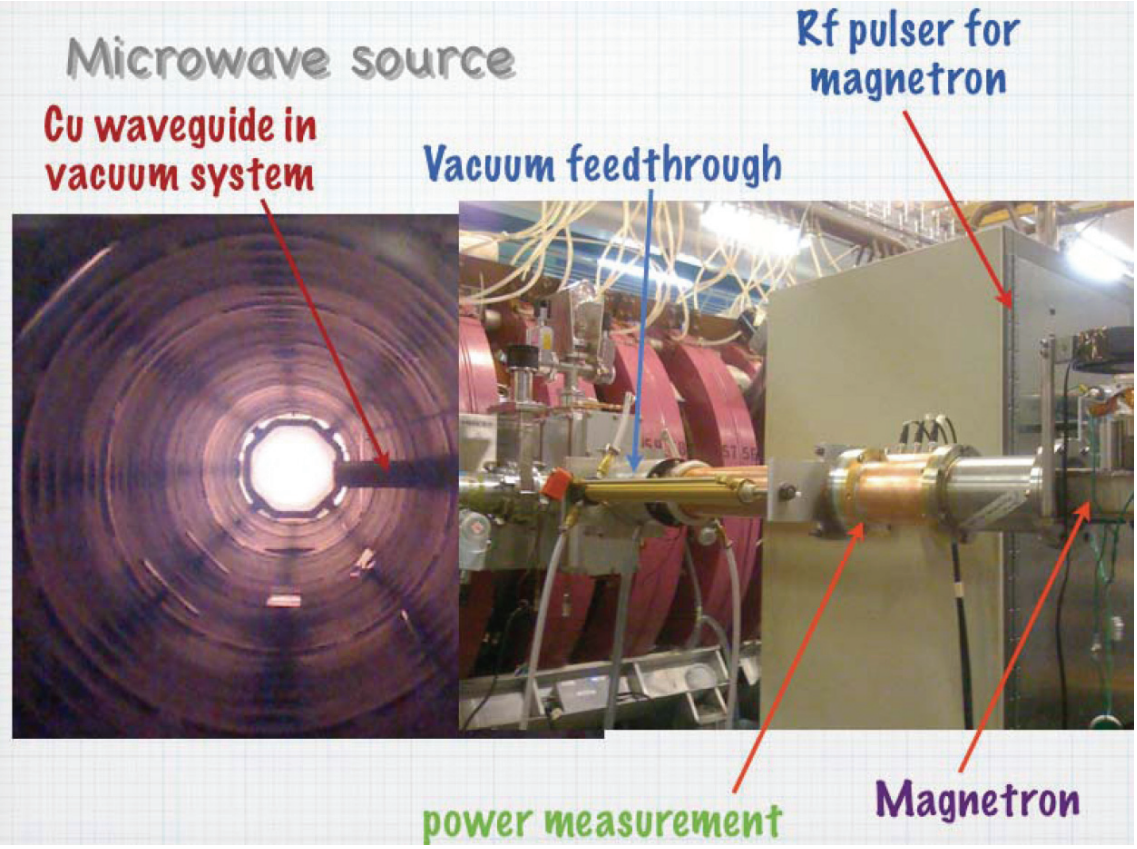

Figure 4.2: Microwave source used in the experiment for resonant electron heating. 2.45 GHz microwaves were generated by a pulsed magnetron. The microwave waveguide, a Cu pipe fed through a vacuum interlock on the side of the machine, delivered microwave radiation to the electron cyclotron resonant region, where $f_{\mu w} = f_{ce}$. The left hand photograph shows the waveguide at the edge of the plasma column. (Adopted from [33,36] Credit: Walter Gekelman, Steve Vincena, UCLA).

hot electron current decreased essentially to zero. When the RMF radiation source was turned off the hot electron current returned (orange curve in Fig. 4.3).

Detailed description of the diagnostics used in the experiment along with detailed measurements of space-time evolution of the plasma density in the magnetic trap will be published elsewhere. It is clear that the injection of the RMF generated

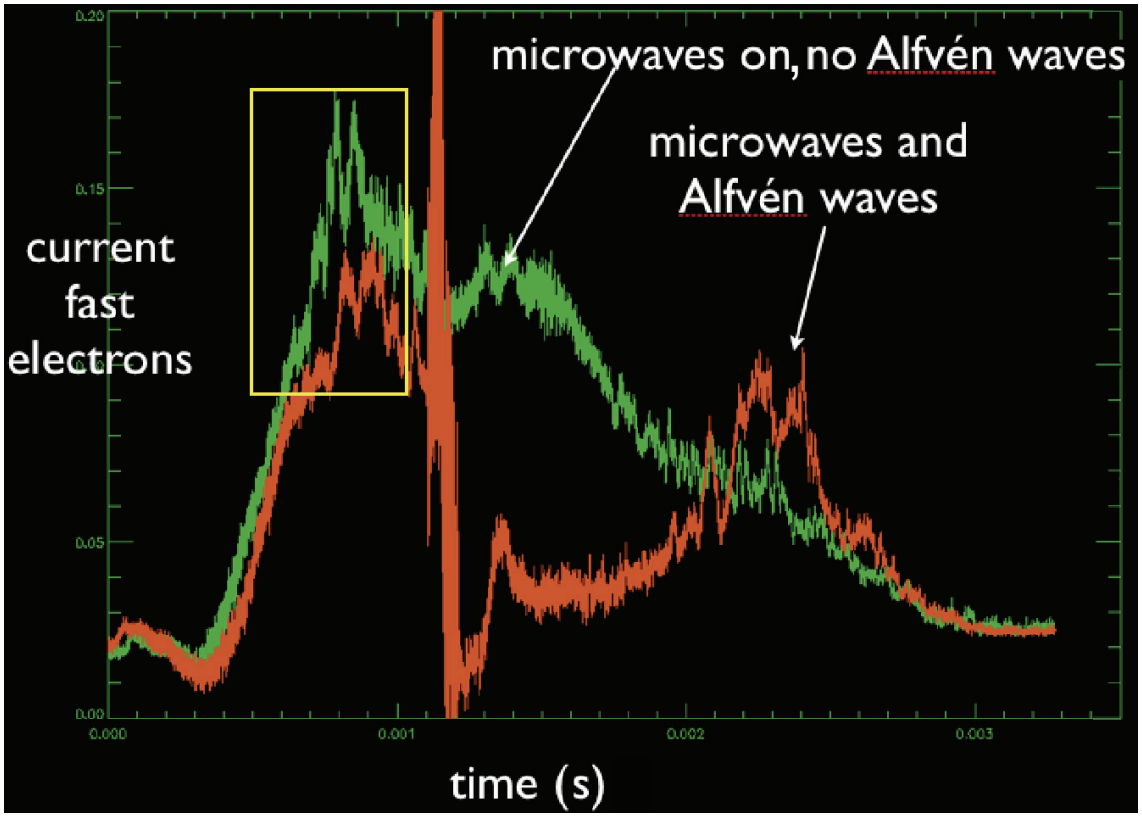

Figure 4.3: Hot electron current (arbitrary units) in the magnetic trap measured in the experiment when the RMF source was turned off (green curve) and when the shear Alfvén wave generated by the RMF source with left-handed polarization was launched at time $t = 1.1\ ms$ lasting $0.1\ ms$ (orange curve) (Credit: Walter Gekelman, Steve Vincena, UCLA).

waves had an important effect on the lifetime of the trapped energetic electrons. In order to understand the physical processes in the scattering of hot electrons from magnetic trap in the experiment performed in the LAPD we conducted a series of test-particle simulations with the parameters close to the experimental values.

4.2 Setup of test particle simulations

The three-dimensional cold two magnetized fluid code described in detail in the Appendix B and verified with the experimental results (See Chapter 3) was used to produce the wave electric and magnetic fields generated by RMF source for test particle simulations of the pitch angle scattering of trapped hot electrons by numerically solving their relativistic equations of motion. The computational domain has a size of $35\ cm \times 35\ cm \times 10\ m$ (very long in the direction of the ambient magnetic field compared to the transverse directions). The ambient magnetic field used in the simulations is a static solenoidal cylindrically symmetric 0.1 $Tesla$ field with a drop of ~ 20 % in the middle of the computational box (Fig. 4.4(a)), which provides the magnetic mirror configuration. The loss cone angle for a magnetic mirror can be estimated by Eq. (4.1), which in the case of $B_{max} = 0.1\ Tesla$ and $B_{min} = 0.08\ Tesla$ gives $\theta_{LC} \approx 63.4^o$.

The wave magnetic (See Fig. 4.4(b)) and electric (Fig. 4.4(c)) fields are calculated as functions of time and spatial coordinates using the 3D model for the parameters of the Experiment set 1 (See Table 3.1) with left-handed, right-handed and linear polarizations, and then are added to the ambient magnetic field. The radiating RMF source was 5 m away form the middle of the magnetic trap on the central axis. The induced wave field amplitude was adjusted in such a way that the amplitude of the magnetic field in the middle of the trap was $B = 1\ mTesla$, which is only 1% of the ambient magnetic field, and 5% of the drop of the magnetic field in the trap. Thus, the wave can be considered as a small amplitude field perturbation.

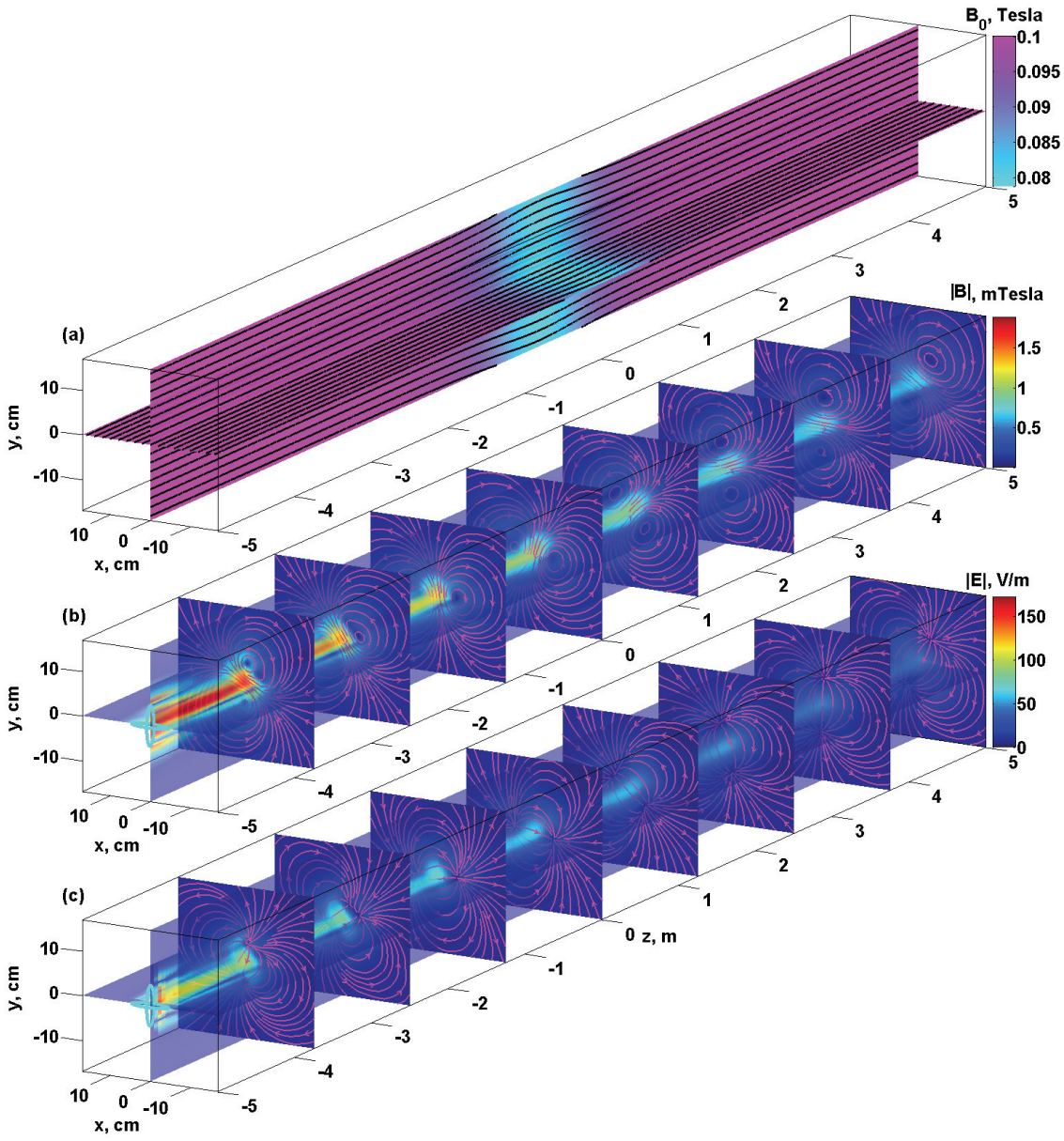

Figure 4.4: Setup of test particle simulations on scattering of trapped hot electrons by the waves generated by the rotating magnetic field source. The computational box size is 35 $cm \times 35$ $cm \times 10$ m. (a) - ambient magnetic field configuration (Solenoidal uniform magnetic field 0.1 $Tesla$ has a drop of 20 % in the middle, which provides the magnetic trap), the wave generated by the RMF source: The magnetic field (b) and electric field (c) configurations generated by the RMF source at an instant of time. Note the different scales on x, y and z-directions.

The wave generated in the experiment and modeled using the 3D simulations in Chapter 3 were launched in a uniform magnetic field of 0.1 $Tesla$. The presence of the weaker magnetic field region will affect the wave propagation, namely, the Alfvén speed will decrease in that region, as it is proportional to B_0. This results in decrease of the group velocity of the wave and increase of the wave energy density in the vicinity of the weaker ambient magnetic field. That would increase the wave amplitude by $\sim 10\%$. This effect is neglected in the simulations.

Figure 4.5 shows the ambient magnetic field profile (Fig. 4.5(a)) and the wave magnetic field components at an instant of time along the cental axis of the simulation box for the left-handed (Fig. 4.5(b)) and single-loop (Fig. 4.5(c)) cases.

The resulting magnetic and electric fields interact with the test particles in the simulations. The 22500 electrons were uniformly randomly distributed in the middle of the magnetic trap. The initial particle velocity distribution was with uniform distribution of the pitch-angle in the $80^o - 90^o$ range and monoenergetic kinetic energy of 1 keV. The interaction between the particles and background plasma was neglected. The wave in the model was also not affected by the energetic particles.

The tracing of the energetic electrons is done by numerically solving the full relativistic momentum equations in the electromagnetic field

$$\frac{d}{dt}\left(\frac{m_0\mathbf{v}}{\gamma}\right) = -e\left(\mathbf{E} + \mathbf{v}\times\mathbf{B}\right), \tag{4.2}$$

where $\gamma = \sqrt{1 - v^2/c^2}$ is the Lorentz relativistic factor. The numerical scheme to integrate the equation of motion is similar to the semi-implicit technique used in

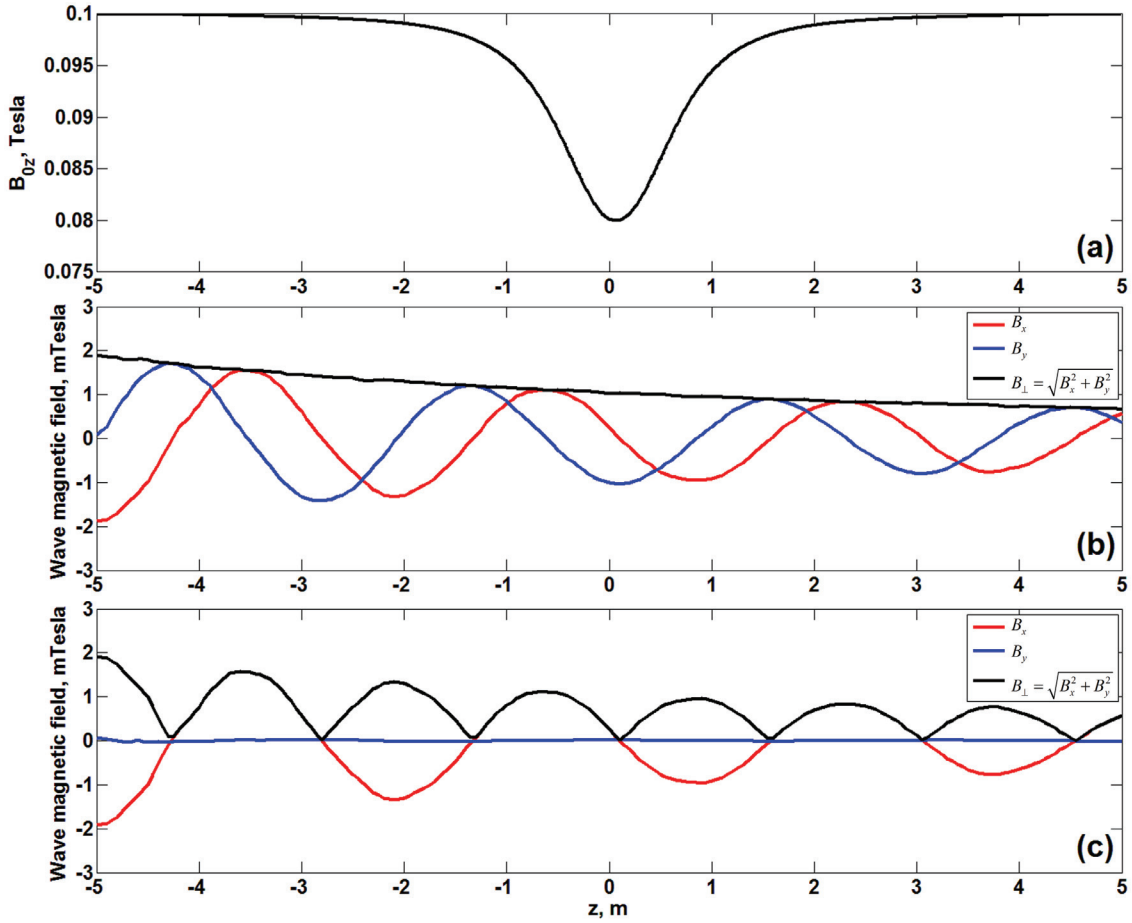

Figure 4.5: (a) - z-component of the ambient magnetic field, (b) - components of the wave magnetic field for left-handed polarization of the wave and (c) - the wave generated by the single loop at an instant of time along the z-axis.

particle codes [14] and in the relativistic proton tracing in the Earth magnetosphere [72], namely a time-centered leap-frog scheme. The time is discretized with the time-step δt, and the particle velocities ($\mathbf{v}_{n\pm\frac{1}{2}}$) are defined at half time steps and the particle positions ($\mathbf{r}_{n\pm1}$) are defined at integer time steps.

Introducing a variable $\mathbf{u} = \frac{\mathbf{v}}{\gamma}$, Eq. (4.2) in the discretized form becomes

$$\mathbf{u}_{n+\frac{1}{2}} - \mathbf{u}_{n-\frac{1}{2}} = \frac{e\delta t}{m}\left(\mathbf{E}_n + \frac{1}{2}\gamma_n\left(\mathbf{u}_{n+\frac{1}{2}} - \mathbf{u}_{n-\frac{1}{2}}\right) \times \mathbf{B}_n\right), \tag{4.3}$$

where the velocity $\mathbf{v}$ is treated with an implicit Crank-Nicholson method. In Eq. (4.3) the electric and magnetic fields are taken at the integer time step n. The relativistic Lorentz factor γ is found from the velocity $\mathbf{u}$ as

$$\gamma^2 = \frac{1}{1 + \frac{u^2}{c^2}}. \tag{4.4}$$

the particle positions are updated as

$$\mathbf{r}_{n+1} = \mathbf{r}_{n+1} + \gamma_{n+\frac{1}{2}} \mathbf{u}_{n+\frac{1}{2}} \delta t. \tag{4.5}$$

Eq. (4.3) in three dimensions is a system of three ordinary equations with respect to $\mathbf{u}_{n+\frac{1}{2}}$ components, which reduces to the inversion of a 3×3 matrix for each particle every time step, which is done analytically.

In order to calculate the particle trajectories accurately the characteristic time step δt should be at least one order smaller than the cyclotron period of the electron. Since the driving frequency of the wave is lower than the ion cyclotron frequency and the ion cyclotron frequency $m_i/m_e \approx 10^4$ times lower than the electron cyclotron frequency approximately one million steps are needed to resolve the electron dynamics during one wave period. As a matter of fact, in the present simulations 25 wave periods were resolved in time with $\sim 1.7 \times 10^7$ time steps. The sufficiently large number of steps are required to achieve high stability and accuracy of the integration technique. The use of the implicit Crank-Nicholson (CN) scheme for calculating velocities provides the required high stability of the algorithm, namely the kinetic energy of the particles does not grow over time, which would be the case if an explicit technique were used.

Absorbing boundary conditions are imposed on the system, that is when an electron hits any of the boundaries it is considered as lost and taken out from the simulations.

4.3 Results and discussion

The typical parameters of the electrons and the fields in the test particle simulations are presented in Table 4.1. Particles in a magnetic trap are involved in three periodic motions: the cyclotron motion, the bouncing motion along the ambient magnetic field lines between mirror points, and drift motion across the magnetic field lines due to the curvature of the latter. Any of these motions in principle can be in resonance with an electromagnetic wave. For our parameters the injected wave frequency was very low and could not satisfy the electron cyclotron resonance condition

$$k_{||}v_{||} - \omega = \frac{\Omega_{ce}}{\gamma}, \tag{4.6}$$

where ω and $k_{||}$ are the wave frequency and longitudinal wave number. For the driving frequency of $\omega = 0.54\Omega_{ci}$ ($\omega \ll \Omega_{ce}$)and the electron kinetic energy of 1 keV this condition becomes

$$k_{||}v_{||} \approx \frac{\omega}{V_A}v_{||} < \frac{\omega}{V_A}v \ll \Omega_{ce}. \tag{4.7}$$

The bouncing frequency between the mirror points for a fixed particle energy in general depends on the particle pitch angle. In our case the lowest bouncing frequencies for the particles with initial pitch angles $\sim 80^o$ are nearly two orders higher than the wave frequency. The third curvature-B drift motion can be in resonance with

the wave, but because the curvature of the ambient magnetic field lines is low in the middle of the trap, the period of the drift motion is too high compared to the wave period. The transverse wave length of the wave is much higher than the Larmor radius as well. Thus, the trapped electron scattering has a non-resonant nature.

Table 4.1: Parameters of electrons and wave fields in the test particle simulations.

Parameter	Value
Ions	He^+
Ambient magnetic field outside the trap	$0.1\ Tesla$
Ambient magnetic field in the middle of the trap	$0.08\ Tesla$
Electron cyclotron frequency Ω_{ce}	
$B_0 = 0.1\ Tesla$	$1.762 \times 10^{10} s^{-1}$
$B_0 = 0.08\ Tesla$	$1.410 \times 10^{10} s^{-1}$
Electron Larmor radius	
$B_0 = 0.1\ Tesla$	$1.067\ mm$
$B_0 = 0.08\ Tesla$	$1.334\ mm$
Electron kinetic energy	$1\ keV$
Electron velocity	$1.873 \times 10^7 m/s$
Length of the magnetic trap at half magnitude	$1.25\ m$
Typical electron bouncing period	$\sim 1 - 5 \times 10^{-7} s$
Typical electron curvature-B drift period	$\gg T_w$
Wave frequency ω	$1.294 \times 10^6 s^{-1}$
	$0.54\Omega_{ci}$
	$7.4 \times 10^{-5}\Omega_{ce}$
Longitudinal wave length	$\sim 2.95\ m$
Longitudinal phase velocity	$\sim 6 \times 10^5 m/s$
Transverse wave length	$\sim 18\ cm$

Figure 4.6(a) shows trajectory of a randomly chosen particle in the mirror magnetic field over a course of 25 wave periods, for the wave injection by a single-loop antenna. Figure 4.6(b) shows the trajectory of a randomly chosen particle for left-hand polarization RMF wave injection. The boxes shown are 5 m long in the z-direction and 10 cm in the x and y-directions. In the absence of the wave field a particle gyrates around magnetic field line with the cyclotron frequency, bounces

between the mirror points and slowly drifts around the center of trap due to the curvature of the magnetic field lines. The particle in the wave field generated by a single-loop antenna has more complicated trajectory (See Fig. 4.6(a)). Besides the gyration and bouncing motions it also drifts in the direction outwards of the center of the trap in the plane of oscillation of the wave magnetic field (in the center of the trap the wave magnetic field oscillates in the $x - z$-pane See Fig. 4.5(c)). In Fig. 4.6(b) the trajectory of one of the lost particles in the left-handed polarized rotating magnetic field is shown. In Fig. 4.7 the same trajectory of the lost particle is shown from three different perspectives. As time advances the pitch-angle of the particle decreases and the mirror points further diverge form the central plane of the magnetic mirror. Finally the particle pitch-angle reaches the loss cone and the particle becomes de-trapped. This is possible because the particle in the rotating magnetic field continuously experienced gradient in the transverse wave magnetic field, and possible breaking of the first adiabatic invariant.

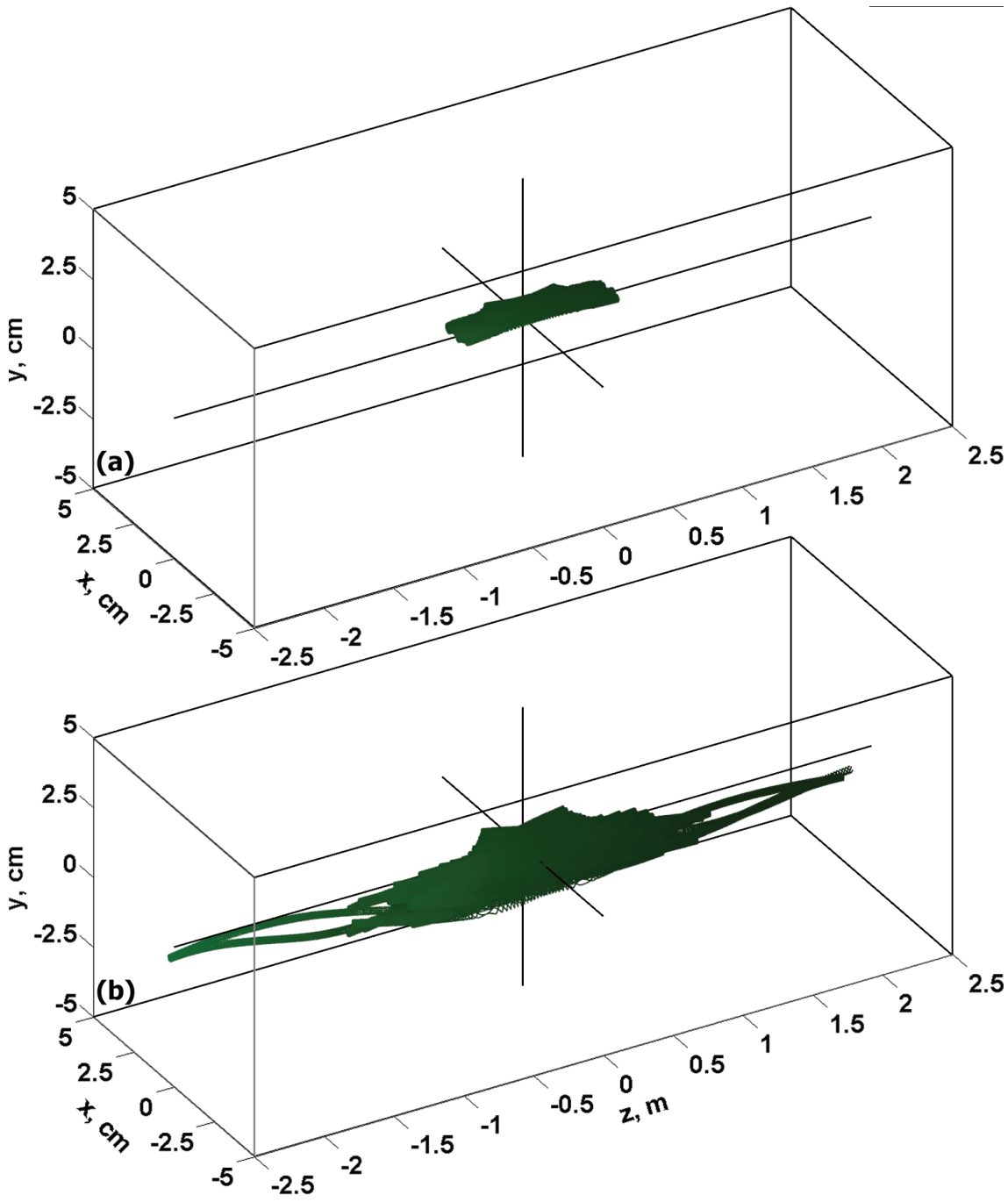

Figure 4.6: Trajectories of randomly chosen energetic electrons in the trap magnetic field in the presence of a wave generated by a single loop antenna (a), and of a wave generated by the the rotating magnetic field source with left-handed polarization (b).

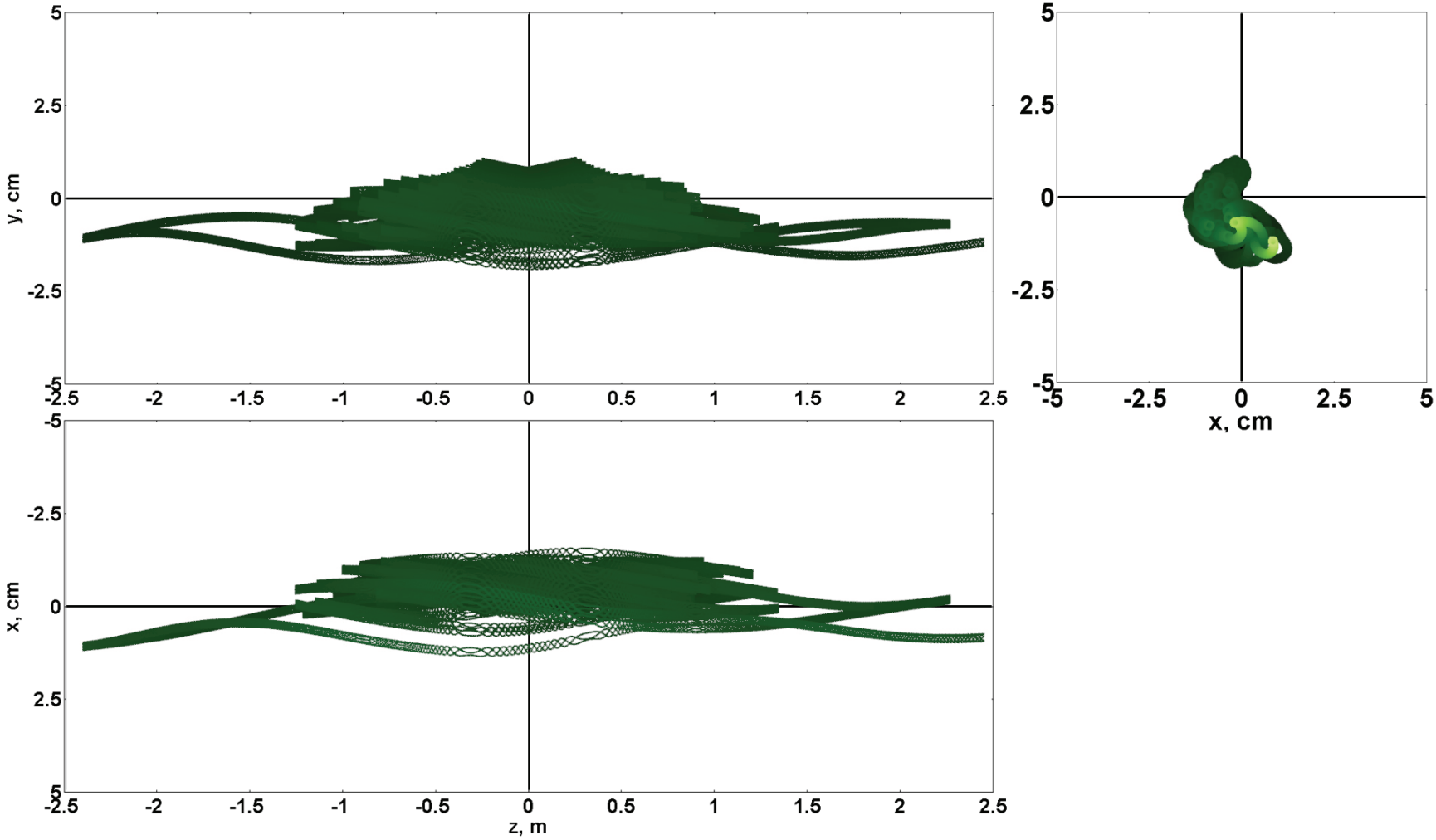

Figure 4.7: The trajectory of one of the lost particles in the test particle simulations with the wave generated by the rotating magnetic field source with left-handed polarization in three different projections.

In Fig. 4.8 the time dependence of ten randomly chosen particle pitch-angles interacting with the waves generated by the single-loop antenna (Fig. 4.8(a)) and by the rotating magnetic field source with left-handed (Fig. 4.8(b)) and right-handed (Fig. 4.8(c)) polarizations are shown. The pitch-angle is calculated as $\theta = \arctan\left(|v_{||}|/|v_{\perp}|\right)$ at the moment the particle crosses the the middle plain where the ambient magnetic field has its minimum. The pitch-angle presented in Fig. 4.8 is equivalent to the equatorial pitch-angle of the electrons trapped in the Earth's magnetosphere. One can see that the rotating magnetic field is more efficient in modifying the particle pitch-angle than the single-loop wave. Three of the ten particles in the simulations with the left-handed polarized wave (See Fig. 4.8(b)) reach the loss cone angle and are lost.

In Fig. 4.9 the time dependence of ten randomly chosen kinetic energies for the waves generated by the single-loop antenna (Fig. 4.9(a)) and by the rotating magnetic field source with left-handed (Fig. 4.9(b)) and right-handed (Fig. 4.9(c)) polarizations are shown. One can see that the amount of change of the particle kinetic energies is around 3% at most. The sinusoidal shape of the particle kinetic energy curves is synchronized with the wave period, and these oscillations are due to the wave electric field. Also one can see that the lost particle does not gain or lose any significant amount of energy before the scattering.

Figure 4.10 shows the distributions of the particles in the magnetic trap field after 25 wave periods for the wave generated by the single-loop antenna (Fig. 4.10(a)) and by the rotating magnetic field source with left-handed (Fig. 4.10(b)) and right-handed polarization (Fig. 4.10(c)). One can see significant difference between the

distributions in the single-loop antenna and rotating magnetic field cases. In the single-loop antenna case all the particles stay mainly in the vicinity of the center of the magnetic trap, while for the rotating magnetic field there is a noticeable spreading of the particle cloud in z-direction. Another feature of the particle distributions is the shape of the particle clouds in $x-y$ cross sections (See the insets in Fig. 4.6). In the rotating magnetic field case the test particle come to a co-rotational motion with wave magnetic field, while in the single-loop case the wave has nearly plane polarization.

In Fig. 4.11 the evolution of particle pitch-angle distributions calculated for all test particles in the course of 25 wave periods for single-loop antenna (Fig. 4.11(a)) and the rotating magnetic fields with left-handed (Fig. 4.11(b)) and the right-handed (Fig. 4.11(c)) polarization cases are shown. One can see significant difference in the particle distributions in single-loop and rotating magnetic field cases, namely, in the one-loop antenna case the distribution spread to lower pitch angles very slow compare to the rotating magnetic field cases. In the rotating magnetic field cases the distribution reaches the loss cone angle after approximately 10 wave periods. In the course of 25 wave periods not a single particle was lost in the simulations with the wave generated by the single-loop antenna, while for the rotating magnetic field more than 1/3 of the particles escaped the magnetic trap after 25 wave periods.

Although, the shear Alfvén waves generated by a RMF source had obvious effect on the hot electron populations both in the experiment (See Section 4.1) and test-particle simulations, the mechanism of the electron de-trapping is still not clear and requires additional investigation. The possible explanation of the de-trapping of

the electrons from the magnetic mirror configuration is breaking of the first adiabatic invariant by the RMF wave generated transverse magnetic field gradients.

The first adiabatic invariant is violated at least for some of the electrons that escaped the magnetic trap in the test-particle simulations. Since, the kinetic energy of the electrons is conserved with the variations of order $B_w/B_0 \sim 10^{-2}$, and the particle pitch angles was diverted form $\sim \pi/2$ to the loss cone, this means that the kinetic energy of the scattered particles was redistributed between the degrees of freedom increasing parallel component of the kinetic energy and decreasing the perpendicular one. Thus, the magnetic moment of these particles are reduced.

An electron in the presence of the low frequency shear Alfvén wave with sharp transverse magnetic field gradients on its cyclotron trajectory experiences magnetic field values which differ on opposite sides of cyclotron circle by of the order 10^{-4} for the test particle simulation parameters. The small variations of the magnetic field along the particle cyclotron trajectory in the case of the wave magnetic field unsynchronized with the particle motion can lead to a stochastic character of the particle phase trajectory, rather than a nearly periodic motion [58]. Quantitative characteristics of the lifetime of the particles in the magnetic mirror and behavior of the ensemble pitch angle distribution as a function of the wave parameters and particle energies as well as a criterion when the RMF wave interaction with hot electron population becomes efficient for pitch angle scattering require additional study.

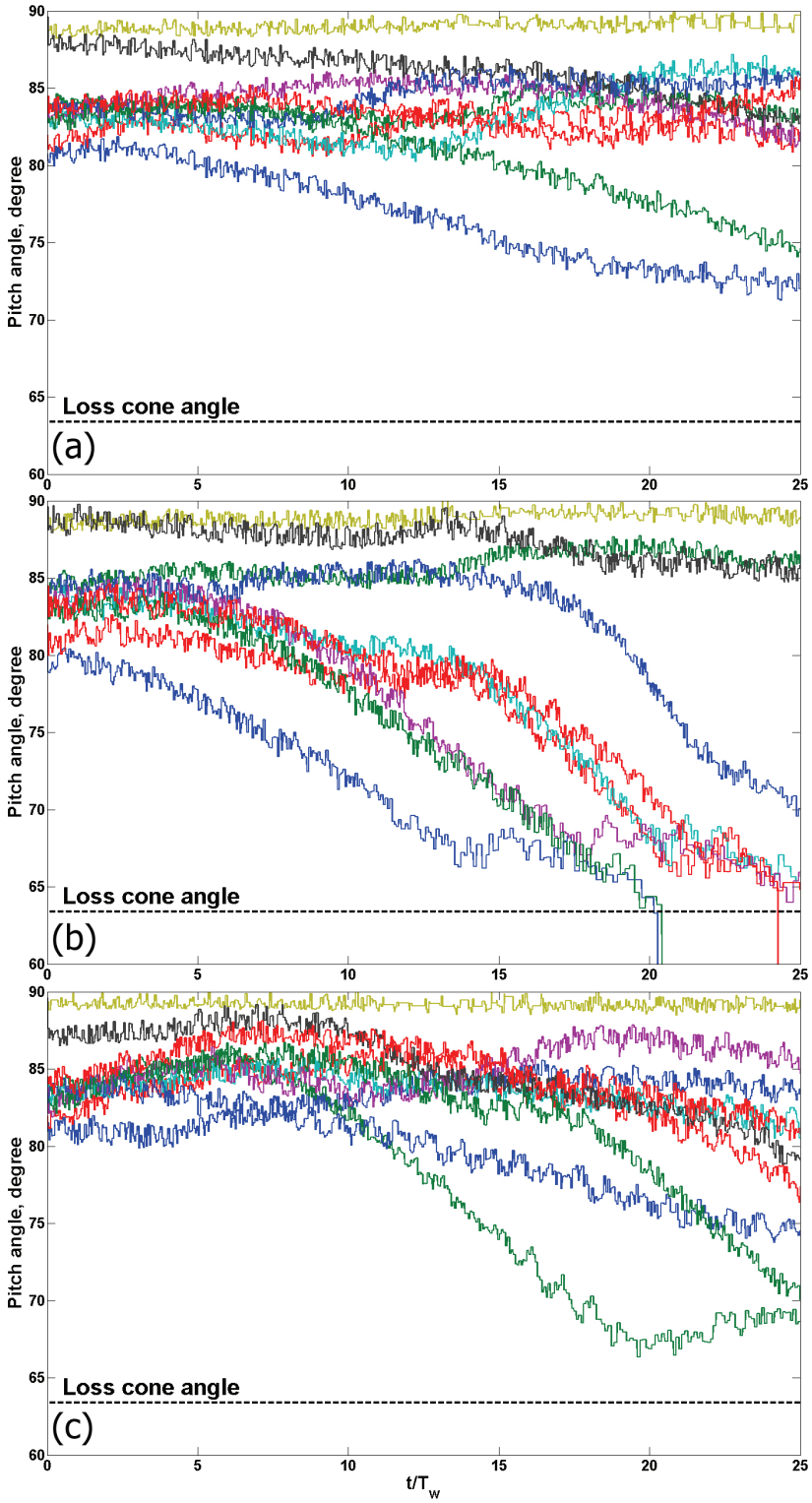

Figure 4.8: Evolution of pitch-angles of ten randomly chosen particles in the test particle simulations with the waves generated (a) - by the single-loop antenna, (b) - by the rotating magnetic field source with left-handed polarization, and (c) - by the rotating magnetic field source with right-handed polarization over the course of 25 wave periods.

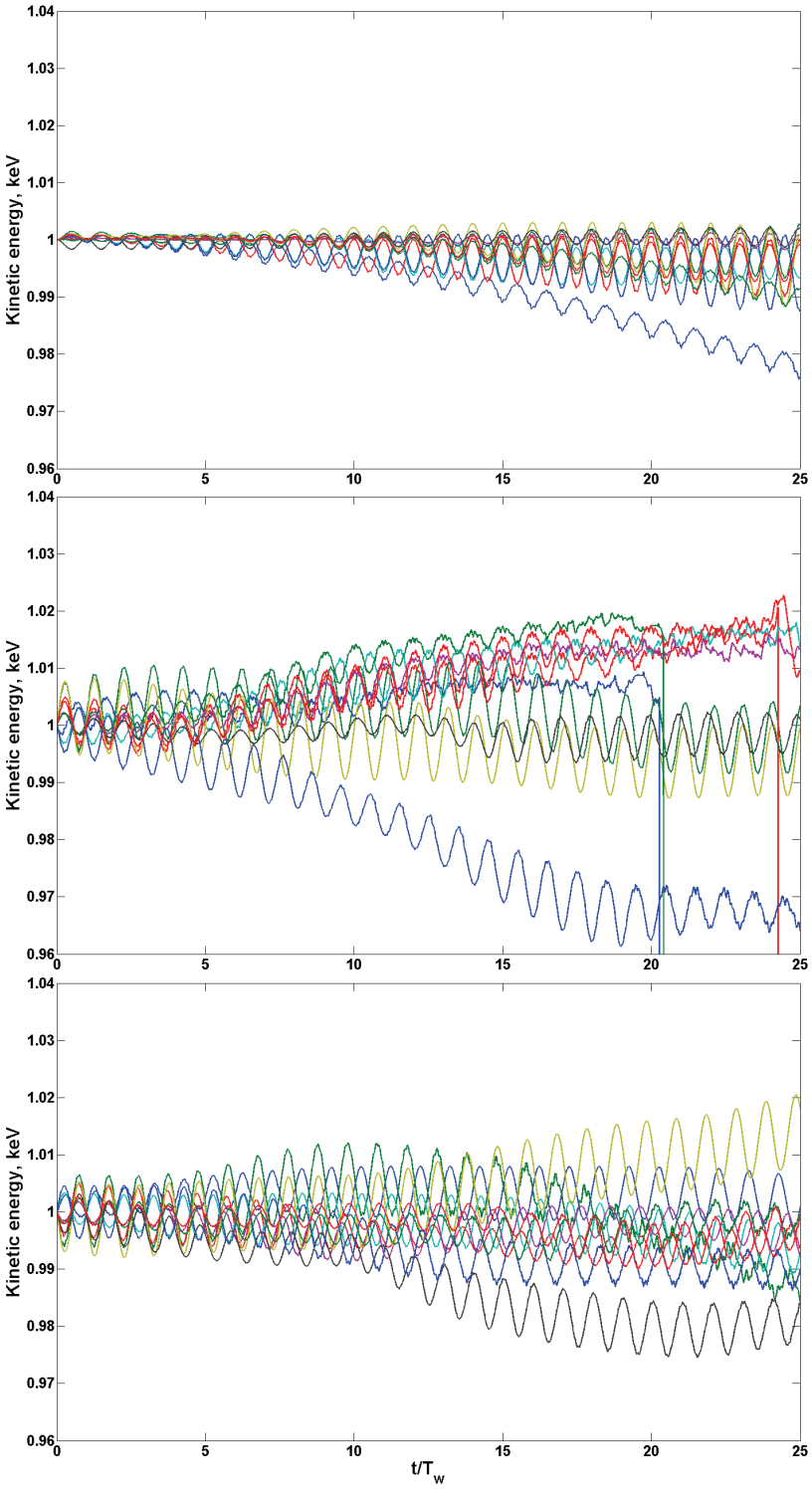

Figure 4.9: Evolution of kinetic energies of ten randomly chosen particles in the test particle simulations with the waves generated (a) - by the single-loop antenna, (b) - by the rotating magnetic field source with left-handed polarization, and (c) - by the rotating magnetic field source with right-handed polarization over the course of 25 wave periods.

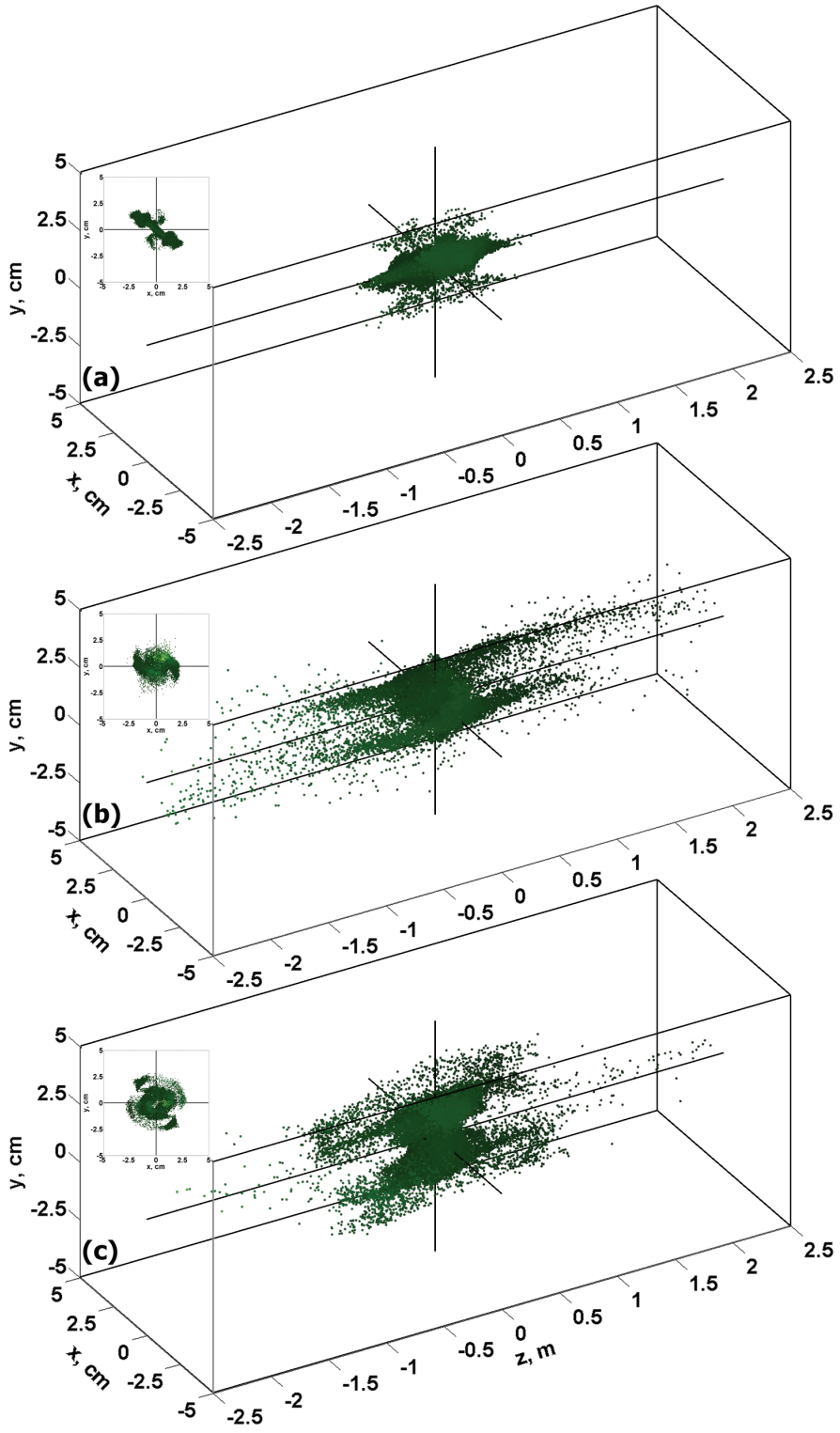

Figure 4.10: Distribution of the test particles in the magnetic trap after 25 wave periods for test particle simulations with the wave generated (a) - by the single-loop antenna, (b) - by the rotating magnetic field source with left-handed polarization, and (c) - by the rotating magnetic field source with right-handed polarization.

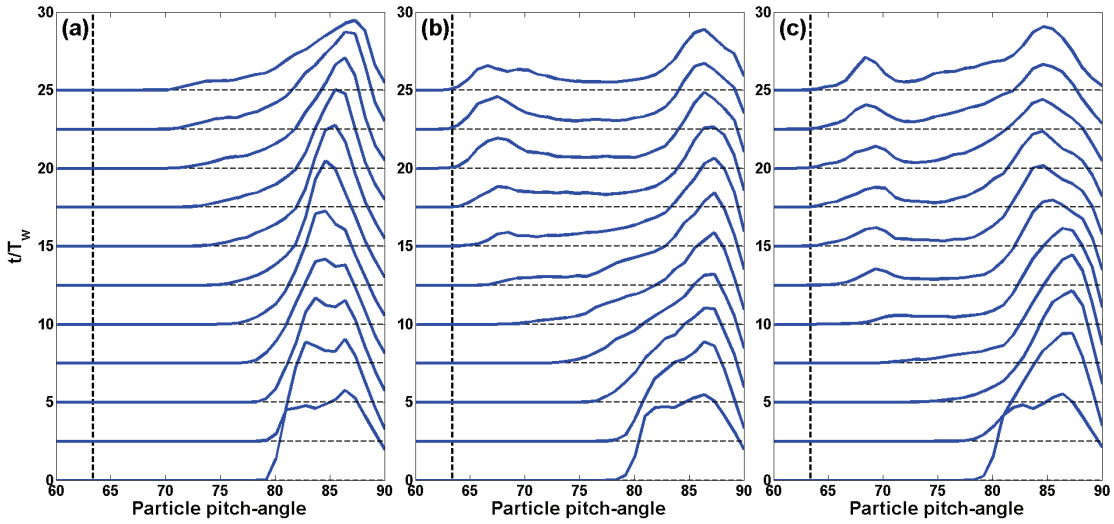

Figure 4.11: Evolution of particle pitch-angle distributions in the course of 25 wave periods for the wave generated (a) - by the single-loop antenna, (b) - by the rotating magnetic field source with left-handed polarization, and (c) - by the rotating magnetic field source with right-handed polarization. The vertical dashed lines represent loss cone angle.

Chapter 5

Conclusion

The interaction of magnetic fields rotating at a low frequency rate with magnetized plasmas was investigated experimentally, theoretically and by numerical simulations using 3D linear models. It was found that the RMF interaction with plasmas leads to efficient generation of whistler and shear Alfvén waves with arbitrary polarizations. Particular emphasis was placed in comparing the RMF generated waves with those generated by a traditional single magnetic loop radiation sources driven by low frequency alternating current.

The key results of the experiments and 3D simulations on generation of whistler and shear Alfvén waves by a RMF source are summarized bellow. In the whistler wave regime with the frequencies between the ion and electron cyclotron frequencies the main features are:

1. The RMF generated whistler waves have far fields with the perpendicular component of the magnetic field much larger than the parallel one. The maxima of the amplitude of the perpendicular component of the wave magnetic field are located along the field line corresponding to the center of the RMF antenna. The RMF generated wave magnetic field has right-handed or left handed circular polarization depending on the polarization of the RMF source. In the case of the whistler wave generated by a single-loop antenna the wave has nearly plane polarization.

2. The whistler wave structures generated by RMF source and single-loop antenna had significant field aligned plasma currents confined to the region of the source, leading to an efficient propagation along the ambient magnetic field very efficiently. These field aligned currents allows the whistler waves generated by both the one-loop and two-loop antennas to be confined by the ambient magnetic field without requiring nonlinear wave particle interaction and/or plasma density ducts. In the collisionless case the wave amplitude decays slowly along the ambient magnetic field with a rate determined by the leakage of the wave energy from the central axis to the periphery. This slow decay rate distinguishes the generation of the whistler waves by magnetic dipole and RMF antennas from the generation of whistler waves by electric dipole antennas. Small amplitude whistler waves generated by an electric dipole antenna in the absence of density ducts decay very rapidly along the ambient magnetic field even for collisionless plasmas, due to the fact that the radiated energy is mostly distributed along the resonance cone. On the other hand from the 3D simulations it was estimated that in the case of the waves generated by the RMF the wave energy, which stays within a radial column of width $\lambda_\perp$, is of order $75 - 85$ % (depending on the wave frequency).

3. The values of the effective collision frequency estimated from the parameters of the experiment and the 3D EMHD model for the best match with the experiments were found to be very close. Thus, the whistler wave generation by RMF source in the experiments along with the 3D EMHD model can be used for estimating an effective electron collision frequency.

4. The RMF driven whistler waves have very high transverse wave number

$k_\perp$ compared to the parallel wave number $k_{||}$. As a result significant magnetic field gradients are generated in the direction perpendicular to the ambient magnetic field. This has important implications for the non-resonant pitch angle scattering of energetic charged particles trapped in the radiation betls.

In the case of shear Alfvén waves with the frequencies below the ion cyclotron frequency the main features a s follows.

1. It was demonstrated in the experiments and three-dimensional cold two-fluid model simulations that the RMF antenna composed of two independent coils with alternating currents set $\pm 90^o$ out of phase can efficiently generate shear Alfvén waves in magnetized plasmas with high transverse wave number $k_\perp$ and arbitrary polarization. The wave magnetic field generated by the RMF source is mainly perpendicular to the ambient magnetic field, similar to the RMF generated whistler waves.

2. The spatio-temporal wave structures are similar to those generated in the whistler regime. It was shown in the experiment and calculated using the 3D model that the SAWs generated by the RMF carry significant field aligned plasma currents which propagate parallel to the ambient magnetic field lines without noticeable spreading in the transverse direction. The RMF generated SAWs found to be very efficient for transferring energy along the ambient magnetic field. The exponential decay rate of the wave amplitude along the ambient magnetic field was found to be determined by the collisions. Unlike the whistler waves generated by RMF which loose the energy due to leakage from the central line to the periphery, the SAWs in the case of collisionless plasmas have nearly constant amplitude along the ambient

magnetic field.

3. The dependence of the amplitude of the wave magnetic field on the driving frequency was studied. It was shown that the amplitude of the RMF generated SAW increases with the frequency reaches its maximum at $\sim 0.9\Omega_{ci}$ and then drop to zero approaching the ion cyclotron frequency. The dependence measured in the experiment and calculated from the 3D model are very close to each other except for the frequencies very close to the ion cyclotron frequency. This can be explained by the fact that the resonant wave-particle interaction and magnetosonic wave mode are not included in the 3D model.

4. The power of the magnetic filed of the RMF generated wave was calculated from the experimental data and found to be $\sim 250\ W$ for the driving frequency $\omega = 0.54\Omega_{ci}$, and the current magnitudes $I_1 = I_2 = 600\ A$ (that corresponds to magnetic moment $M \approx 11.5\ A \cdot m^2$). The power found in the 3D simulations for the magnetic field for the experimental parameters was $253\ W$, which differs from the experimental value only by $\sim 1\%$. The wave power corresponding to the other components of the wave, namely, the kinetic energy of electron and ion fluids calculated from 3D simulations are $P_{Ke} = 26\ W$, and $P_{Ki} = 500\ W$, respectively. Thus, the energy of the wave is distributed as: $\sim 1/2$ - electromagnetic field energy, $\sim 1/2$ - the kinetic energy of ions, and $\sim 2.5\%$ - the kinetic energy of electrons.

5. Similar to the RMF generated whistler waves the SAWs have high transverse wave number $k_\perp$ determined by the RMF antenna size resulting in the transverse magnetic field gradients.

Simulations using the 3D two-fluid model were compared in detail with the

experimental results for wide ranges of the experimental parameters and showed good agreement. This shows good predictive capability of the 3D model, which can be used for parameters that are hard to achieve in laboratory plasmas or space plasma configurations.

A key motivation for the experiment on the generation of the whistler and shear Alfén waves by a RMF source and the development of the 3D models was the possibility of use of the waves for non-resonant pitch angle scattering of highly energetic trapped particles in the Earth's inner radiation belt by injecting of such waves from satellites inside the radiation belts. Chapter 4 discussed the effect of the low frequency ($\omega \ll \Omega_{ce}$) RMF generated SAWs on the population of highly energetic electrons. The problem was studied by the test particles simulations in which the full relativistic equation of motion of the particles in the wave electromagnetic field was numerically integrated for 1 keV electrons, and in the experiments conducted in LAPD-machine. It was shown that the low frequency RMF generated SAWs, with both the right-handed and left-handed polarizations, are more efficient for the pitch angle scattering of the energetic electrons, which are off resonance with the wave, than the waves generated by the single-loop antenna. The mechanism of the non-resonant pitch angle scattering of the energetic electrons by the low frequency RMF generated waves is probably breaking of the first adiabatic invariant of the hot particles due to a presence of the wave transverse magnetic field gradients.

The non-resonant pitch angle scattering has one significant advantage over the resonant one. For efficient resonant scattering the resonance condition should be satisfied, which can be achieved for only a small fraction of the particle population

with very specific set of parameters and/or in a very localized volume because of the changing values of the ambient magnetic field [4]. While for the non-resonant pitch angle scattering due to presence of the transverse magnetic field gradients there is no such condition to satisfy, and virtually all the energetic electron population is affected by the wave magnetic field. This makes the low frequency wave generated by RMF approach to the precipitation of inner radiation belt electrons promising.

Appendix A

Cold electron magnetohydrodynamics model in a static background magnetic field

A.1 General EMHD model equations

In the Appendix the general model which was used to simulate the propagation of whistler waves generated by current sources is described. Following the electron magnetohydrodynamics (EMHD) approach [39,53,55,79] we start from the Maxwell equations

$$\nabla \times \mathbf{E} = -\frac{1}{c}\frac{\partial \mathbf{B}}{\partial t}, \tag{A.1}$$

$$\nabla \times \mathbf{B} = \frac{1}{c}\frac{\partial \mathbf{E}}{\partial t} + \frac{4\pi}{c}\mathbf{J}, \tag{A.2}$$

and electron momentum equation in the frames of the cold fluid approach

$$m_e \frac{d\mathbf{v}}{dt} = -e\mathbf{E} - \frac{e}{c}\mathbf{v} \times \mathbf{B} - m_e \nu_e \mathbf{v}, \tag{A.3}$$

where $\mathbf{E}$ and $\mathbf{B}$ are electric and magnetic fields, $\mathbf{v}$ is the velocity of the cold electron fluid, $\mathbf{J} = -en\mathbf{v} + J_{ext}$ is a current density, including two parts, *viz.*, the plasma current density and external current density $\mathbf{J}_{ext}$, e and m_e are the electron charge and mass, and ν_e is an effective frequency of electron collisions either with ions or neutrals. The plasma density $n = n(\mathbf{x}, t)$ is a function of space coordinates and time, which is determined not by the wave propagation, but by some external

factors. For example, the time dependence of the plasma density can be due to the electron-ion recombination in the afterglow of a gas discharge. In that cense the $n = n(\mathbf{x}, t)$ should be treated as external given function.

One of the key approximations of the electron magnetohydrodynamics model is the neglecting of the ion motion. This approximation works fairly well for the driving frequencies ω in a range $\Omega_{ci} < \omega_{LH} \ll \omega < \Omega_{ce}$, where Ω_{ci} and Ω_{ce} are the ion and electron cyclotron frequencies, and ω_{LH} is the lower-hybrid resonance frequency ($\omega_{LH} = \sqrt{\Omega_{ci}\Omega_{ce}}$). In that case the ions due to the big mass do not respond to the high frequency field perturbations and can be treated as motionless neutralizing background. Below the lower-hybrid resonance the EMHD approach is not valid in general, but still can be used in some cases (See Chapter 2). The second approximation which is used in the frames of EMHD model is the neglecting of the displacement current in the Ampere's law (A.2). This assumption is based on two independent points. The component of the displacement current perpendicular to the wave vector $\mathbf{k}$ can be neglected, because the whistlers are slow waves, *i.e.*, $\omega/k \ll c$. The component of the displacement current parallel to the wave-vector $\mathbf{k}$ can be neglected, when the driving frequency ω is much less than the electron plasma frequency ω_{pe}, which is the case in the most of laboratory and space plasmas ($\Omega_{ce} \ll \omega_{pe}$). In that case the whistler wave is quasi-neutral, *i.e.*, the wave does not influence the electron and ion densities ($n_e = n_i = n(\mathbf{x})$). The assumption quasi-neutrality removes the necessity to resolve Poisson's equation to determine the electrostatic field.

Based on this assumptions the general equations covering the cold electron

fluid motion for the frequency range $\Omega_{ci} < \omega_{LH} \ll \omega < \Omega_{ce}$ are

$$\begin{aligned} \nabla \times \mathbf{E} &= -\frac{1}{c}\frac{\partial \mathbf{B}}{\partial t}, & \text{(A.4)} \\ \nabla \times \mathbf{B} &= -\frac{4\pi}{c} en\mathbf{v} + \frac{4\pi}{c}\mathbf{J}_{ext}, & \text{(A.5)} \\ \frac{\partial \mathbf{v}}{\partial t} + (\mathbf{v}\cdot\nabla)\,\mathbf{v} &= -\frac{e}{m_e}\mathbf{E} - \frac{e}{m_e c}\mathbf{v}\times\mathbf{B} - \nu_e \mathbf{v}. & \text{(A.6)} \end{aligned}$$

This is the closed system of partial differential equations on $\mathbf{B}$, $\mathbf{E}$ and $\mathbf{v}$. Before the solving it we introduce the normalization which was used in the implemented code. Let decompose the magnetic field $\mathbf{B}$ as a sum $\mathbf{B} = \mathbf{B}_0 + \delta\mathbf{B}$, where $\mathbf{B}_0$ is the ambient magnetic field, which is not necessary uniform, but has typical scale of B_0, and $\delta\mathbf{B}$ is the wave field perturbation. The normalization is naturally determined by two frequencies. The electron plasma frequency $\omega_{pe} = \sqrt{4\pi n_0 e^2/m_e}$ determines the length-scale $d_e = c/\omega_{pe}$, which is electron skin-depth. The electron cyclotron frequency $\Omega_{ce} = (eB_0)\,/\,(cm_e)$ determines the time-scale $T = \Omega_{ce}^{-1}$. Using the scales the normalized variables become

$$\overline{t} = \frac{t}{T}, \quad \overline{\mathbf{x}} = \frac{\mathbf{x}}{d_e}, \quad \overline{\mathbf{v}} = \frac{T\mathbf{v}}{d_e}, \quad \overline{\mathbf{B}} = \frac{\mathbf{B}}{B_0}, \quad \overline{\mathbf{E}} = \frac{cT\mathbf{E}}{d_e B_0}, \quad \overline{\nu} = \frac{\nu_e}{\Omega_{ce}}, \quad \overline{n} = \frac{n}{n_0}. \quad \text{(A.7)}$$

We can then rewrite Eqs. (A.4),(A.5),(A.6) as

$$\begin{aligned} \overline{\nabla}\times\overline{\mathbf{E}} &= -\frac{\partial \overline{\mathbf{B}}}{\partial \overline{t}}, & \text{(A.8)} \\ \overline{\nabla}\times\overline{\mathbf{B}} &= -\overline{n}\overline{\mathbf{v}} + 4\pi\overline{\mathbf{J}}_{ext}, & \text{(A.9)} \\ \frac{\partial \overline{\mathbf{v}}}{\partial \overline{t}} &= -\left(\overline{\mathbf{v}}\cdot\overline{\nabla}\right)\overline{\mathbf{v}} - \overline{\mathbf{E}} - \overline{\mathbf{v}}\times\overline{\mathbf{B}} - \overline{\nu}\overline{\mathbf{v}}. & \text{(A.10)} \end{aligned}$$

From this point to the end only dimensionless variables are used, so let drop the bars in the remain sections of the Appendix A. We decompose the electric $\mathbf{E}$

and magnetic $\mathbf{B}$ fields in the following way

$$\mathbf{E} = \mathbf{E}' + \mathbf{E}_{ext}, \quad \mathbf{B} = \mathbf{B}_0 + \mathbf{B}' + \mathbf{B}_{ext}, \tag{A.11}$$

where $\mathbf{B}_0$ is the ambient magnetic field, $\mathbf{E}'$ and $\mathbf{B}'$ are electric and magnetic fields associated with the wave, and $\mathbf{E}_{ext}$ and $\mathbf{B}_{ext}$ are localized electric and magnetic fields corresponding to the external currents. The decomposition (A.11) is arbitrary, and the only reason we do this is because we want the $\mathbf{E}_{ext}$ and $\mathbf{B}_{ext}$ fields to take care of all singularities which can be introduced to the system by infinitely thin external current elements. Using the field decomposition (A.11) we can rewrite the equations (A.8),(A.9), and (A.10) as

$$\nabla \times \mathbf{E}' + \nabla \times \mathbf{E}_{ext} = -\frac{\partial \mathbf{B}'}{\partial t} - \frac{\partial \mathbf{B}_{ext}}{\partial t}, \tag{A.12}$$

$$\nabla \times \mathbf{B}' + \nabla \times \mathbf{B}_{ext} = -n\mathbf{v} + 4\pi \mathbf{J}_{ext}, \tag{A.13}$$

$$\frac{\partial \mathbf{v}}{\partial t} = -\left(\mathbf{v} \cdot \nabla\right)\mathbf{v} - \mathbf{E}' - \mathbf{E}_{ext} - \tag{A.14}$$

$$-\mathbf{v} \times \left(\mathbf{B}_0 + \mathbf{B}' + \mathbf{B}_{ext}\right) - \nu \mathbf{v},$$

where we used the fact that for a static magnetic field $\nabla \times \mathbf{B}_0 = 0$ and $\partial \mathbf{B}_0 / \partial t = 0$.

Let the $\mathbf{E}_{ext}$ and $\mathbf{B}_{ext}$ fields are determined by

$$\mathbf{E}_{ext} = -\frac{\partial}{\partial t}\mathbf{A}_{ext}, \tag{A.15}$$

$$\mathbf{B}_{ext} = \nabla \times \mathbf{A}_{ext}, \tag{A.16}$$

where the vector potential $\mathbf{A}_{ext}$ satisfies the equation

$$\nabla \times \nabla \times \mathbf{A}_{ext} + \mathbf{A}_{ext} = 4\pi \mathbf{J}_{ext}. \tag{A.17}$$

Eq. (A.17) should be resolved for the external current configuration. The ways of solving Eq. (A.17) are described in Appendix C. If the external currents do not move in time Eq. (A.17) should be resolved only ones.

Using Eqs. (A.15), (A.16) and (A.17), Eqs. (A.12),(A.13) and (A.14) can be written as

$$\frac{\partial \mathbf{v}}{\partial t} = \frac{1}{n}\left(\nabla \times \nabla \times \mathbf{E}' + \frac{\partial}{\partial t}\mathbf{A}_{ext} - \frac{\partial n}{\partial t}\mathbf{v}\right), \tag{A.18}$$

$$\nabla \times \mathbf{B}' = -n\mathbf{v} + \mathbf{A}_{ext}, \tag{A.19}$$

$$\begin{aligned} \nabla \times \nabla \times \mathbf{E}' + n\mathbf{E}' = & -n\left(\mathbf{v}\cdot\nabla\right)\mathbf{v} + (n-1)\frac{\partial}{\partial t}\mathbf{A}_{ext} - \\ & -n\mathbf{v}\times\left(\mathbf{B}_0 + \mathbf{B}' + \nabla\times\mathbf{A}_{ext}\right) + \left(\frac{\partial n}{\partial t} - \nu n\right)\mathbf{v}. \end{aligned} \tag{A.20}$$

Thus, the system of equations covering the motion of cold electron fluid reduces to one evolution equation (A.18) and two elliptical equations (A.19) and (A.20). We can construct the algorithm for numerical integration of the system in the following way. For given $\mathbf{E}'$, $\mathbf{B}'$ and $\mathbf{v}$ at instant $t = t_n$, using Eq. (A.18), we can perform one step integration in time to get $\mathbf{v}$ at instant $t = t_{n+1}$. This new value of $\mathbf{v}$ is used to obtain $\mathbf{B}'$ and $\mathbf{E}'$, using Eqs. (A.19) and (A.20), respectively, and the process is repeated. This approach to the solution Eqs. (A.18), (A.19) and (A.20) in simplified form was used in [55, 79]. The advantage of this approach is that this algorithm can handle the fully nonlinear problem. One of the problems with this method is that we need to resolve two elliptical equations in three dimensions each time step. We better use some advanced and fast technics to do that. Since the time step should be small enough to resolve the electron cyclotron frequency, we have to perform many thousands steps to resolve at least one period of oscillation for the

case when the driving frequency $\omega \ll \Omega_{ce}$. This arise the strong requirements for the time integration algorithm of Eq. (A.18), namely, the high stability and high accuracy of the time integrator.

A.2 Linear whistler waves in homogenous case: an analytical solution

Consider the case of small magnitude waves $\delta\mathbf{B} \ll \mathbf{B}_0$ in a homogeneous plasma, when the plasma density does not depend on space coordinates and time, and uniform ambient magnetic field $\mathbf{B}_0 = const$. In that case all nonlinear terms in the system of Eqs. (A.18), (A.19) and (A.20) can be neglected and the system reduces to

$$\frac{\partial \mathbf{v}}{\partial t} = \nabla \times \nabla \times \mathbf{E}' + \frac{\partial}{\partial t}\mathbf{A}_{ext}, \tag{A.21}$$

$$\nabla \times \mathbf{B}' = -\mathbf{v} + \mathbf{A}_{ext}, \tag{A.22}$$

$$\nabla \times \nabla \times \mathbf{E}' + \mathbf{E}' = -\mathbf{v} \times \mathbf{b} - \nu\mathbf{v}, \tag{A.23}$$

where $\mathbf{b}$ is unit vector in the direction of $\mathbf{B}_0$. In that case an analytical solution of the system of Eqs. (A.21), (A.22), (A.23) can be obtained in the Fourier domain.

We want to find a solution of the system in three dimensions on a discreet grid, so it is natural to use as a representation of the solutions for $\mathbf{v}$, $\mathbf{B}'$ and $\mathbf{E}'$ the discreet Fourier sums

$$\mathbf{v} = \sum_{\mathbf{k}} \mathbf{v}^* e^{i\mathbf{k}\cdot\mathbf{x}}, \tag{A.24}$$

$$\mathbf{B}' = \sum_{\mathbf{k}} \mathbf{B}^* e^{i\mathbf{k}\cdot\mathbf{x}}, \tag{A.25}$$

$$\mathbf{E}' = \sum_{\mathbf{k}} \mathbf{E}^* e^{i\mathbf{k}\cdot\mathbf{x}}, \tag{A.26}$$

where asterisks denote the Fourier components. We select the reference frame in such a way that the ambient magnetic field $\mathbf{B}_0$ is oriented along the z-axis ($\mathbf{b} = \mathbf{e}_z$). Than in the Fourier domain from Eqs. (A.22) and (A.23) we get the magnetic and electric field components $\mathbf{B}^*$, $\mathbf{E}^*$ expressed through the velocity $\mathbf{v}^*$

$$\mathbf{B}^* = \frac{i\mathbf{k} \times (-\mathbf{v}^* + \mathbf{A}^*_{ext})}{k^2}, \tag{A.27}$$

$$\mathbf{E}^* = -\frac{\mathbf{v}^* \times \mathbf{e}_z + \nu\mathbf{v}^* + \mathbf{k}\,(\mathbf{k} \cdot (\mathbf{v}^* \times \mathbf{e}_z))}{1 + k^2}. \tag{A.28}$$

Using Eq. (A.28) we can exclude the electric field from Eq. (A.21) and get the closed system for the velocity $\mathbf{v}^*$

$$\frac{\partial \mathbf{v}^*}{\partial t} = \frac{-k^2\,(\mathbf{v}^* \times \mathbf{e}_z + \nu\mathbf{v}^*) + \mathbf{k}\,(\mathbf{k} \cdot (\mathbf{v}^* \times \mathbf{e}_z))}{1 + k^2} + \frac{\partial}{\partial t}\mathbf{A}^*_{ext}. \tag{A.29}$$

In the component form Eq. (A.29) is a 3×3 linear system, which can be written as

$$\frac{\partial \mathbf{v}^*}{\partial t} = L\,(\mathbf{k})\,\mathbf{v}^* + \frac{\partial}{\partial t}\mathbf{A}^*_{ext}, \tag{A.30}$$

where

$$L\,(\mathbf{k}) = \frac{1}{1 + k^2}\begin{pmatrix} -\nu k^2 + k_x k_y & -k^2 + k_x^2 & 0 \\ k^2 - k_y^2 & -\nu k^2 - k_x k_y & 0 \\ -k_y k_z & k_x k_z & -\nu k^2 \end{pmatrix} \tag{A.31}$$

is the system matrix, and $k^2 = k_x^2 + k_y^2 + k_z^2$, while $\mathbf{v}^*$ and $\mathbf{A}^*_{ext}$ are treated as column vectors. Solution of Eq. (A.30) can be written in the form

$$\begin{aligned} \mathbf{v}^*\,(\mathbf{k}, t) = {} & U\,(\mathbf{k})\,e^{\Lambda(\mathbf{k})t}U^{-1}\,(\mathbf{k})\,\mathbf{v}^*\,(\mathbf{k}, 0) + \\ & + U\,(\mathbf{k})\,e^{\Lambda(\mathbf{k})t}\int_0^t e^{-\Lambda(\mathbf{k})t'}U^{-1}\,(\mathbf{k})\,\frac{\partial}{\partial t'}\mathbf{A}^*_{ext}\,(\mathbf{k}, t')\,dt', \end{aligned} \tag{A.32}$$

where $\Lambda\,(\mathbf{k})$ and $U\,(\mathbf{k})$ are diagonal matrix of eigen values and modal matrix that consists of columns of corresponding eigen vectors, which decompose the system

matrix (A.31) as

$$L = U\Lambda U^{-1} \tag{A.33}$$

and do not depend on time. Thus, for a given geometry of the external currents they can be computed only ones.

Particularly, in the case of harmonically driven field and zero initial plasma current we get

$$\frac{\partial}{\partial t}\mathbf{A}^*_{ext}(\mathbf{k},t) = \mathbf{F}^*(\mathbf{k})\, e^{i\omega t}, \qquad \mathbf{v}^*(\mathbf{k},t) = 0, \tag{A.34}$$

and Eq. (A.32) transforms into

$$\mathbf{v}^*(\mathbf{k},t) = U(\mathbf{k})\, M(\mathbf{k},t)\, U^{-1}(\mathbf{k})\, \mathbf{F}^*(\mathbf{k}), \tag{A.35}$$

where

$$M(\mathbf{k},t) = \left(e^{\Lambda(\mathbf{k})t} - e^{i\omega t} I\right)\left(\Lambda(\mathbf{k}) - i\omega I\right)^{-1}, \tag{A.36}$$

where I is 3×3 identity matrix.

To find the eigen values of $L(\mathbf{k})$ we need to solve characteristic equation which can be written in the form

$$\left[\left(\lambda + \frac{\nu k^2}{1+k^2}\right)^2 + \left(\frac{k k_z}{1+k^2}\right)^2\right]\left(\lambda + \frac{\nu k^2}{1+k^2}\right) = 0. \tag{A.37}$$

This gives the eigen values

$$\lambda_{1,2} = -\frac{\nu k^2}{1+k^2} \mp i\frac{k k_z}{1+k^2}, \qquad \lambda_3 = -\frac{\nu k^2}{1+k^2}. \tag{A.38}$$

The fist pair of complex conjugate roots describes wave propagation in $\pm\mathbf{e}_z$ directions with the frequency

$$\omega(\mathbf{k}) = -Im\{\lambda_{1,2}\} = \pm\frac{k k_z}{1+k^2} \tag{A.39}$$

and uniform attenuation

$$Re\{\lambda_{1,2}\} = Re\{\lambda_3\} = \frac{\nu k^2}{1+k^2}. \tag{A.40}$$

Finally we get the linear dispersion relation for the whistler waves

$$\left(\omega + i\frac{\nu k^2}{1+k^2}\right)^2 = \left(\frac{k k_{||}}{1+k^2}\right)^2 \tag{A.41}$$

which in the non-dissipative case become

$$\omega = \frac{k k_{||}}{1+k^2}. \tag{A.42}$$

This is so-called quasi-longitudinal dispersion relation [42] with $k_{||} = k_z$. In the case of a plane whistler waves propagating along the ambient magnetic $k = k_{||}$, that is the wave vector $\mathbf{k}$ has no transverse component ($k_\perp = 0$), we get the well known whistler dispersion relation

$$\omega = \frac{k^2}{1+k^2}. \tag{A.43}$$

Eq. (A.42) can be written as

$$\omega = \frac{k_{||}\sqrt{k_{||}^2 + k_\perp^2}}{1 + k_{||}^2 + k_\perp^2}. \tag{A.44}$$

For $k_{||}^2$ has two solutions. One of them corresponds to the evanescent wave and plays significant role for the near field structure. The second root

$$k_{||}^2 = \frac{-k_\perp^2 + 2\left(1+k_\perp^2\right)\omega^2 + \sqrt{k_\perp^4 + 4\omega^2\left(1+k_\perp^2\right)}}{2\left(1-\omega^2\right)} \tag{A.45}$$

describes propagating mode. To calculate the value of the longitudinal wave length $\lambda_{||} = 2\pi/k_{||}$ we need to know the value of normal component of wave vector $k_\perp$ which is mainly determined by the source of radiation. For example, if we have

an oscillating electric dipole oriented perpendicular to the ambient magnetic field its size will be roughly half the wave length in the transverse direction. In the case of the magnetic dipole the perpendicular wave-length is also determined by the antenna size.

A.3 Nonlinear whistler waves in homogeneous plasma

Consider the fully nonlinear system of equations (A.18), (A.19), (A.20) in the case of uniform plasma density n. In that case in dimensionless variables $n = const = 1$, and the system (A.18), (A.19), (A.20) reduces to

$$\frac{\partial \mathbf{v}}{\partial t} = \nabla \times \nabla \times \mathbf{E}' + \frac{\partial}{\partial t}\mathbf{A}_{ext}, \tag{A.46}$$

$$\nabla \times \mathbf{B}' = -\mathbf{v} + \mathbf{A}_{ext}, \tag{A.47}$$

$$\nabla \times \nabla \times \mathbf{E}' + \mathbf{E}' = -\left(\mathbf{v} \cdot \nabla\right)\mathbf{v} - \mathbf{v} \times \left(\mathbf{B}_0 + \mathbf{B}' + \nabla \times \mathbf{A}_{ext}\right) - \nu\mathbf{v}. \tag{A.48}$$

Before introducing the way of solving the fully nonlinear system let simplify the equation (A.48). Let consider the convective term $\left(\mathbf{v} \cdot \nabla\right)\mathbf{v}$. Using identity

$$\frac{1}{2}\nabla \mathbf{v}^2 = \frac{1}{2}\nabla\left(\mathbf{v} \cdot \mathbf{v}\right) = \mathbf{v} \times \left(\nabla \times \mathbf{v}\right) + \left(\mathbf{v} \cdot \nabla\right)\mathbf{v} \tag{A.49}$$

the equation (A.48) becomes

$$\nabla \times \nabla \times \mathbf{E}' + \mathbf{E}' = -\frac{1}{2}\nabla \mathbf{v}^2 - \mathbf{v} \times \left(\mathbf{B}_0 + \mathbf{B}' - \nabla \times \mathbf{v} + \nabla \times \mathbf{A}_{ext}\right) - \nu\mathbf{v}. \tag{A.50}$$

Now let introduce new variable $\mathbf{E}''$ in such a way that

$$\mathbf{E}' = \mathbf{E}'' - \frac{1}{2}\nabla \mathbf{v}^2. \tag{A.51}$$

Using identity

$$\nabla \times \nabla \times \mathbf{E}' = \nabla \times \nabla \times \mathbf{E}'' \tag{A.52}$$

the system of equations (A.46), (A.47), (A.48) becomes

$$\begin{aligned} \frac{\partial \mathbf{v}}{\partial t} &= \nabla \times \nabla \times \mathbf{E}'' + \frac{\partial}{\partial t}\mathbf{A}_{ext}, & \text{(A.53)} \\ \nabla \times \mathbf{B}' &= -\mathbf{v} + \mathbf{A}_{ext}, & \text{(A.54)} \\ \nabla \times \nabla \times \mathbf{E}'' + \mathbf{E}'' &= -\mathbf{F} - \nu\mathbf{v}, & \text{(A.55)} \end{aligned}$$

where

$$\mathbf{F} = \mathbf{v} \times (\mathbf{B}_0 + \mathbf{B}' - \nabla \times \mathbf{v} + \nabla \times \mathbf{A}_{ext}) . \tag{A.56}$$

The advantage of the substitution (A.51) is that we are able to get rid of the $\nabla \mathbf{v}^2$ term which is very computationally intense if we want to use the Fourier space representation to solve the system. Now we do not need to resolve the equation for $\mathbf{E}'$ every time step, but only for the moments when we need actual electric field values.

In the Fourier domain the system (A.53), (A.54), (A.55) becomes

$$\begin{aligned} \frac{\partial \mathbf{v}^*}{\partial t} &= -\mathbf{k} \times \mathbf{k} \times \mathbf{E}^* + \frac{\partial}{\partial t}\mathbf{A}^*{}_{ext}, & \text{(A.57)} \\ \mathbf{B}^* &= \frac{i\mathbf{k} \times (-\mathbf{v}^* + \mathbf{A}^*_{ext})}{k^2}, & \text{(A.58)} \\ \mathbf{E}^* &= -\frac{\mathbf{F}^* + \nu\mathbf{v}^* + \mathbf{k}\,(\mathbf{k} \cdot \mathbf{F}^*)}{1 + k^2}, & \text{(A.59)} \end{aligned}$$

where we have used $\nabla \cdot \mathbf{B}' = 0$ and $\nabla \cdot \mathbf{v} = 0$. Substituting Eq. (A.59) to Eq. (A.57) we get

$$\frac{\partial \mathbf{v}^*}{\partial t} = \frac{-k^2\,(\mathbf{F}^* + \nu\mathbf{v}^*) + \mathbf{k}\,(\mathbf{k} \cdot \mathbf{F}^*)}{1 + k^2} + \frac{\partial}{\partial t}\mathbf{A}^*{}_{ext}. \tag{A.60}$$

Eqs. (A.60), (A.58), and (A.56) form a closed system of equations for $\mathbf{v}$, $\mathbf{B}$, and $\mathbf{F}$. The algorithm of integration of the system can be constructed in the following way. For given values of $\mathbf{F}^*$, $\mathbf{B}^*$ and $\mathbf{v}^*$ at $t = t_n$ using Eq. (A.60), we can perform one step integration in time to get $\mathbf{v}^*$ at instant $t = t_{n+1}$. This new value of $\mathbf{v}^*$ is used to obtain $\mathbf{B}^*$ and $\mathbf{F}^*$ at $t = t_{n+1}$, using Eqs. (A.58) and (A.56), respectively, and the process is repeated. Note that in order to compute F we need to converge $\mathbf{v} \times (...)$ term. To do that we have to Fourier transform three components of $\mathbf{v}^*$ and three components of the expression in brackets in Eq. (A.56) to the real space, take the cross product of them, and then Fourier transform the result back to k-space. Thus, each time step we have to perform six backward and three forward Fourier transforms.

A.4 Marching in time

In the Fourier domain the evolutionary equation (A.60) can be considered as a large system of ordinary differential equations (ODEs) which can be solved numerically using any stable and accurate method. Due to the nonlinearity of the equations the use of fully implicit schemes, such as backward Euler (BE) or Crank-Nicolson (CN) methods, is computationally inefficient, and standard explicit integrator techniques, such as Adams-Bashforth (AB) or Adams-Bashforth-Moulton (ABM) predictor-corrector schemes can be used [18]. For small enough time step AB and ABM methods are absolutely stable, while A-unstable [18], which leads to exponential grow of magnitudes at sufficiently large times.

The standard fourth-order Runge-Kutta (RK4) scheme was used in [24] for 3D simulations of sufficiently large magnitude nonlinear spheromaks. The leap-frog predictor [17, 18, 26] and trapezoidal corrector method was used in in [70, 71] for 2D simulations of nonlinear EMHD waves. An original predictor-corrector-corrector scheme of better stability properties was used in [55] for 2D simulations as well, which requires three evaluations of the right hand side per time step. The last scheme is a modified third-order Runge-Kutta (RK3) integrator, where the coefficients are selected in order to minimize the $O(h^4)$ term, which actually reduces the accuracy of the method to the second order.

Similar order of accuracy for the amplitudes can by achieved using the fourth-order AB (AB4) and the fourth-order ABM (ABM4) schemes, which require one and two right hand side evaluations each time step, respectively. In contrast to the scheme used in [55] AB4 and ABM4 provide the same order accuracy for both the amplitudes and the phases. Higher order technics, such as the six-order AB (AB6) and the six-order ABM (ABM6) have the same computational complexity as AB4 and ABM4, respectively, while require $\sim 50\%$ more memory to store the data from two additional time steps, and provide more accurate computation.

All of these schemes were implemented and found satisfactory, while the most accurate and stable computations were performed using additional iteration of the nonlinear term each time step. For such a scheme AB6 algorithm was used as a predictor, and then the Moulton correction was applied several times until the iteration error reaches some prescribed value. The number of such iterations is usually small (on average we had to perform not more than three iterations), while

this technic allows to integrate in time with relatively large time step (several times larger than the time step required by AB4 for the same accuracy). As a result of using this AB6 + iterative Moulton correction scheme the sufficient saving in computation time and increased stability of the scheme for substantially nonlinear cases were achieved.

A.5 Implementation. Numerical tests

The algorithm described above was implemented under MATLAB environment, which is quite efficient for the present problem as provides a good performance easy-to-use FFT library, while all the operations in the algorithm can be vectorized. The MATLAB environment also allows a user to map the algorithm on graphic processing unit (GPU) using AccelerEyes Jacket interface [3], which supports basic MATLAB operations and provide interface between MATLAB and CUFFT library [2]. In the present algorithm we used dealiasing based on the 2/3 rule [17, 18], which benefits also in terms of computational speed and used memory since it shrinks the size of state variables $(3/2)^3$ times. On top of it it is possible to use only half-size storage in the Fourier space due to real symmetry.

Numerical tests of the implemented algorithm were performed on a standard 3 GHz QuadCore PC equipped with 8 GB RAM and NVIDIA Tesla C1060 GPU with 4 GB video-memory operated under Windows XP64 varying grid size, input fields, antenna configuration, and time steps.

A.5.1 Linear waves induced by a loop antenna

In order to verify the fully nonlinear code in linear regime a set of computations were performed using fully nonlinear code with the magnetic field perturbations $\delta B \ll B_0$, which were compared to the analytical solution of linear problem Eq. (A.32). Fig. A.1(a), (b) illustrates distribution of the y-component of the wave magnetic field induced by a one loop antenna in the center plane ($y = 0$) at moment $t = 375$ as a function of x and z coordinates found using analytical solution of linear problem (Fig. A.1(a)) and by numerical integration of fully nonlinear equations (Fig. A.1(b)). The circular loop antenna of radius $a = 2.65$ was placed in the xz-plane and its center at the origin. The wave was exited by the current $I(t) = I_0 \cos \omega_{ext} t$ for $t > 0$, with $I_0 = 0.001$ and $\omega_{ext} = 0.04$. Computational domain of size $125 \times 125 \times 500$ was discretized by $256 \times 256 \times 512$ grid.

Figure A.1 shows that the numerical solution of the fully nonlinear equations obtained by numerical integration with time step $h = 1/4$ is close to the linear analytical solution. The relative magnitude of the nonlinear effects in this case can be estimated as $\sim 10^{-2}$ (in L^2-norm). The relative difference between the analytical and numerical solution is about 4×10^{-3} which is consistent with the order of the perturbation magnitude.

Further validation tests were performed for the same domain size varying the grid size. A convergence of the solution was observed for increasing number of the grid points. E.g., computational result on the grid $128 \times 128 \times 256$ for the case illustrated in Fig. A.1 had $\sim 10\%$ relative difference with respect to the reference

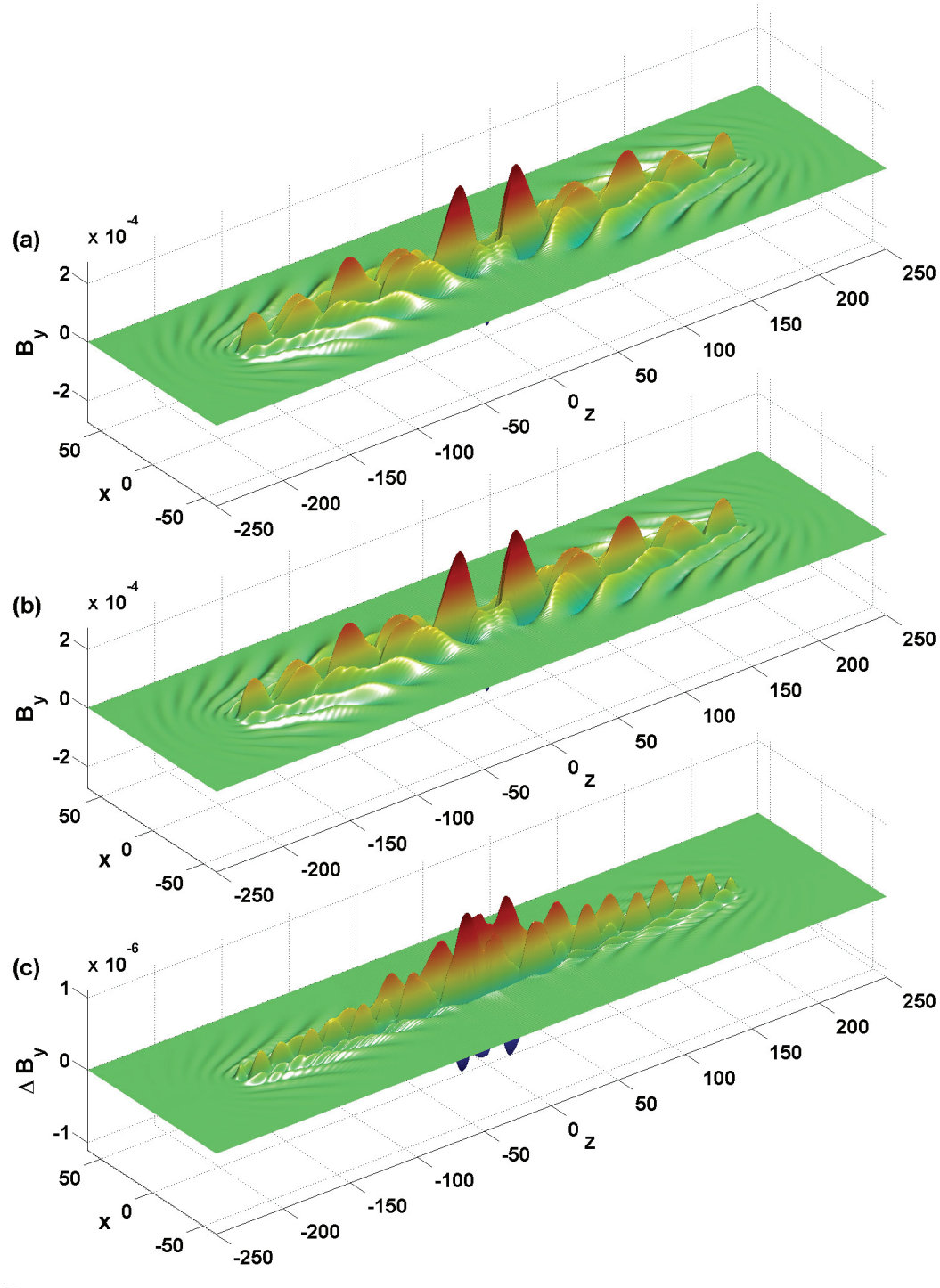

Figure A.1: Comparison of the analytical solution of the linear problem with the numerical solution of fully nonlinear problem for a wave induced by a one loop antenna driven by a small magnitude current $I_0 = 0.001$ ($B_y(x, y, z, t)$, $y = 0$, $t = 375$) driven with frequency $\omega_{ext} = 0.04$. Plot (c) shows the absolute difference between the analytical (a) and numerical (b) solutions.

solution on $256 \times 256 \times 512$ grid, while computations on $256 \times 256 \times 256$ grid had $\sim 1\%$ relative difference with respect to the reference solution on $256 \times 256 \times 512$ grid.

The tests with different time steps using AB4 scheme on the same grid were performed. In this case a numerical solution obtained on CPU with double precision and the time step $h = 1/32$ was used as a reference. A decrease of the time step from $h = 1/2$ to $h = 1/8$ both for the CPU and GPU (single precision) computations showed that the relative error reduces 16 times as h is halved (See Fig. A.2), which is consistent with the accuracy of the AB4 scheme. This trend continues for the double precision CPU computations with $h = 1/16$, but stops at this value for the GPU as the single precision limit is reached. Thus, a reduction of the time step for the GPU base code below $h = 1/16$ had almost no effect on relative error, which stabilized around 10^{-6}.

A.5.2 Nonlinear waves induced by a loop antenna

To study the effects of nonlinearity we performed several test runs for two-loop antennas with different magnitudes of the input currents. In these computations, the domain had sizes $67.6 \times 67.6 \times 270.3$, which was discretized by $150 \times 150 \times 600$ grid. The driving frequency was $\omega_{ext} = 0.1$ and the currents in the loops had the same magnitude of I_0 and were oscillating with $\pi/2$ relative phase difference. The diameter of the loops also was set $a = 2.65$.

Fig. A.3 illustrates the results for the magnetic field, $\mathbf{B}$. The plots in the left

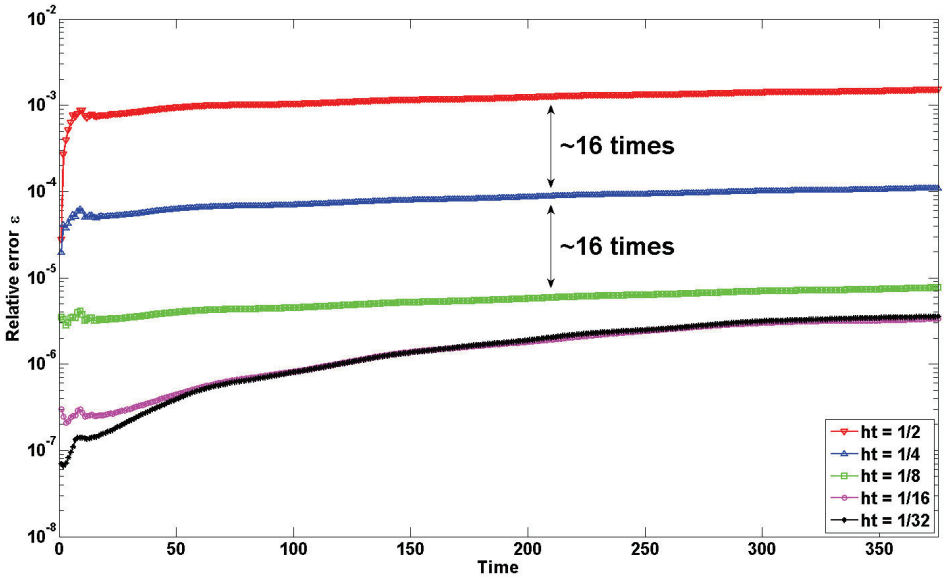

Figure A.2: Relative difference between numerical solutions with different time steps and reference numerical solution obtained on CPU with double precision and $h = 1/32$ as a function of time.

column show that at low input current magnitudes, the whistler waves have a regular structure. The increase of the amplitude leads to distortion of this structure, which at larger amplitudes looses its regularity and forms turbulent structures propagating from the source in the z directions. The panels in the right column show the z-slices of the magnetic field. The rotating structure of the field is clearly seen. It is also seen that large amplitude of the nonlinearity leads to a more complex structure.

We note that in all computations we varied the time step for integration to achieve stable reproducible results. While for the linear case the time integration step could be as large as h = 1/4 (or even larger), substantial reduction of the time step were needed to achieve stable computations for substantially nonlinear cases. The fact that the time step should be reduced at increasing non-linearity has an easy explanation. Indeed, the electron cyclotron frequency Ω_{ce} increases proportionally to the scale $\mathbf{B}$. If the scale is taken to be B_0 (ambient magnetic field), this is the true scale only for low amplitude perturbations. As the amplitude of the field increases, the effective cyclotron frequency increases as well. Since in our scaling we fixed Ω_{ce} to be determined by the background amplitude, we at least should decrease the time step inversely linearly with the amplitude of the field to provide the same stability conditions for larger amplitude perturbations as for the case of small amplitudes. For example, we found that computations for amplitude $I_0 = 5$ required integration time step $h = 1/32$ for stable computations for a given time interval $(0 < t < 500)$.

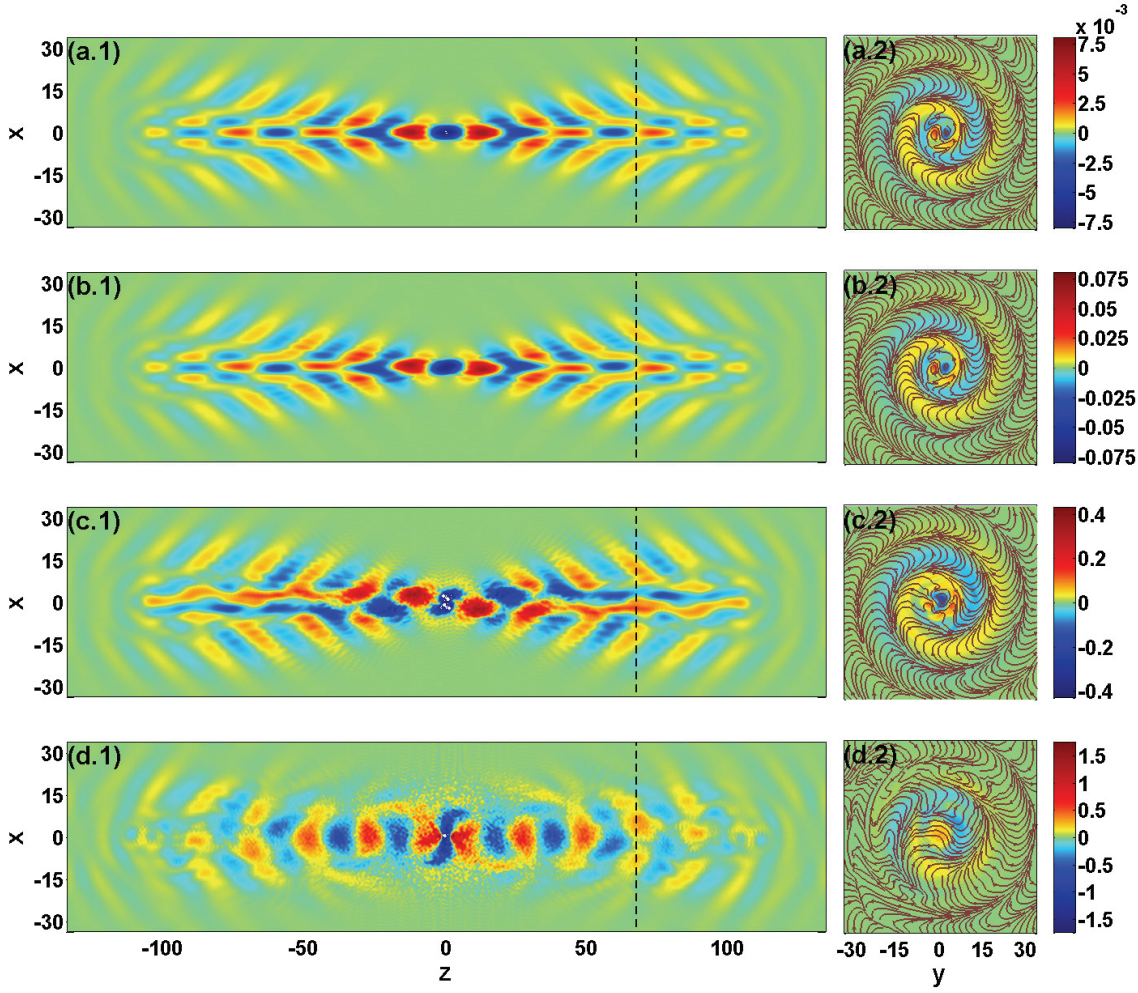

Figure A.3: The waves with different degree of nonlinearity generated by a two loop antenna with right handed polarization driven by currents with frequency $\omega_{ext} = 0.1$ and magnitudes $I_0 = 0.005$, 0.05, 0.5, and 5 (cases a,b,c and d, respectively). Plots (a.1) - (d.1) show y-component (perpendicular to the plane of figure) of magnetic field at $t = 220$. The stream lines on plots (a.2) - (d.2) show projection of the magnetic field perturbation on the plane perpendicular to z-axis, which location is shown by the dashed lines on plots (a.1)-(d.1).

A.5.3 Error test

In order to check the accuracy of the algorithm in nonlinear regime on the CPU (double precision) and GPU (single precision) the following tests were performed. In this tests numerical and analytical (exact) solutions for the fully nonlinear case were compared. To generate an exact of the fully nonlinear equation we used the following procedure.

Consider Eq. (A.60), which can be written as

$$\frac{\partial \mathbf{v}^*}{\partial t} = L\left(\mathbf{v}^*\right) + N\left(\mathbf{v}^*\right) - \mathbf{E}^*_{ext}\left(t\right), \tag{A.61}$$

where L and N are linear and nonlinear parts of the operator acting on the solution $\mathbf{v}^*$, and $\mathbf{E}^*_{ext}$ is know at any moment of time external electric field driving the wave. Assume we have a solution of linear equation $\mathbf{v}^*_{lin}\left(t\right)$, driven by the external field $\mathbf{E}^*_{ext}\left(t\right)$:

$$\frac{\partial \mathbf{v}^*_{lin}}{\partial t} = L\left(\mathbf{v}^*_{lin}\right) - \mathbf{E}^*_{ext}\left(t\right). \tag{A.62}$$

Now consider the nonlinear equation

$$\frac{\partial \mathbf{v}^*}{\partial t} = L\left(\mathbf{v}^*\right) + N\left(\mathbf{v}^*\right) - \mathbf{E}^*_{eff}\left(t\right), \tag{A.63}$$

with the effective driving field $\mathbf{E}^*_{eff}\left(t\right)$ given by

$$\mathbf{E}^*_{eff}\left(t\right) = \mathbf{E}^*_{ext}\left(t\right) + N\left(\mathbf{v}^*_{lin}\left(t\right)\right). \tag{A.64}$$

If we substitute Eq. (A.64) to Eq. (A.63) we get that the $\mathbf{v}^*_{lin}$ is a solution of the nonlinear equation. Since the linear solution can be found analytically, we can compute the operator $N\left(\mathbf{v}^*_{lin}\left(t\right)\right)$, that is the effective driving field $\mathbf{E}^*_{eff}\left(t\right)$, for any

given moment of time. Integrating numerically the nonlinear equation (A.63) with the same initial conditions as linear equation (A.62) ideally we should reproduce the linear solution.

Numerical error between the solution of fully nonlinear equation and the linear exact analytical solution in the real space can be computed as

$$\epsilon = \frac{\|\mathbf{v}_{nl} - \mathbf{v}_{lin}\|}{\|\mathbf{v}_{lin}\|}. \tag{A.65}$$

In the tests the L^∞ norm was used (relative maximum absolute error).

Fig. A.4 shows evolution of the errors for the test problem using GPU (single precision) and CPU(double precision) based computations. In all cases the reference solution was computed on CPU with double precision. The linear solution was generated as in the cases described above by a two loop antenna driven at frequency $\omega_{ext} = 0.05$ with $\pi/2$ relative phase difference. Computational domain of size $125 \times 125 \times 500$ was discretized by $64 \times 64 \times 256$ grid and the time step was $h = 1/32$ for all cases. We used the most accurate algorithm we have for these comparison (linearly stable scheme with ABM6 iterative integrator). It is seen that the error substantially depends on the amplitude of perturbations. Also while the error for low and moderate amplitude waves ($I_0 = 0.005$, $I_0 = 0.05$, $I_0 = 0.5$, and $I_0 = 0.5$) does not grow in time, a slight growth is observed for the large amplitude ($I_0 = 5$) case. The most striking, of course, is the difference between the CPU and GPU computations. For low amplitude waves these errors are consistent with single and double precision errors (note that there is no complete compliance of the GPU math functions with the IEEE standards for double precision), while they increase

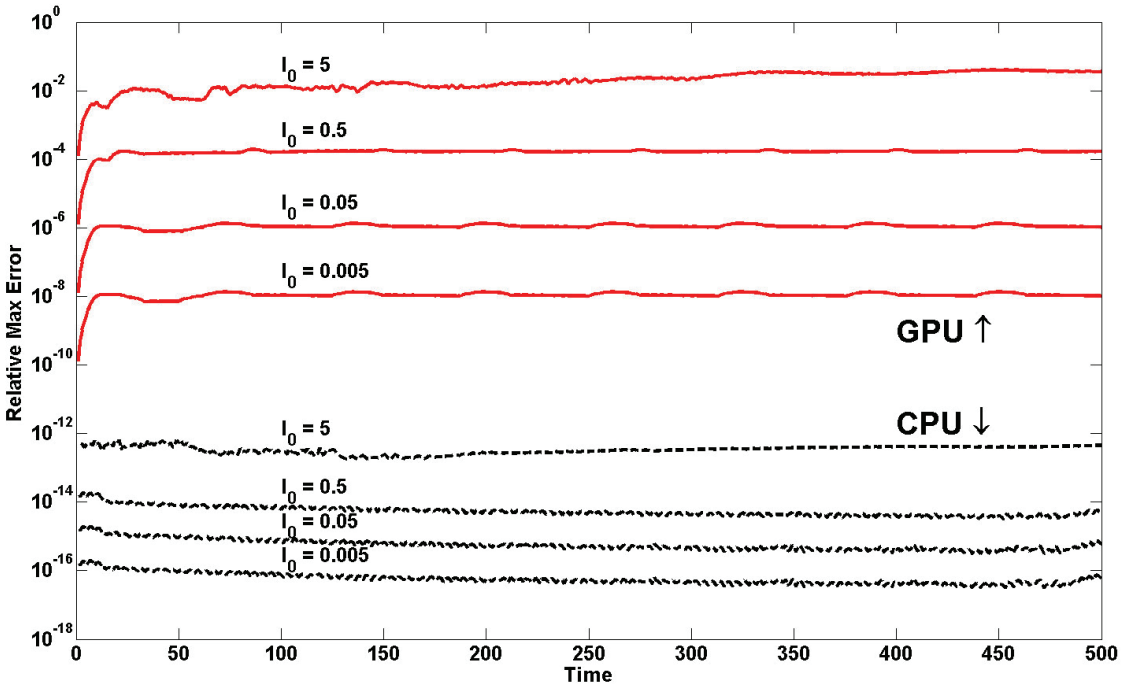

Figure A.4: Maximum relative errors as functions of time for computations on CPU with double precision and GPU with single precision for different, characterized by the input current I_0. In all cases the integrator time step was the same ($h = 1/32$). The iterative ABM6 scheme was used for the time propagation.

in orders of magnitude as the wave amplitude increases. It is also seen that at $t = 0$ the GPU errors are small they rapidly grow for a short time, and then stabilize. This is in contrast to the CPU computations, where the errors are almost constant in time. However, we can note that even for the worst case we have (GPU computations, $I_0 = 5$, $t = 500$), the maximum relative error achieved the value $\sim 3.6\%$. This level of the errors is acceptable for comparison with experiments and analysis of physical effects.

A.5.4 Performance

Since, the most computationally expensive part of the algorithm is related to the FFTs, the algorithm complexity scales as $O(N_t N \log N)$, where N_t is the number of time steps, and N is the size of the problem, which is the product of three dimensions of the grid, $N = N_x \times N_y \times N_z$. In terms of the use of different time integrators the constant of this asymptotic complexity is proportional to the number of evaluations of the right hand side of the system of ODEs to be solved. The Adams-Bashforth method in this sense is the fastest, as it requires only one evaluation per time step (ABM requires 2, RK4 requires 4, etc.). So to compare the performance of the same algorithm running on a CPU (serial code) and GPU it is sufficient to compare times per function call, or per time step for the Adams-Bashforth method.

Such a comparison is presented in Fig. A.5. We used grids which sizes are powers of two and dimensions which do not differ one form the other more than 2 times, starting with $32\times32\times32$ ($N = 2^{15}$) and ending with $256\times256\times512$ ($N = 2^{25}$), which is limited by the memory size of the hardware we used (in the latter case it was 2.46 GB of the GPU global memory; the problem scales nearly linearly in memory). One can see that even a serial code has a good enough performance as it computes one step on a grid of size of order $N \sim 10^6$ for time of the order of $1s$. However the use of the GPU reduces this time approximately 10 times. It is also seen that while the CPU time is scaled approximately linearly with N (theoretically $N \log N$), the efficiency of the use of the GPU increases with the problem size. For relatively

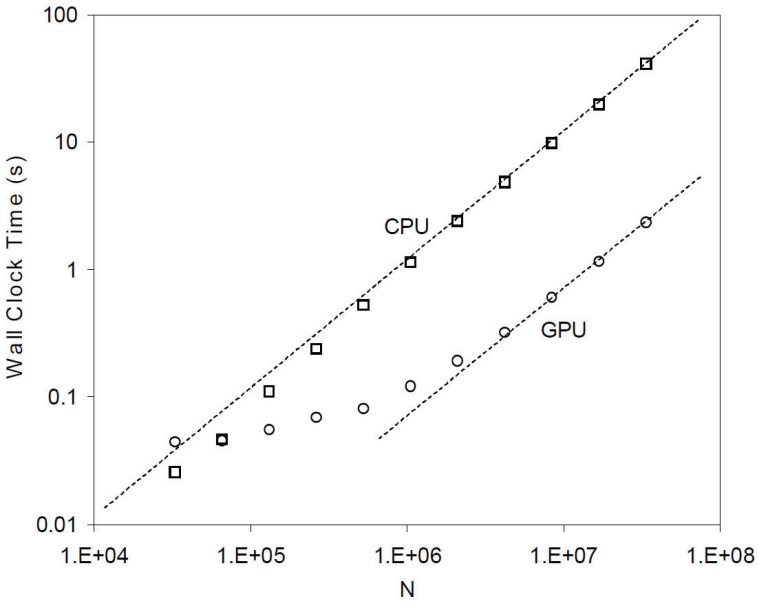

Figure A.5: Comparison of the CPU and GPU calculation wall clock times required to perform one time step using scheme with one right-hand side evaluation per time step (e.g., AB4) as a function of the problem size $N = N_x \times N_y \times N_z$ (N_x, N_y, and N_z are 3D grid dimensions).

small problems ($N \sim 10^5$) there are no advantage in the use of the GPU. Asymptotic saturation is reached for $N \sim 10^7$. So for such large N both implementations are scaled approximately linearly and the maximum ratio of the CPU and GPU times we observed is around 17.5.

Appendix B

Cold two-fluid MHD model

In the following section we describe a linear 3D spectral model which was used to simulate the propagation of shear Alfven waves generated by a RMF source. Following the EMHD approach [39, 53, 55, 79], which was implemented into linear [52] and nonlinear 3D EMHD spectral codes (See Appendix A), we start form the Maxwell equations with the displacement current neglected. In the EMHD model the ions treated as motionless. While this approximation works fairly well for the frequency range well above the lower-hybrid resonance, it becomes unacceptable for the frequencies bellow ion cyclotron frequency Ω_{ci}, when the motion of ions become important in the wave propagation [54, 93]. Thus, we can not consider the ions motionless and should solve an equation of motion for them.

On the other hand we would like the model to be able to produce valid results for broad frequency range including frequencies well above ion cyclotron frequency. In that case when the wave frequency approaches the electron cyclotron frequency Ω_{ce}, we can not consider electrons as massless, as it is often done in single fluid MHD models. In order to satisfy both of the requirements we should consider the plasma as a media consisting of two cold fluids (electrons and ions) and resolve equation of motion for both of them.

The equations governing a quasineutral cold two-fluid plasma can be written

as

$$\boldsymbol{\nabla} \times \mathbf{E} = -\frac{1}{c}\frac{\partial \mathbf{B}}{\partial t}, \tag{B.1a}$$

$$\boldsymbol{\nabla} \times \mathbf{B} = \frac{4\pi}{c}\mathbf{J} + \frac{4\pi}{c}\mathbf{J}_{ext}, \tag{B.1b}$$

$$\frac{\partial \mathbf{v}_e}{\partial t} + (\mathbf{v}_e \cdot \boldsymbol{\nabla})\,\mathbf{v}_e = -\frac{e}{m_e}\left(\mathbf{E} + \frac{1}{c}\mathbf{v}_e \times \mathbf{B}\right) - \nu_{en}\mathbf{v}_e - \nu_{ei}\left(\mathbf{v}_e - \mathbf{v}_i\right), \tag{B.1c}$$

$$\frac{\partial \mathbf{v}_i}{\partial t} + (\mathbf{v}_i \cdot \boldsymbol{\nabla})\,\mathbf{v}_i = \frac{e}{m_i}\left(\mathbf{E} + \frac{1}{c}\mathbf{v}_i \times \mathbf{B}\right) - \nu_{in}\mathbf{v}_i - \nu_{ie}\left(\mathbf{v}_i - \mathbf{v}_e\right), \tag{B.1d}$$

where indexes e and i denote electrons and ions, $\mathbf{J}$ is a plasma current, $\mathbf{J}_{ext}$ is an external current source, and ν_{en}, ν_{in}, ν_{ei}, and ν_{ie} are effective frequencies of collisions of electrons and ions with neutrals and Coulomb collisions. The last terms in Eqs. (B.1c) and (B.1d) correspond to momentum exchange between the electron and ion fluids due to Coulomb collisions. The conservation of the total momentum of two-fluid system requires that

$$\nu_{ie} = \frac{m_e}{m_i}\nu_{ei}. \tag{B.2}$$

Let decompose the total magnetic field as $\mathbf{B} = \mathbf{B}_0 + \mathbf{B}'$, where $\mathbf{B}_0$ is stationary uniform ambient magnetic field, and $\mathbf{B}'$ is the wave perturbation. The scales of the Eqs. (B.1) are determined by two frequencies: electron plasma ω_{pe} and electron cyclotron Ω_{ce} frequencies. Normalizing length by the electron skin-depth $\lambda_e = c/\omega_{pe}$ and time by the inverse of electron cyclotron frequency $T = \Omega_{ce}^{-1}$, the dimensionless variable become $\overline{t} = t/T$, $\overline{\mathbf{x}} = \mathbf{x}/\lambda_e$, $\overline{\mathbf{v}} = T\mathbf{v}/\lambda_e$, $\overline{\mathbf{B}} = \mathbf{B}/B_0$, $\overline{\mathbf{E}} = (cT\mathbf{E})/(\lambda_e B_0)$ and $\overline{\nu} = \nu/\Omega_{ce}$.

Consider the case of small amplitude wave ($|\mathbf{B}'| \ll |\mathbf{B}_0|$). In that limit lin-

earized Eqs. (B.1) can be written in dimensionless form as

$$\overline{\boldsymbol{\nabla}} \times \overline{\mathbf{E}} = -\frac{\partial \overline{\mathbf{B}}}{\partial \overline{t}}, \tag{B.3a}$$

$$\overline{\boldsymbol{\nabla}} \times \overline{\mathbf{B}} = \overline{\mathbf{v}}_i - \overline{\mathbf{v}}_e + 4\pi \overline{\mathbf{J}}_{ext}, \tag{B.3b}$$

$$\frac{\partial \overline{\mathbf{v}}_e}{\partial \overline{t}} = -\left(\overline{\mathbf{E}} + \overline{\mathbf{v}}_e \times \mathbf{b}\right) - \overline{\nu}_{en}\overline{\mathbf{v}}_e - \overline{\nu}_{ei}\left(\overline{\mathbf{v}}_e - \overline{\mathbf{v}}_i\right), \tag{B.3c}$$

$$\frac{\partial \overline{\mathbf{v}}_i}{\partial \overline{t}} = m_r\left(\overline{\mathbf{E}} + \overline{\mathbf{v}}_i \times \mathbf{b}\right) - \overline{\nu}_{in}\overline{\mathbf{v}}_i - m_r\overline{\nu}_{ei}\left(\overline{\mathbf{v}}_i - \overline{\mathbf{v}}_e\right), \tag{B.3d}$$

where we neglected all nonlinear terms. m_r is the ratio between electron and ion masses ($m_r = m_e/m_i$), $\overline{\mathbf{B}}$ is dimensionless perturbed magnetic field and $\mathbf{b}$ is the unit vector in the direction of the ambient magnetic field $\mathbf{B}_0$, chosen to be along z-axis ($\mathbf{b} = \mathbf{e}_z$). We used also for the plasma current $\mathbf{J} = en\left(\mathbf{v}_i - \mathbf{v}_i\right)$, where for quasineutral plasma $n = n_e = n_i$. From this point to the end only dimensionless variables are used, so let drop the bars in the remaining section.

The external current $\mathbf{J}_{ext}$ entering Eq. (B.3b), which is used to drive the RMF wave, can be introduced in the model as loops of an antenna. In the case of interest the size of the antenna is much smaller than the computational domain. That means that if we want to resolve the boundary problem on the current elements we have to use either nonuniform or very fine mesh with a large number of grid points. In the case of infinitely thin wires the current and the fields become singular. In order to avoid singularity in solution and remove the necessity to resolve boundary problem on the current elements we decompose the electric and magnetic field as $\mathbf{E} = \mathbf{E}' + \mathbf{E}_{ext}$ and $\mathbf{B} = \mathbf{B}' + \mathbf{B}_{ext}$, where

$$\mathbf{E}_{ext} = -\frac{\partial}{\partial t}\mathbf{A}_{ext}, \quad \mathbf{B}_{ext} = \boldsymbol{\nabla} \times \mathbf{A}_{ext}. \tag{B.4}$$

Such decomposition can be chosen more or less arbitrary with the only requirement that the fields $\mathbf{E}_{ext}$ and $\mathbf{B}_{ext}$ have the same singularity at the vicinity of the external current as the total fields. One of the possible choices for the external vector potential $\mathbf{A}_{ext}$ is the screened potential satisfying the equation

$$\boldsymbol{\nabla} \times \boldsymbol{\nabla} \times \mathbf{A}_{ext} + (1 + m_r)\, \mathbf{A}_{ext} = 4\pi \mathbf{J}_{ext}. \tag{B.5}$$

The principle of superposition is applicable to the vector potential $\mathbf{A}_{ext}$, and it can be calculated for each current independently. If the current elements does not move in space and the time dependence appears only as $f(t)$ factor in $\mathbf{J}\,(\mathbf{x}, t)$, the vector potential $\mathbf{A}_{ext}$ should be calculated only ones at the very first time step. The ways of solving of Eq. (B.5) for particular current configurations are described in Appendix C and Ref. [52].

Let introduce new variables:

$$\mathbf{V} = m_r \mathbf{v}_e + \mathbf{v}_i, \quad \mathbf{j} = \mathbf{v}_i - \mathbf{v}_e. \tag{B.6}$$

which are the mass velocity of the two-component fluid up to the coefficient $(1 + m_r)$ and the total current.

In these variables using Eqs. (B.4),(B.5) the system of Eqs. (B.3) can be rewritten as

$$\boldsymbol{\nabla} \times \boldsymbol{\nabla} \times \mathbf{E}' = -\frac{\partial \mathbf{j}}{\partial t} - \frac{\partial}{\partial t}\mathbf{A}_{ext}, \tag{B.7a}$$

$$\frac{\partial \mathbf{V}}{\partial t} = m_r \mathbf{j} \times \mathbf{e}_z + \alpha \mathbf{V} + \beta \mathbf{j}, \tag{B.7b}$$

$$\frac{\partial \mathbf{j}}{\partial t} = (1 + m_r)\, \mathbf{E}' + (\mathbf{V} - (1 - m_r)\, \mathbf{j}) \times \mathbf{e}_z + \gamma \mathbf{V} + \delta \mathbf{j} - (1 + m_r)\, \frac{\partial}{\partial t}\mathbf{A}_{ext}, \tag{B.7c}$$

where

$$\alpha = -\frac{\nu_{in} + m_r \nu_{en}}{1 + m_r}, \tag{B.8a}$$

$$\beta = m_r \gamma, \tag{B.8b}$$

$$\gamma = \frac{\nu_{en} - \nu_{in}}{1 + m_r}, \tag{B.8c}$$

$$\delta = -\frac{(1 + m_r)^2 \nu_{ei} + \nu_{en} + m_r \nu_{in}}{1 + m_r}. \tag{B.8d}$$

All of these coefficients are just real number parameters depending on the effective collision frequencies and the electron/ion mass ratio.

Taking the divergence of Eq. (B.7c) we find

$$\boldsymbol{\nabla} \cdot \mathbf{E}' = -\frac{\boldsymbol{\nabla} \cdot \left((\mathbf{V} - (1 - m_r)\, \mathbf{j}) \times \mathbf{e}_z + \gamma \mathbf{V} \right)}{1 + m_r}, \tag{B.9}$$

where we used the fact that if the external current is divergence-free ($\boldsymbol{\nabla} \cdot \mathbf{J}_{ext} = 0$) Eq. (B.5) implies that $\boldsymbol{\nabla} \cdot \mathbf{A}_{ext} = 0$, and Eq. (B.3b) implies that $\boldsymbol{\nabla} \cdot \mathbf{j} = 0$.

From Eqs. (B.7) using Eq. (B.9) we find

$$\begin{aligned} \left(1 + m_r - \nabla^2\right) \mathbf{E}' \;\; = \;\; & \boldsymbol{\nabla} \frac{\boldsymbol{\nabla} \cdot \left((\mathbf{V} - (1 - m_r)\, \mathbf{j}) \times \mathbf{e}_z + \gamma \mathbf{V} \right)}{1 + m_r} - \\ & - (\mathbf{V} - (1 - m_r)\, \mathbf{j}) \times \mathbf{e}_z, -\gamma \mathbf{V} - \delta \mathbf{j} \end{aligned} \tag{B.10}$$

which can be easily resolved with respect to $\mathbf{E}'$ in the Fourier domain

$$\begin{aligned} \mathbf{E}^* \;\; = \;\; & -\mathbf{k} \frac{\mathbf{k} \cdot \left((\mathbf{V}^* - (1 - m_r)\, \mathbf{j}^*) \times \mathbf{e}_z + \gamma \mathbf{V}^* \right)}{(1 + m_r)\left(1 + m_r + k^2\right)} - \\ & - \frac{(\mathbf{V}^* - (1 - m_r)\, \mathbf{j}^*) \times \mathbf{e}_z}{1 + m_r + k^2} - \frac{\gamma \mathbf{V}^* + \delta \mathbf{j}^*}{1 + m_r + k^2}, \end{aligned} \tag{B.11}$$

where asterisks denote the Fourier components.

Excluding $\mathbf{E}'$ from Eq. (B.7c) we can write the closed system for $\mathbf{j}^*$ and $\mathbf{V}^*$ in the Fourier domain

$$\frac{\partial \mathbf{j}^*}{\partial t} = -\mathbf{k}\frac{\mathbf{k}\cdot\left(\left(\mathbf{V}^* - (1-m_r)\,\mathbf{j}^*\right)\times\mathbf{e}_z + \gamma\mathbf{V}^*\right)}{1+m_r+k^2} + \tag{B.12a}$$
$$+\frac{k^2\left(\mathbf{V}^* - (1-m_r)\,\mathbf{j}^*\right)\times\mathbf{e}_z}{1+m_r+k^2} + \frac{k^2\left(\gamma\mathbf{V}^* + \delta\mathbf{j}^*\right)}{1+m_r+k^2} - (1+m_r)\,\frac{\partial}{\partial t}\mathbf{A}^*_{ext},$$

$$\frac{\partial \mathbf{V}^*}{\partial t} = m_r\mathbf{j}^*\times\mathbf{e}_z + \alpha\mathbf{V}^* + m_r\gamma\mathbf{j}^*. \tag{B.12b}$$

The Eqs. (B.12) form the closed system of six equations for j_x^*, j_y^*, j_z^*, V_x^*, V_y^*, and V_z^* for every possible wave vector $\mathbf{k}$. One of the equations can be excluded noting that $\boldsymbol{\nabla}\cdot\mathbf{j} = 0$ or $\mathbf{k}\cdot\mathbf{j}^* = 0$. Thus, for every $\mathbf{k}$ we need to solve the system of five time evolution equations.

In principle, an analytical solution of system (B.12) can be written right away using LU-decomposition as it was done for EMHD model [52] and in Appendix A, and the system reduces to eigen values and eigen vectors problem of 5×5 matrix for every $\mathbf{k}$, but we would like to slightly modify Eqs. (B.12) before solving it.

Consider an arbitrary vector field $\mathbf{F}$ and its Fourier components $\mathbf{F}^*$. For any vector $\mathbf{F}$

$$\mathbf{k}\cdot\left(\mathbf{F}^*\times\mathbf{e}_z\right) = -i\left(\boldsymbol{\nabla}\times\mathbf{F}\right)^*_{||} = -iF^*_{c||}, \tag{B.13}$$

where $F^*_{c||}$ is the Fourier component of the projection of $\boldsymbol{\nabla}\times\mathbf{F}$ on z-axis, that is parallel to the ambient magnetic field.

$$k_z F_z^* = -i\left(\boldsymbol{\nabla}\cdot\mathbf{F}_{||}\right)^* = -iF^*_{d||}, \tag{B.14}$$

where $F^*_{d||}$ is the Fourier component of the divergence of the vector $\mathbf{F}$ component

parallel to the ambient magnetic field.

$$\mathbf{k}\cdot\mathbf{F}^{*}-k_{z}F_{z}^{*}=-i\left(\boldsymbol{\nabla}\cdot\mathbf{F}_{\perp}\right)^{*}=-iF_{d\perp}^{*}, \tag{B.15}$$

where $F_{d\perp}^{*}$ is the Fourier component of the divergence of the vector $\mathbf{F}$ component perpendicular to the ambient magnetic field.

Using definitions (B.13), (B.14), and (B.15) Eqs. (B.12) become

$$\frac{\partial}{\partial t}X=LX+S, \tag{B.16}$$

where

$$X=\begin{bmatrix} j_{c||}^{*} \\ j_{d||}^{*} \\ V_{c||}^{*} \\ V_{d\perp}^{*} \\ C^{*} \end{bmatrix}, \quad S=-\left(1+m_{r}\right)\frac{\partial}{\partial t}\begin{bmatrix} A_{c||}^{*} \\ A_{d||}^{*} \\ 0 \\ 0 \\ 0 \end{bmatrix} \tag{B.17}$$

and the system matrix

$$L=\begin{pmatrix} K\delta & -K\left(1-m_{r}\right) & K\gamma & -K & 0 \\ K_{z}\left(1-m_{r}\right) & K\delta & \frac{\gamma^{2}(K-2K_{z})-K_{z}}{1+\gamma^{2}} & -\gamma\frac{\gamma^{2}K+K_{z}}{1+\gamma^{2}} & \frac{\gamma^{3}(K-K_{z})}{1+\gamma^{2}} \\ m_{r}\gamma & m_{r} & \alpha & 0 & 0 \\ m_{r} & -m_{r}\gamma & 0 & \alpha & 0 \\ 0 & 0 & 0 & 0 & \alpha \end{pmatrix}, \tag{B.18}$$

where

$$C^{*}=V_{d\perp}^{*}-\frac{1}{\gamma}V_{c||}^{*}+\left(1+\frac{1}{\gamma^{2}}\right)V_{d||}^{*}. \tag{B.19}$$

and

$$K = \frac{k^2}{1 + m_r + k^2}, \quad K_z = \frac{k_z^2}{1 + m_r + k^2}. \tag{B.20}$$

Solution of Eq. (B.16) can be written as

$$\begin{aligned} X(\mathbf{k}, t) &= U(\mathbf{k}) e^{\Lambda(\mathbf{k})t} U^{-1}(\mathbf{k}) X(\mathbf{k}, 0) + \\ &+ U(\mathbf{k}) e^{\Lambda(\mathbf{k})t} \int_0^t e^{-\Lambda(\mathbf{k})t'} U^{-1}(\mathbf{k}) S(\mathbf{k}, t')\, dt', \end{aligned} \tag{B.21}$$

where $\Lambda(\mathbf{k})$ and $U(\mathbf{k})$ are diagonal matrix of eigenvalues and modal matrix that consists of columns of corresponding eigenvectors, which decompose the system matrix Eq. (B.18) as

$$L = U \Lambda U^{-1} \tag{B.22}$$

and do not depend on time. Thus, for a given geometry they can be computed for every $\mathbf{k}$ only once. Particularly, in the case of harmonically driven field and zero initial velocities of electron and ion fluids we get

$$S(\mathbf{k}, t) = S(\mathbf{k}) e^{-i\omega t}, \qquad X(\mathbf{k}, 0) = 0 \tag{B.23}$$

and the solution (B.21) become

$$X(\mathbf{k}, t) = U(\mathbf{k}) M(\mathbf{k}, t) U^{-1}(\mathbf{k}) S(\mathbf{k}), \tag{B.24}$$

where

$$M(\mathbf{k}, t) = \left(e^{\Lambda(\mathbf{k})t} - I e^{-i\omega t}\right) \left(\Lambda(\mathbf{k}) + i\omega I\right)^{-1}, \tag{B.25}$$

where I is identity matrix.

Thus, the problem reduces to finding eigen values and eigen vectors of the system matrix (B.18) for every possible $\mathbf{k}$. To find the eigenvalues of $L(\mathbf{k})$ we need

to solve characteristic equation which can be written in the form

$$(\alpha-\lambda)\begin{vmatrix} K\delta-\lambda & -K(1-m_r) & K\gamma & -K \\ K_z(1-m_r) & K\delta-\lambda & \frac{\gamma^2(K-2K_z)-K_z}{1+\gamma^2} & -\gamma\frac{\gamma^2K+K_z}{1+\gamma^2} \\ m_r\gamma & m_r & \alpha-\lambda & 0 \\ m_r & -m_r\gamma & 0 & \alpha-\lambda \end{vmatrix}=0. \quad \text{(B.26)}$$

If we replace λ by $-i\omega$ we will get the dispersion relation for the two-fluid system. The first term of the Eq. (B.26) does not depend on $\mathbf{k}$ and describes the mode which is determined by electron-neutral and ion-neutral collision rates. The variable C^* (Eq. (B.19)) depends only on the components of the mass velocity, and this mode is essentially a friction between the two-fluid system and neutral gas background. In the case of zero initial mass velocity this mode is not excited, and the variable C^* becomes an integral of motion and stays zero all the time.

The 4×4 determinant in Eq. (B.26) gives in general case forth order equation for λ. All the coefficients of the equation are real. It means that the forth order equation has two pairs of complex conjugate roots. The real parts of the roots correspond to spatial decay rates, and the imaginary parts determine the wave propagation in $\pm$ directions with respect to the background magnetic field.

In the collisionless case ($\nu_{ei}=\nu_{en}=\nu_{in}=0$) the 4×4 determinant in Eq. (B.26) simplifies to the dispersion relation

$$\omega^4-\left(m_r(K+K_z)+(1-m_r)^2KK_z\right)\omega^2+m_r^2KK_z=0. \quad \text{(B.27)}$$

Introducing θ be the angle between the direction of the wave vector $\mathbf{k}$ and the

ambient magnetic field ($k_z = k\cos\theta$), we get from Eq. (B.27)

$$Ak^4 + Bk^2 + C = 0, \tag{B.28}$$

where

$$A = \omega^4 + \cos^2\theta\left(m_r^2 - (1-m_r)^2\omega^2\right) - m_r\omega^2\left(1 + cos^2\theta\right), \tag{B.29}$$

$$B = \omega^2(1+m_r)\left(2\omega^2 - m_r\left(1 + cos^2\theta\right)\right), \tag{B.30}$$

$$C = \omega^4(1+m_r). \tag{B.31}$$

Note that the parameter $m_r < 10^{-4} \ll 1$ for, let say, He plasma, but during the derivation of the equations we did not neglected m_r compare to 1, so results are valid even for electron-positron plasma ($m_r = 1$). We kept finite masses for both electrons and ions, which benefits in the ability of the model give valid results in the broad frequency range in different regimes: the Alfven waves (below ion cyclotron frequency) and the whistler waves (well above lower-hybrid resonance). As a matter of fact the EMHD model [39, 52, 53, 55, 79] is built in the two fluid model as the limit $m_r \to 0$. In Fig. B.1 B_x component (perpendicular to the plane of the picture) of the perturbed magnetic field for different regimes calculated using described two fluid MHD 3D model is presented in collisionless case. In Fig. B.1(a) the wave generated with the driving frequency $\omega = 0.5\Omega_{ci}$ is presented. Note that in the Fig. B.1(a) the scale along z-axis is 10 times larger than along y-direction. One can see that the wave generated is very well confined by the ambient magnetic field and the magnitude does not decay along z-axis, which are the properties of the Alfven waves in collisionless plasmas. Unlike the Alfen wave regime the wave generated

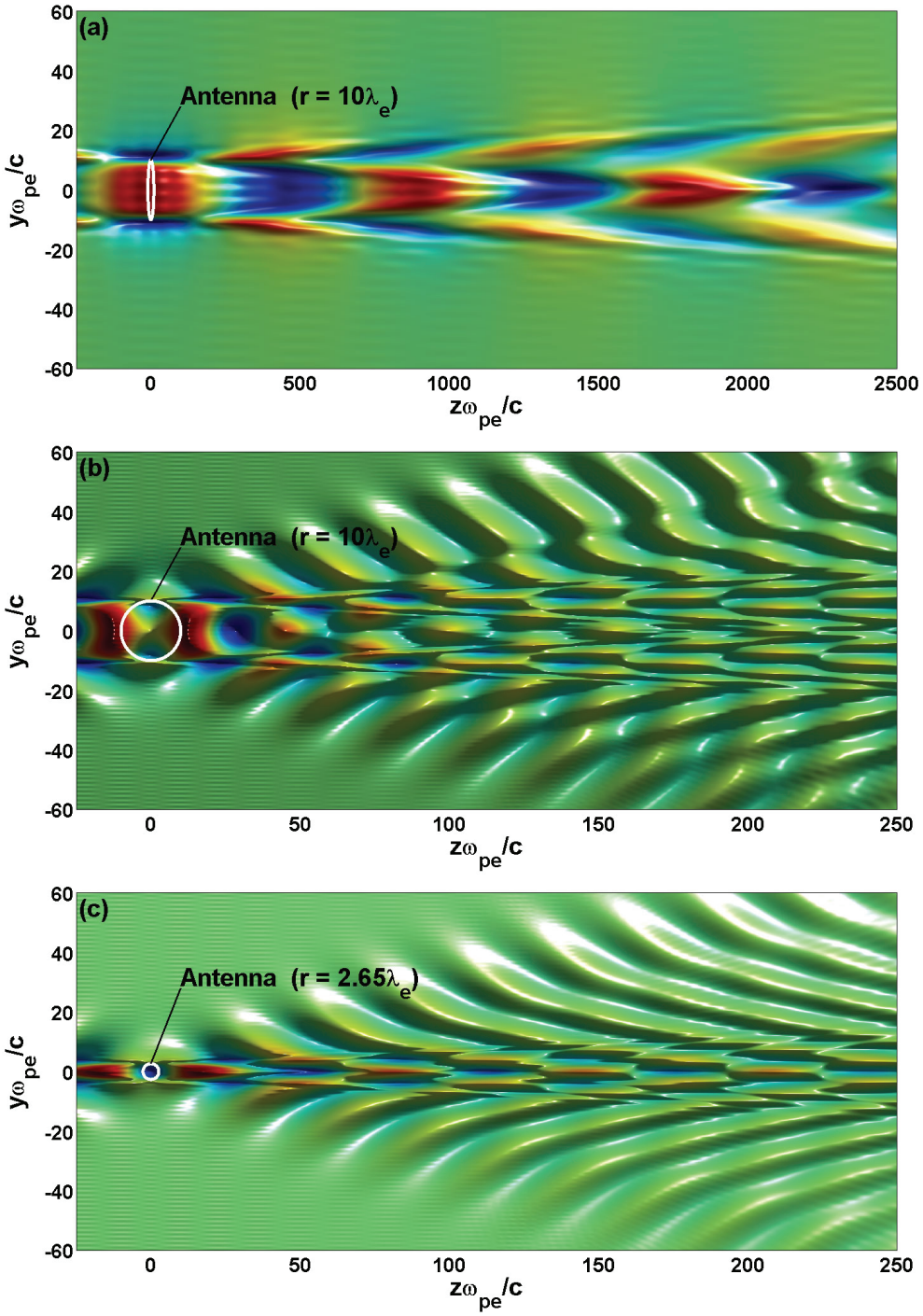

Figure B.1: B_x component (perpendicular to the plane of the picture) of perturbed magnetic filed in the plane containing the loop with current (ring at the origin) in different wave regimes calculated using two fluid MHD 3D model in collisionless case: (a) - Alfven wave ($\omega = 0.5\Omega_{ci}$, antenna radius $r = 10\lambda_e$), (b) - whistler wave ($\omega = 0.05\Omega_{ce}$, antenna radius $r = 10\lambda_e$), (c) - whistler wave ($\omega = 0.05\Omega_{ce}$, antenna radius $r = 2.65\lambda_e$). Note that the scale in (a) is 10 times bigger along z-axis.

with frequency $\omega = 0.05\Omega_{ce}$ (See Fig. B.1(b)) has cone structure and decay of the magnitude along z-axis due to spreading of the wave energy inside the propagation cone, which is characteristic of whistler waves. Fig. B.1 features B_x component of perturbed magnetic field of the wave with frequency $\omega = 0.05\Omega_{ce}$ and the antenna radius $r = 2.65\lambda_e$. These parameters were used in [52] (See Section IV) and featured on Fig. 2.19 for calculations using EMHD model. The relative difference between the results produced by two fluid MHD and single electron fluid EMHD models has order of 10^{-4} for these parameters, which is the order of m_r.

Appendix C

Solution of equation for eternal vector potential

C.1 Equation for external vector potential

In order to avoid singularity in solution and remove necessity to resolve boundary problem on current elements the electric end magnetic field were decomposed as Eq. (A.11). Such decomposition can be chosen more or less arbitrarily with the only one requirement that $\mathbf{E}_{ext}$ and $\mathbf{B}_{ext}$ have the same singularity at the external current elements as the total fields. One of the possible choices for the external vector potential is the screened potential satisfying the Helmholtz equation

$$\nabla \times \nabla \times \mathbf{A}_{ext} + \mathbf{A}_{ext} = 4\pi \mathbf{j}_{ext}. \tag{C.1}$$

Consider the case of the radiating antenna, which consists of one or several closed current loops. Since the case of more than one loop can be easily treated by superposition of single loop vector potentials, it is sufficient to consider the case of a single current loop C. In this case the solution for Eq. (C.1) for current $I(t)$ flowing in the loop C can be written in the integral form as

$$\mathbf{A}_{ext}(\mathbf{r}, t) = -4\pi I(t) \int_C G(\mathbf{r}, \mathbf{r}') \, d\mathbf{l}(\mathbf{r}'), \tag{C.2}$$

where $\mathbf{l}(\mathbf{r}')$ is the contour element along loop C, and $G(\mathbf{r}, \mathbf{r}')$ is the Green's function, satisfying equation

$$\nabla^2_{\mathbf{r}} G(\mathbf{r}, \mathbf{r}') - G(\mathbf{r}, \mathbf{r}') = -\delta(\mathbf{r} - \mathbf{r}'). \tag{C.3}$$

and

$$G\left(\mathbf{r},\mathbf{r}'\right)=\frac{\exp\left(-\left|\mathbf{r}-\mathbf{r}'\right|\right)}{\left|\mathbf{r}-\mathbf{r}'\right|}. \tag{C.4}$$

In general case the contour integral Eq. (C.1) should be found numerically and stored for further use in computations for every loop. Note that when using spectral methods the external vector potential Eq. (C.1) can be computed directly in the Fourier space, which can simplify the computations or even provide an analytical expression in some cases (See Appendix C.2). Since the Fourier component of the Green's function

$$G^{*}\left(\mathbf{k},\mathbf{r}'\right)=\frac{\exp\left(-i\mathbf{k}\cdot\mathbf{r}'\right)}{k^{2}+1}, \tag{C.5}$$

the Fourier component of the vector potential can be written as

$$\mathbf{A}_{ext}^{*}\left(\mathbf{k},t\right)=\int_{\mathbb{R}^{3}}\mathbf{A}_{ext}e^{-i\mathbf{k}\cdot\mathbf{r}}d\mathbf{r}=-\frac{4\pi}{k^{2}+1}I\left(t\right)\int_{C}\mathbf{l}\left(\mathbf{r}'\right)e^{-i\mathbf{k}\cdot\mathbf{r}'}dl\left(\mathbf{r}'\right). \tag{C.6}$$

C.2 An analytical expression for vector potential of a singe circular current loop

Consider a single circular current loop of radius a centered at the origin of the reference frame and with the normal pointing along the z-direction (See Fig. C.1). For such loop in the cylindrical coordinates we have

$$\mathbf{l}\left(\mathbf{r}'\right) = \mathbf{e}'_{\varphi}, \tag{C.7}$$

$$dl = ad\varphi', \tag{C.8}$$

$$\mathbf{e}'_{\varphi} = -\mathbf{e}_{x}\sin\varphi'+\mathbf{e}_{y}\cos\varphi', \tag{C.9}$$

$$\mathbf{e}'_{\rho} = \mathbf{e}_{x}\cos\varphi'+\mathbf{e}_{y}\sin\varphi', \tag{C.10}$$

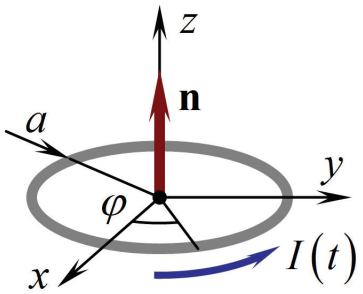

Figure C.1: Coordinate system for a single circular current loop.

where $\mathbf{e}_x$, $\mathbf{e}_y$, $\mathbf{e}_\varphi$, and $\mathbf{e}_\rho$ are unit vectors along the corresponding directions.

Eq. (C.6) yields for the current $I(t)$ flowing in that loop

$$\begin{aligned} \mathbf{A}^*_{ext} &= -\frac{4\pi a I(t)}{k^2+1}\int_0^{2\pi} \mathbf{e}'_\varphi e^{-i\mathbf{k}\cdot\mathbf{r}'} d\varphi' = \\ &= \mathbf{e}_x \frac{4\pi a I(t)}{k^2+1}\int_0^{2\pi} \sin\varphi' e^{-i\mathbf{k}\cdot\mathbf{r}'} d\varphi' - \mathbf{e}_y \frac{4\pi a I(t)}{k^2+1}\int_0^{2\pi} \cos\varphi' e^{-i\mathbf{k}\cdot\mathbf{r}'} d\varphi'. \end{aligned} \tag{C.11}$$

For components of the wave vector $\mathbf{k}$ we have

$$k_x = k_\rho \cos\varphi_k, \tag{C.12}$$

$$k_y = k_\rho \sin\varphi_k, \tag{C.13}$$

$$k_\rho = \sqrt{k_x^2 + k_y^2}. \tag{C.14}$$

That yields

$$e^{-i\mathbf{k}\cdot\mathbf{r}'} = e^{-iak_\rho\cos(\varphi_k-\varphi')}. \tag{C.15}$$

Substituting Eq. (C.15) into Eq. (C.11) we get the following expressions for the

vector potential in cylindrical coordinates

$$A^*_{ext,\rho} = A^*_{ext,x}\cos\varphi_k + A^*_{ext,y}\sin\varphi_k = \tag{C.16}$$
$$= \frac{4\pi a I(t)}{k^2+1}\int_{\varphi_k}^{2\pi-\varphi_k}\sin\varphi'' e^{-iak_\rho\cos\varphi''}d\varphi'' = 0,$$
$$A^*_{ext,\varphi} = -A^*_{ext,x}\sin\varphi_k + A^*_{ext,y}\cos\varphi_k = \tag{C.17}$$
$$= -\frac{4\pi a I(t)}{k^2+1}\int_{\varphi_k}^{2\pi-\varphi_k}\cos\varphi'' e^{-iak_\rho\cos\varphi''}d\varphi'' = \frac{i8\pi^2 a I(t)}{k^2+1}J_1(k_\rho a),$$
$$A^*_{ext,z} = 0, \tag{C.18}$$

where J_1 is the first-order Bessel function of the first kind. The components of the single loop vector potential in the cartesian coordinates are

$$A^*_{ext,x}(\mathbf{k},t) = -I(t)\frac{i8\pi^2 a k_y}{k_\rho(k^2+1)}J_1(k_\rho a), \tag{C.19}$$
$$A^*_{ext,y}(\mathbf{k},t) = I(t)\frac{i8\pi^2 a k_x}{k_\rho(k^2+1)}J_1(k_\rho a), \tag{C.20}$$
$$A^*_{ext,y}(\mathbf{k},t) = 0. \tag{C.21}$$

Note also that these expressions are not singular at $k_\rho = 0$ (along the z-axis). Since $J_1(k_\rho a) = \frac{1}{2}k_\rho a + O\left((k_\rho a)^3\right)$ for $k_\rho \to 0$, the asymptotic behavior of the components at the vicinity of the z-axis is

$$A^*_{ext,x}(\mathbf{k},t) \sim -I(t)\frac{i4\pi^2 a^2 k_y}{k^2+1}\left(1+O\left((k_\rho a)^2\right)\right), \tag{C.22}$$
$$A^*_{ext,y}(\mathbf{k},t) \sim I(t)\frac{i4\pi^2 a^2 k_x}{k^2+1}\left(1+O\left((k_\rho a)^2\right)\right). \tag{C.23}$$

Appendix D

Van Allen Radiation Belts

D.1 Mechanism of trapping of charged particles by a magnetic field

It is well known that charged particles can be trapped by a spatially variable stationary magnetic field due to the conservation of the first adiabatic invariant [62, 63, 82]

$$\mu = \frac{v_\perp^2}{B}, \tag{D.1}$$

where $v_\perp$ is the component of the particle velocity perpendicular to the magnetic field line and B is the value of the magnetic field at the location of the particle. Typical trajectories of trapped charged particles in the Earth's dipole magnetic field are shown in Fig. D.1. The trajectories shown in Fig. D.1 were found by numerical integration of the relativistic equations of motion for charged particles in a dipole magnetic field. The energy of the protons used in the simulations was 30 MeV, which is a typical energy of the trapped protons in the inner radiation belt. The energy of the electrons used in the simulations was 200 MeV which is much higher than the typical energy values. This was chosen for the simulation in order to make the gyration radius higher, otherwise for the typical energy of several MeV it would be too small to see it on the scale of Fig. D.1.

The trajectory of a charged particle in the dipole magnetic field consists three types of motion. The first of them is gyration around the magnetic field line on a

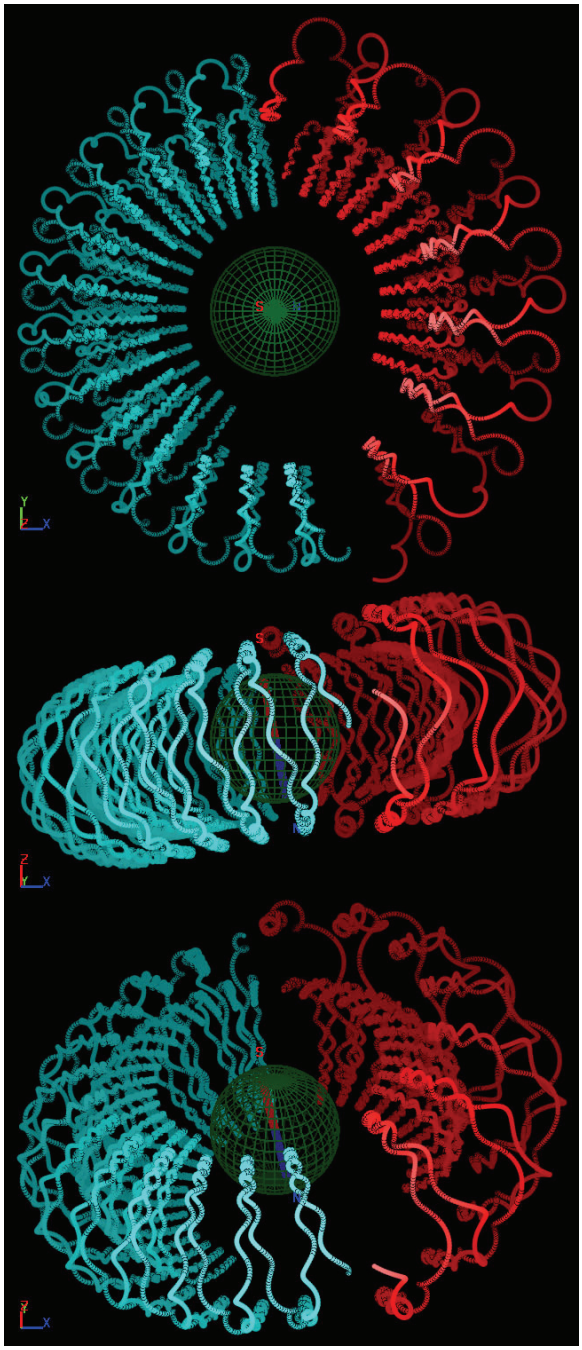

Figure D.1: Typical trajectories of trapped charged particles in the Earth's dipole magnetic field (red - 30 MeV protons, blue - 200 MeV electrons). A charged particle on its trajectory is involved in three different motions: gyration around magnetic field line, bouncing motion between mirror points and the drift around the planet due to curvature of the magnetic field lines. Protons drift westward and electrons drift eastward. The direction of the drift is determined by the sign of particle charge.

circular orbit with so called Larmor radius

$$r_g = \frac{p_\perp}{|q|B}, \tag{D.2}$$

where $p_\perp$ is the relativistic momentum of the particle in the direction perpendicular to the magnetic field line and q is its charge. This gyration motion has frequency

$$\Omega_c = \frac{|q|B}{\gamma m} \tag{D.3}$$

known as the cyclotron frequency. Here m is the rest mass of the particle and $\gamma = \sqrt{1 - v^2/c^2}$ is the relativistic Lorentz gamma factor. For typical values of Earth's magnetic field ($\sim \mu T$) the cyclotron frequencies for protons are on the order of tens to several hundreds of Hertz, and the cyclotron frequencies for electrons are in the range $10^5 - 10^6\ Hz$.

Because of the presence of a non-zero component of the velocity parallel to the magnetic field $v_{||}$, the motion becomes a spiral around the magnetic filed line. The Earth magnetic field lines are banded and their density is higher closer to the surface of the planet. When a particle spiraling around the magnetic field line gets closer to the polar regions it experiences a stronger magnetic field. Because of conservation of the first adiabatic invariant, Eq. (D.1), it increases the component of the velocity perpendicular to the magnetic field and the portion of kinetic energy corresponding to the perpendicular motion. The Lorentz force due to a magnetic field is always normal to the velocity of the particle and does not change its total kinetic energy. This means that in order to keep the particle energy constant the portion corresponding to the motion parallel to the magnetic field decreases. At some point the perpendicular portion of the kinetic energy becomes equal to the

total energy and parallel portion becomes zero. The particle switches the sign of its parallel velocity, gets reflected and travels back along the field line. The point when parallel component of the velocity becomes zero is called mirror point. The particles trapped by Earth magnetic field bounce back and forth between mirror points in northern and southern hemispheres.

The location of the mirror point for a given particle energy is determined by the field line and the relation of the parallel component of the particle velocity to the perpendicular component at the magnetic equatorial plane. This relation is usually expressed using the so called pitch angle. The pitch angle is the angle between the magnetic field line and velocity of the particle (See Fig. D.2). Strictly speaking, the value of the pitch angle of the particle is changing during the motion of the particle along the field line. That is why the equatorial pitch angle - the angle between the velocity of the particle and the magnetic field line when the particle crosses magnetic equatorial plane - is used for characterization of the motion of the particles. For a given particle kinetic energy the equatorial pitch angle determines the ratio between the parallel and perpendicular components of the kinetic energy. The closer the pitch angle is to 90 degrees the higher the perpendicular component of the kinetic energy is. That means that the parallel component of the kinetic energy is smaller and can faster get to zero value which corresponds to the mirror point. For equatorial pitch angles equal to 90 degrees the particles gyrate in the magnetic equatorial plane. Particles with lower pitch angels have higher parallel component of the kinetic energy, can travel farther away from the magnetic equator, and mirror at a lower altitude. For pitch angles below a threshold value the particles can get

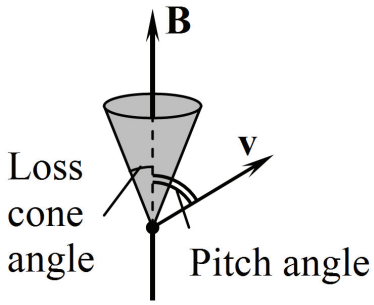

Figure D.2: Particle pitch angle and loss cone.

to altitudes where the ambient gas density is high enough to precipitate them. The maximum value of the equatorial pitch angle required for particle precipitation is called the loss cone angle. Virtually all the particles with a pitch angle inside the loss cone precipitate in the atmosphere, while in the absence of collisions particles with pitch angle values higher than the loss cone angle can remain trapped. The Coulomb collisions start to play an important role in the scattering and loss of electrons with energies greater than 100 keV only at L shells lower than 1.25 [4,90]. The electrons trapped in the radiation belts are so energetic that they make a several thousand kilometers trip between two mirror points at the northern and southern hemispheres at the time in around 0.1 s.

The third kind of motion is the drift around the planet which is determined by the curvature of the magnetic field lines westward for ions and eastward for electrons. A typical electron circles the Earth in tens of minutes. The drift motion for all ions and electrons has a particular direction, determined by the sign of the particle charge. Since the directions of electron and ion drifts are opposite, this results in a current around the planet known as the ring current. Typical parameters of trapped

charged particles are shown in Table D.1.

Table D.1: Characteristics of typical charged particles trapped by the Earth's magnetic field. (Adopted form [1])

	Electron $E = 1\ MeV$	Proton $E = 10\ MeV$
Peak equatorial omnidirectional flux ($cm^{-2}s^{-1}$)	4×10^6	3.4×10^5
Radial location (L) of peak flux (Earth radii)	4.4	1.7
Gyroradius (km)		
At altitude 500 km	0.6	50
At altitude $20,000\ km$	10	880
Gyration period (s)		
At altitude 500 km	10^{-5}	7×10^{-3}
At altitude $20,000\ km$	2×10^{-4}	0.13
Bounce period (s)		
At altitude 500 km	0.1	0.65
At altitude $20,000\ km$	0.3	1.7
Longitudinal drift period (min)		
At altitude 500 km	10	3
At altitude $20,000\ km$	2.5	1.1

D.2 Van Allen Radiation Belts

The Van Allen radiation belts belts are two concentric donut-shaped regions around Earth with omnidirectional fluxes of highly energetic charged particles with a slot region of relatively low flux in between them (See Fig. D.3). The inner radiation belt starts essentially from the upper ionosphere and extends up to ~ 2 Earth radii. It consists of a high concentration of energetic protons with energies up to several

hundreds of MeV and electrons with typical energies of a hundred keV up to a few MeV [1]. The source of the protons with energies higher than 50 MeV is the beta decay of neutrons created by cosmic ray interactions with nuclei in the upper atmosphere. The lower energy protons are in the radiation belts due to a diffusion inwards in a changing magnetic field during geomagnetic storms [80].

The inner radiation belt is a very stable formation with natural characteristic relaxation times of years, which has nearly steady location and flux values. Fig. D.4 shows time variation of the omnidirectional fluxes of protons with $E > 80$ MeV and electrons with the energies $E > 300$ keV over a 25 years period. Both the inner proton and electron radiation belts are nearly steady in location with a very pronounced outer border, except for the extreme event of the anomalous sudden commencement on March 24, 1991 when during a strong geomagnetic storm the outer border of the inner radiation belt was significantly moved outward. It took nearly three years for it to get back [9, 15, 57, 74, 84, 95]. The outer radiation belt is much more dynamically active. It changes its location, width, and in many events moves inwards to the surface and fill the slot region between $L \approx 2$ and $L \approx 3$.

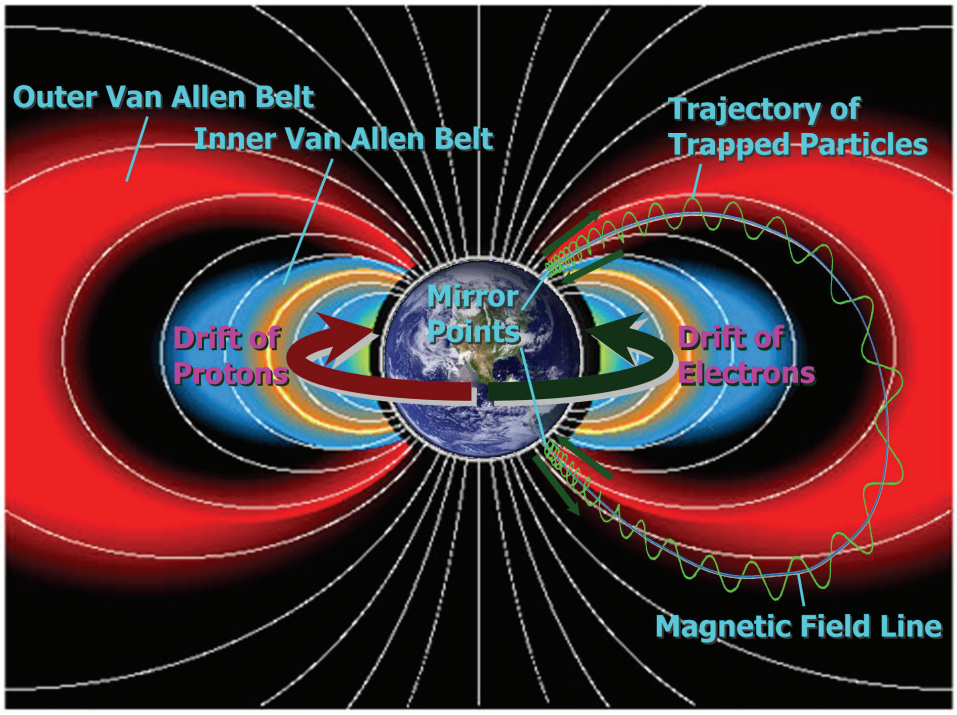

Figure D.3: Schematic picture of lower layers of Earth magnetosphere. Van Allen radiation belts and a typical trajectory of a trapped charged particle are shown.

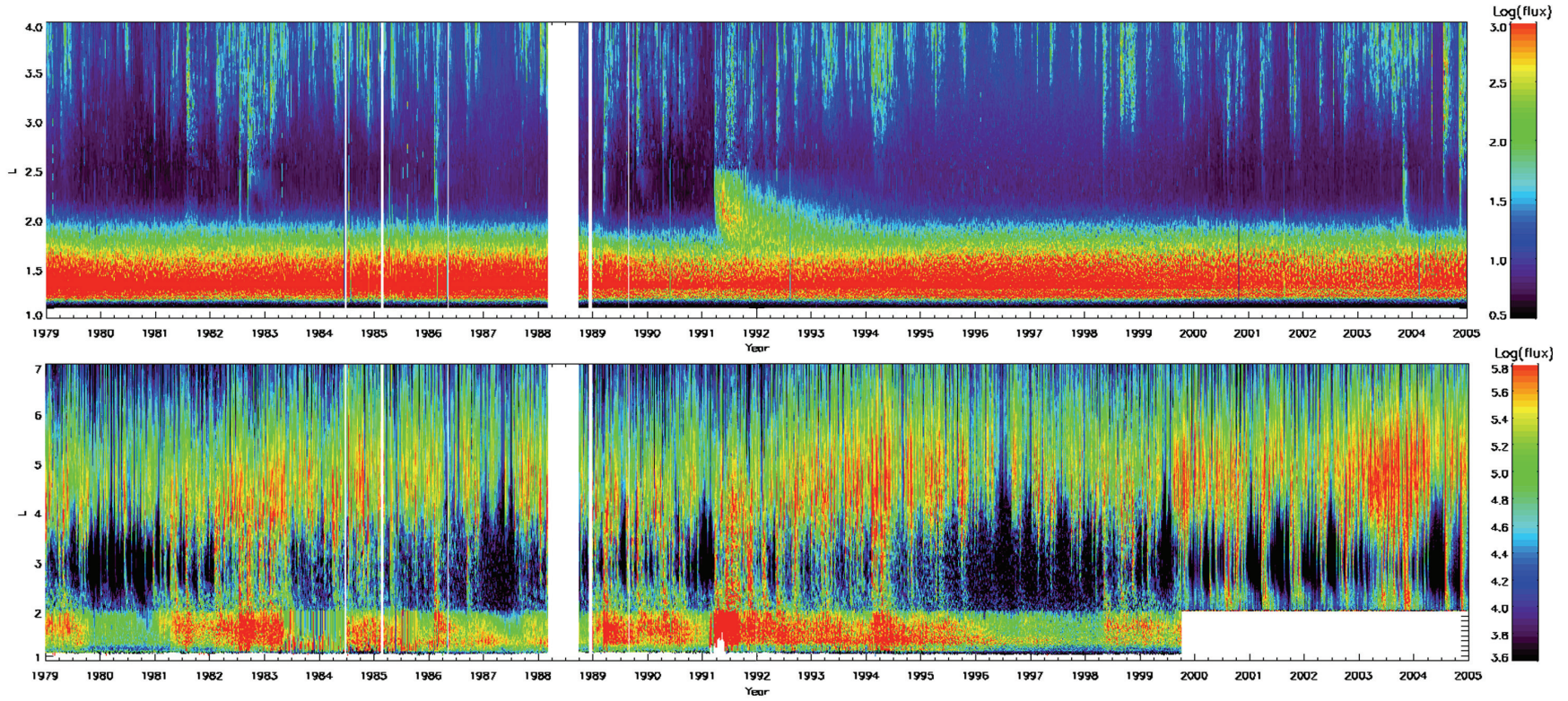

Figure D.4: Time variation of omnidirectional fluxes of protons with the energy $E > 80\ MeV$ (top graph) and electrons with the energy $E > 300\ keV$ (bottom graph) in the radiation belts during 25 years period (1979 - 2005). Sharp move of the outer border of the proton inner radiation belt (top graph) corresponds to the great geomagnetic storm of March 24, 1991. In the electron flux (bottom graph) one can see the inner belt with the peak flux at $L \approx 1.6$ and sharp nearly steady outer border at $L \approx 2$, the slot region from $L \approx 2$ to $L \approx 3$, and much more dynamically active outer belt with peak flux at $L \approx 4 - 5$. Data from NOAA 5-15 POES Satellites. Launched in 1999 NOAA-15 POES satellite changed telescope pointing direction, so there is no data available for electrons at $L < 2$. (Credit: Xi Shao, University of Maryland)

The outer radiation belt starts at approximately three and extends up to ten Earth radii. The outer radiation belt consists mostly of highly energetic electrons with energies of $0.1-10\ MeV$. The peak of the flux intensity is usually around $4-5$ Earth radii. The source of the energetic electrons is mostly inward diffusion and local acceleration due to wave-particle interaction of the electrons with the whistler mode waves [45]. Unlike the inner radiation belt the outer radiation belt is more dynamically active. Its location and fluxes are highly influenced by the intensity of incoming solar wind. It can be compressed inwards by a storm to fill the slot region and expand outwards during quiet time.

D.3 The effect of radiation belts on satellites

A vast number of satellites are currently orbiting around the Earth, with trajectories passing through the radiation belts. The radiation belt energetic electron and proton fluxes are a major cause of performance anomalies and operational lifetime limitations for Low Earth Orbiting (LEO) satellites. This is accentuated by the presence of the South Atlantic Anomaly (SAA), a region where because of the low magnetic field the protons can get closer to the surface of the planet, and the high energy proton flux is reaching altitudes as low as 200 km.

The highly energetic charged particles of the radiation belts can damage or even destroy the microprocessor control systems, sensors, and solar cells of orbiting satellites. An electron with the energy of order MeV can fly through the bulk of a microchip causing strong ionization on its way before loosing all of its kinetic

energy, and leading to possible malfunctioning of the chip. This issue is becoming increasingly important because current development of microchips uses sub-micron feature technologies, which is on the order of the characteristic cross-section of the damage caused by an energetic electron. That means that an electron can destroy one of the millions of transistors of a microchip making it worthless. For example, the intolerable rate of Single Event Upsets (SEU) of the IBM 603 microprocessors (based on $\sim 0.5\ \mu m$ CMOS technology) used in Iridium communication satellites forced Motorola to disable the microprocessor cache while passing the SAA.

While currently most of the operational problems are centered in the vicinity of SAA, this is not the case of the for future LEO satellites. High volume production and the associated cost savings forced satellite systems to utilize Commercial-Of-The-Shelf (COTS) electronics. The anomalies caused by an impact of energetic charged particles are known as Single Event Effects (SEE). The SEE anomaly cross section is a strongly non-linear function of the device feature size. Current estimates [20] indicate that the SEE cross section, that is the probability of the damage, increases by a factor of over one hundred if the satellite systems move from micron feature scale to the currently available COTS of $65\ nm$. This implies that in the near future the LEO orbit range for satellites using COTS electronics will be operationally unavailable.

Although the slot region between inner and outer radiation belts with ~ 4 orders of magnitude lower flux values is relatively safe for spacecrafts, orbits are usually chosen in order to maximize mission efficiency, but not to minimize the radiation damage. In addition, strong solar storms can perturb the outer radiation

belt and change its size and location and push the outer belt into the slot region.

The protection of a spacecraft from the harmful particle radiation is one of the most important design problems. In principle, it is possible to protect valuable parts, electronics and instruments which could be damaged by the radiation belt particles by a metallic shielding. For example, the depth of penetration of a 1 MeV electron into aluminum is around 2 mm. This means that two mm shielding of a spacecraft by aluminum will protect the spacecraft from electrons with energies less than 1 MeV. But that shield will not help against higher energy electrons which will only slow down and penetrate the shield. Besides, each kilogram of extra weight of shielding will cost tens of thousands of dollars for a mission, or if the weight is kept constant, extra shielding means less instrumental loads for the spacecraft. Furthermore not all parts of a spacecraft, like solar panels, sensors, radiating and receiving antennas, are possible to shield.

D.4 Radiation belt remediation by VLF transmissions

Magnetospheric physics suggests potential ways for man to have an influence on the populations of energetic charged particles in the Earth's magnetosphere. Recent analysis of data collected by the DEMETER satellite provided evidence that very-low frequency (VLF) transmissions by a US Navy station in Exmouth, Australia, used for communications with submarines in submerged position, cause precipitation of high-energy electrons form the inner radiation belt [69]. The results of the research suggest the possibility of controlled radiation belt remediation (RBR).

The evidence of the electron radiation belt remediation by the ground-based VLF transmissions has been accumulating for quite a while. A. Vampola and G. Kuck [83] reported about OV1-14 and OV1-19 satellites observations during 1968-1970 period of the electron remediation caused by transmissions of Russian VLF station UMS, operating at the frequency of 16.2 kHz. Similar results but caused by different VLF transmitters (the U. S. Navy VLF transmitters at Cutler, Maine (NAA) and at Annapolis, Maryland (NSS)) were reported in Refs. [47–49, 67] in 1983. Although these results were strong and compelling, they were patchy.

So, what makes the DEMETER satellite special? In the payload of the DEMETER satellite is a charged particle counter called IDP. The combination of the spectral resolution, collection area and viewing angle of the instrument provides a nearly ideal tool for electron density measurements in the inner radiation belt. Because of its circular polar orbit, as DEMETER makes its way around the Earth it crosses all the field lines, from the low magnetic latitude short loops to unclosed magnetic pole field lines. The IDP instrument and the proper orbit have provided the possibility to make charts of electron fluxes of various energies at an altitude of 715 km above the Earth's surface.

On the charts of energetic electron fluxes Sauvaud *et al.* [69] found a long, thin feature trailing eastward from the vicinity of Exmouth, Australia, of the enhanced electron flux at low 715 km altitude. Exmouth is the site of the US Navy VLF Communication Station Harold E. Holt. The VLF transmitter of 1 MW of power (the most powerful VLF transmitter in the Southern hemisphere) has 300 m high antennas and operates at the frequency of 19.8 kHz. The long, thin stripe in the electron

flux indicates that trapped electrons were able to reach the low DEMETER orbit, because the pitch angle was drawn to smaller values. A similar feature appears in the Northern hemisphere and trails eastward from the Exmouth magnetic conjugate point. It appears 95% of nighttime transmissions, when the ionospheric wave guide is the leakiest, and some of the wave energy can penetrate the ionosphere and get to the inner radiation belt region. During daytime transmissions, the conjugate point feature is not seen, because too little of the VLF wave energy can get through the ionosphere to have a detectable effect.

The VLF radiation is the most efficient for the resonant pitch angle scattering of the electrons into the loss cone when the direction of the propagation is along the magnetic field [4], which is not the case for the Exmouth station. When the VLF radiation emitted form the Exmouth transmitter travels upward and penetrates the ionosphere, it meets the magnetic field lines inclined by $\sim 35^o$ to the vertical. But because of the existence of the tubes of enhanced cold plasma density called whistler wave ducts, the VLF radiation can be guided within these ducts. If the transmitter was located at the higher magnetic latitude the effect of scattering would be bigger.

After discovering the effect that the Exmouth transmitter had on electron pitch angle, Sauvaud and coauthors [69] looked for a similar effect caused by another powerful VLF transmitter, located in Hawaii, but they did not see any detectable effects. This is because too little of the VLF wave energy leaks through the equatorial ionosphere, and the penetrated wave reaches the outer ionosphere where the magnetic field lines are nearly perpendicular to the wave propagation direction, and the whistler wave ducts are to weak.

Efficient ground-based VLF transmissions require very long antennas. At best, only fractions of a percent of the energy radiated from the ground-based VLF transmitter can penetrate the ionosphere and reach the inner radiation belt during night time, and even smaller during day time. Thus, a lower power satellite-based VLF transmitter can be more efficient for radiation belt remediation than the most powerful ground-based station.

Controlled, enhanced precipitation of relativistic electrons in the radiation belts by injecting whistler waves from space platforms is an active research topic and is related to enhanced precipitation of relativistic electrons injected by a beta-decay of radioactive products of a deliberate or an accidental high altitude nuclear explosion [23, 65, 66, 75]. Such an explosion can increase the relativistic electron flux in the radiation belt by more than four orders of magnitude with natural decay rate of several years. This would have catastrophic consequences to LEO satellites within a period of one week.

The RBR aims at injecting sufficient VLF power in the radiation belts to reduce the relativistic electron lifetime to less than a few days. In Ref. [27] authors have discussed the possibility of VLF wave injection by taking advantage of the free energy available by the release of few tons of Barium from a rocket launcher at $\sim 500\ km$ altitude. Such a release could create whistler waves with extremely high amplitude capable of achieving electron lifetime of less than an hour. In Ref. [4] author studied the loss rates of MeV radiation belt electrons on L-shells from $L \approx 2$ to $L \approx 4$ due to Coulomb collisions with thermal background plasma as well as resonant wave-particle interaction with plasmaspheric hiss, lightning-generated

whistlers and VLF transmitter radiation. They found that the signals from VLF transmitters, operating at frequencies of $17 - 23\ kHz$ at the locations around the world, constitute the principle loss mechanism and dominantly affect the electron lifetimes over the range $1.3 \leqslant L \leqslant 2.6$. In Ref. [50] Inan et al. further suggested controlling precipitation of radiation belt electrons by injection of whistler mode waves from a constellation of space-based transmitters. In Ref. [73] Shao *et al.* evaluated the possibility of controlling of inner radiation belt proton population by injection of Alfvén waves. The proton radiation belt remediation (PRBR) involves slow and controlled action with time scales of years while electron RBR requires fast action on the order of hours to days.

The precipitation of electrons by the VLF transmissions [47–49, 67, 69, 83] is due to resonant wave-particle interaction, when electrons satisfy the resonant condition [4, 89]

$$\omega - k_{||} v_{||} = -\frac{n\Omega_{ce}}{\gamma}, \tag{D.4}$$

where ω is the wave frequency, $k_{||}$ is the wave number component along the magnetic filed line, $v_{||}$ is the particle velocity component parallel to the magnetic field, Ω_{ce} is the electron cyclotron frequency, γ is the relativistic Lorentz factor, and n is an integer harmonic resonance number. The resonant condition is very restrictive in terms of the position and electron velocity components. Because the magnetic field value varies along the same field line, the region where the resonant condition Eq. (D.4) is satisfied is very localized. Besides that, in the resonant condition the particle velocity enters only through its parallel component. This means that for

the fixed electron energy only the particles with particular pitch angles will be in resonance with the field.

On the other hand the electrons can be precipitated via a non-resonant scattering by creating a non-local magnetic field gradient, which leads to the breaking of the adiabatic invariant Eq. (D.1). Such a non-local magnetic field gradient will affect virtually all the particles independent of their energy and pitch-angle. Whistler and MHD waves created by a rotating magnetic field RMF source are candidates for creating such non-local magnetic field gradients.

Bibliography

[1] *ECSS Space engineering: Space enviroment*. ECSS-E-ST-10-04C, 15 November 2008.

[2] CUDA CUFFT Library. http://developer.download.nvidia.com/compute/cuda/1_1/CUFFT_Library_1.1.pdf, Oct. 2007.

[3] Jacket User Guide. The GPU Engine for MATLAB. http://www.accelereyes.com/content/doc/JacketUserGuide.pdf, Jan 2010.

[4] R. Abel and R. M. Thorne. Electron scattering loss in Earth's inner magnetosphere. *J. of Geophys. Res.*, 103(A2):2385–2407, 1998.

[5] O. Alexandrova, A. Mangeney, M. Maksimovic, C. Lacombe, N. Cornilleau-Wehrlin, E. A. Lucek, P. M. E. Decreau, J.-M. Bosqued, P. Travnicek, and A. N. Fazakerley. Cluster observations of finite amplitude Alfvén waves and small-scale magnetic filaments downstream of a quasi-perpendicular shock. *J. Geophys. Res.*, 109:A05207, 2004.

[6] Hannes Alfvén. Existence of electromagnetichydrodynamic waves. *Nature*, 150:405, 1942.

[7] Hannes Alfvén. On the existence of electromagnetichydrodynamic waves. *Arkiv for Matematik Astromoni och Fysik*, 29B(2):1, 1942.

[8] J. M. Anderson and L. Goldstein. Interaction of electromagnetic waves of radio-frequency in isothermal plasmas: Collision cross section of helium atoms and ions for electrons. *Phys. Rev.*, 100(4):1037–1047, 1955.

[9] T. Araki, S. Fujitani, M. Emoto, K. Yumoto, K. Shiokawa, T. Ichinose, H. Luehr, D. Orr, D. K. Milling, H. Singer, G. Rostoker, S. Tsunomura, Y. Yamada, and C. F. Liu. Anomalous sudden commencement on March 24, 1991. *J. Geophys. Res.*, 102(A7):14075–14086, 1997.

[10] P. Baille, J.-S. Chang, A. Claude, R. M. Hobson, G. L. Ogram, and A. W. Yau. Effective collision frequency of electrons in noble gases. *J. Phys. B: At. Mol. Phys.*, 14:1485–1495, 1981.

[11] H. Barkhausen. Two phenomena discovered with the aid of the new amplifier. *Phys. Zeits*, 20:401–403, 1919.

[12] H. Barkhausen. Whistling tones from the Earth. *Proceedings of the Institute of Radio Engineers*, 18(7):1155 – 1159, 1930.

[13] T. F. Bell, U. S. Inan, and T. Chevalier. Current distribution of a VLF electric dipole antenna in the plasmasphere. *Radio Sci.*, 41:RS2009, 2006.

[14] C. K. Birdsall and A. B. Langdon. *Plasma Physics via Computer Simulation*. Taylor & Francis, 2004.

[15] J. B. Blake, W. A. Kolasinski, R. W. Fillius, and E. G. Mullen. Injection of electrons and protons with energies of tens of MeV into L ¡ 3 on 24 March 1991. *Geophys. Res. Lett.*, 19(8):821824, 1992.

[16] H. A. Blevin and P. C. Thonemann. Plasma confinement using an alternating magnetic field. *Nuclear Fusion. Supplement*, 1(1):55–60, 1962.

[17] J.P. Boyd. *Chebyshev and Fourier Spectral Methods*. Dover, Mineola, NY, 2nd (revised) edition, 2001.

[18] C. Canuto, M. Y. Hussani, A. Quarteroni, and T. A. Zang. *Spectral Methods in Fluid Dynamics*. Berlin : Springer-Verlag, 1988.

[19] C. C. Chaston, C. W. Carlson, W. J. Peria, R. E. Ergun, and J. P. McFadden. FAST observations of inertial Alfvén waves in the dayside aurora. *Geophys. Res. Lett.*, 26(6):647–650, 1999.

[20] S. DasGupta, A. F. Witulski, B. L. Bhuva, M. L. Alles, R. A. Reed, O. A. Amusan, J. R. Ahlbin, R. D. Schrimpf, and L. W. Massengill. Effect of well and substrate potential modulation on single event pulse shape in deep submicron CMOS. *IEEE Trans. Nucl. Sci.*, 54(6):2407 – 2412, 2007.

[21] Imke de Pater and Stephen H. Brecht. SL9 impacts: VLA high-resolution observations at λ=20 cm. *Icarus*, 151(1):1 – 24, 2001.

[22] T. Drozdenko and G. J. Morales. Nonlinear effects resulting from the interaction of a large-scale Alfvén wave with a density filament. *Phys. Plasmas*, 8:3265, 2001.

[23] D. G. Dupont. Nuclear explosions in orbit. *Sci. Am.*, 290(6):100, 2004.

[24] B. Eliasson and P. K. Shukla. Dynamics of whistler spheromaks in magnetized plasmas. *Phys. Rev. Lett.*, 99:205005, NOVEMBER 2007.

[25] E. T. Everson, P. Pribyl, C. G. Constantin, A. Zylstra, D. Schaeffer, N. L. Kugland, and C. Niemann. Design, construction, and calibration of a three-axis, high-frequency magnetic probe (b-dot probe) as a diagnostic for exploding plasmas. *Rev. Sci. Instrum.*, 80(11):113505, 2009.

[26] B. Fornberg. *A Practical Guide to Pseudospectral Methods*. Cambridge Univ. Press, Cambridge, U.K., 1998.

[27] G. I. Ganguli, M. Lampe, W. E. Amatucci, and A. V. Streltsov. Active control of nuclear-enhanced radiation belt. NRL review. (Available at http://www.nrl.navy.mil/content_images/06Simulation(Ganguli).pdf), 2006.

[28] W. Gekelman. Review of laboratory experiments on Alfvén waves and their relationship to space observations. *J. Geophys. Res.*, 104(A7):14417–14435, 1999.

[29] W. Gekelman, H. Pfister, Z. Lucky, J. Bamber, D. Leneman, and J. E. Maggs. Design, construction, and properties of the large plasma research device-the LAPD at UCLA. *Rev. Sci. Instrum.*, 62:2875, 1991.

[30] W Gekelman, S Vincena, and D Leneman. Experimental observations of shear Alfvén waves generated by narrow current channels. *Plasma Physics and Controlled Fusion*, 39(5A):A101, 1997.

[31] W. Gekelman, S. Vincena, D. Leneman, and J. Maggs. Laboratory experiments on shear Alfvén waves and their relationship to space plasmas. *J. Geophys. Res.*, 102(A4):7225–7236, 1997.

[32] Walter Gekelman, David Leneman, James Maggs, and Stephen Vincena. Experimental observation of Alfvén wave cones. *Phys. of Plasmas*, 1(12):3775–3783, 1994.

[33] Walter Gekelman, Patrick Pribyl, Yuhou Wang, Alexey Karavaev, Xi Shao, and Dennis Papadopoulos. Experiments on the scattering of fast electrons by alfven waves. In *AGU Fall Meeting - 2009*, San Francisco, California, December 2009.

[34] Walter Gekelman, S Vincena, N Palmer, P Pribyl, D Leneman, C Mitchell, and J Maggs. Experimental measurements of the propagation of large-amplitude shear Alfvén waves. *Plasma Physics and Controlled Fusion*, 42(12B):B15, 2000.

[35] A. Gigliotti, W. Gekelman, P. Pribyl, S. Vincena, A. Karavaev, X. Shao, A. Surjalal Sharma, and D. Papadopoulos. Generation of polarized shear Alfvén waves by a rotating magnetic field source. *Phys. of Plamas*, 16:092106, 2009.

[36] Alex Gigliotti, Walter Gekelman, Patrick Pribyl, Yuhou Wang, Alexey Karavaev, Xi Shao, and Dennis Papadopoulos. Experiments on the scattering of fast electrons by Alfvén waves. In *51st Annual Meeting of the APS Division of Plasma Physics*, Atlanta, Georgia, November 2009.

[37] V. L. Ginzburg. *The propagation of electromagnetic waves in plasmas*. Pergamon Press, Oxford, 1964.

[38] C. Goertz and R. Boswell. Magnetosphere-ionosphere coupling. *J. Geophys. Res.*, 84(A12):7239–7246, 1979.

[39] A. V. Gordeev, A. S. Kingsep, and L. I. Rudakov. Electron magnetohydrodynamics. *Phys. Rep.*, page 243, 1994.

[40] Akira Hasegawa. Particle acceleration by MHD surface wave and formation of aurora. *J. Geophys. Res.*, 81(28):5083–5090, 1976.

[41] D. Hayward and J.W. Dungey. An Alfvén wave approach to auroral field-aligned currents. *Planet. Space Sci.*, 31(5):579 – 585, 1983.

[42] R. A. Helliwell. *Whistlers and Related Ionospheric Phenomena*. Stanford University Press, Stanford, CA, 1965.

[43] A. L. Hoffman. Rotating magnetic field current drive of FRCs subject to equilibrium constraints. *Nuclear Fusion*, 40(8):1523–1539, 2000.

[44] J. Hollweg, M. Bird, H. Volland, P. Edenhofer, C. Stelzried, and B. Seidel. Possible evidence for coronal Alfven waves. *J. Geophys. Res.*, 87(A1):1–8, 1982.

[45] Richard B. Horne, Richard M. Thorne, Yuri Y. Shprits, Nigel P. Meredith, Sarah A. Glauert, Andy J. Smith, Shrikanth G. Kanekal, Daniel N. Baker, Mark J. Engebretson, Jennifer L. Posch, Maria Spasojevic, Umran S. Inan, Jolene S. Pickett, and Pierrette M. E. Decreau. Wave acceleration of electrons in the Van Allen radiation belts. *Nature*, 437:227–230, 8 September 2005.

[46] C.-H. Hui and C. Seyler. Electron acceleration by Alfvén waves in the magnetosphere. *J. Geophys. Res.*, 97(A4):3953–3963, 1992.

[47] W. Imhof, J. Reagan, E. Gaines, , and R. Anderson. Narrow spectral peaks in electrons precipitating from the slot region. *J. Geophys. Res.*, 88(A10):8103–8110, 1983.

[48] W. L. Imhof, J. B. Reagan, H. D. Voss, E. E. Gaines, D. W. Datlowe, J. Mobilia, R. A. Helliwell, U. S. Inan, J. Katsufrakis, and R. G. Joiner. Direct observation of radiation belt electrons precipitated by the controlled injection of VLF signals from a ground-based transmitter. *Geophys. Res. Lett.*, 10(4):361–364, 1983.

[49] W. L. Imhof, J. B. Reagan, H. D. Voss, E. E. Gaines, D. W. Datlowe, J. Mobilia, R. A. Helliwell, U. S. Inan, J. Katsufrakis, and R. G. Joiner. The modulated precipitation of radiation belt electrons by controlled signals from VLF transmitters. *Geophys. Res. Lett.*, 10(8):615–618, 1983.

[50] U. S. Inan, T. F. Bell, J. Bortnik, and J. M. Albert. Controlled precipitation of radiation belt electrons. *J. Geophys. Res.*, 108(A5):1186, 2003.

[51] I. R. Jones. A review of rotating magnetic field current drive and the operaton of the rotomak a field-reversed configuration (Rotomak-FRC) and a spherical tokomak (Rotomak-ST). *Phys. of Plasmas*, 6(5):1950–1957, 1999.

[52] A. V. Karavaev, N. A. Gumerov, K. Papadopoulos, Xi Shao, A. S. Sharma, W. Gekelman, A. Gigliotti, P. Pribyl, and S. Vincena. Generation of whistler waves by a rotating magnetic field source. *Phys. of Plasmas*, 17(1):012102, 2010.

[53] A. S. Kingsep, K. V. Chukbar, and V. V. Yankov. Electron magnetohydrodynamics. *Rev. Plasma Phys.*, 16:243, 1990.

[54] I. G. Kondrat'ev, A. V. Kudrin, and T. M. Zaboronkova. Radiation of whistler waves in magnetoactive plasma. *Radio Sci.*, 27(2):315–324, 1991.

[55] M. Lampe, G. Joyce, W. M. Manheimer, A. Streltsov, and G. Ganguli. Quasineutral particle simulation technique for whistlers. *J. of Comp. Phys.*, 214:284–298, 2006.

[56] D. Leneman and W. Gekelman. A novel angular motion vacuum feedthrough. *Review of Scientific Instruments*, 72(8):3473–3474, 2001.

[57] X. Li, I. Roth, M. Temerin, J. R. Wygant, M. K. Hudson, and J. B. Blake. Simulation of the prompt energization and transport of radiation belt particles during the March 24, 1991 SSC. *Geophys. Res. Lett.*, 20(22):2423–2426, 1993.

[58] A. J. Lichtenberg and M. A. Lieberman. *Regular and Stochastic motion*. Springer-Verlag, 1983.

[59] P. Louarn, J. E. Wahlund, T. Chust, H. de Feraudy, A. Roux, B. Holback, P. O. Dovner, A. I. Eriksson, , and G. Holmgren. Observation of kinetic Alfvén waves by the FREJA spacecraft. *Geophys. Res. Lett.*, 21(17):1847–1850, 1994.

[60] G. J. Morales, R. S. Loritsch, and J. E. Maggs. Structure of Alfvén waves at the skin-depth scale. *Phys. of Plasmas*, 1(12):3765–3774, 1994.

[61] G. J. Morales and J. E. Maggs. Structure of kinetic Alfvén waves with small transverse scale length. *Phys. of Plasmas*, 4(11):4118–4125, 1997.

[62] Dwight R. Nicholson. *Introduction to Plasma Theory*. John Wiley & Sons Inc, New York, 1983.

[63] Theodore G. Northrop. *The adiabatic motion of charged particles*. Interscience Publishers, New York, 1963.

[64] Nathan Palmer, Walter Gekelman, and Stephen Vincena. Measurement of ion motion in a shear Alfvén wave. *Phys. of Plasmas*, 12(7):072102, 2005.

[65] K. Papadopoulos. Satellite threat due to high altitude nuclear detonation. Presentation at Future of Space: 1st Meeting of Scientific Panel, The Eisenhower Institute, Washington, D. C.. (Available at http://www.lightwatcher.com/chemtrails/Papadopoulos-chemtrails.pdf), 11 December 2001.

[66] J. Parmentola. High altitude nuclear detonations (HAND) against low earth orbit satellites (HALEOS). Report of the Defense Threat Reduction Agency, Advanced Systems and Concepts Office, Fort Belvoir, Va. (Available at http://www.fas.org/spp/military/program/asat/haleos.pdf), 2001.

[67] J. Reagan, R. Meyerott, J. Evans, W. Imhof, and R. Joiner. The effects of energetic particle precipitation on the atmospheric electric circuit. *J. Geophys. Res.*, 88(C6), 1983.

[68] D. R. Roberts, N. Hershkowitz, R.P. Majeski, and D. H. Edgell. M=-1 Alfvén wave beach heating of two-ion mirror plasmas. *Topical conference on Radiofrequency power in plasmas, AIP Conference Proceedings*, 190(1):462–465, 1989.

[69] J.-A. Sauvaud, R. Maggiolo, C. Jacquey, M. Parrot, J.-J. Berthelier, R. J. Gamble, and Craig J. Rodger. Radiation belt electron precipitation due to VLF transmitters: Satellite observations. *Geophys. Res. Lett.*, 35:L09101, 2008.

[70] D. Shaikh. Theory and simulations of whistler wave propagation. *J. Plasma Physics*, 75(1):117132, 2009.

[71] D. Shaikh, A. Das, and P. Kaw. Hydrodynamic regime of two-dimensional electron magnetohydrodynamics. *Phys. Plasmas*, 7(5):1366–1373, May 2000.

[72] X. Shao, Shing F. Fung, L. C. Tan, K. Papadopoulos, M. Wiltberger, and M. C. Fok. Investigation of 3D energetic particle transport inside quiet-time magnetosphere using particle tracing in global MHD model. *Geophysical Monograph Series*, 155:307–319, 2005.

[73] Xi Shao, K. Papadopoulos, and A. Surjalal Sharma. Control of the energetic proton flux in the inner radiation belt by artificial means. *J. Geopphys. Res.*, 114:A07214, 2009.

[74] M. S. Shea, D. F. Smart, J. H. Allen, and D. C. Wilkinson. Spacecraft problems in association with episodes of intense solar activity and related terrestrial phenomena during March 1991. *IEEE Trans. Nucl. Sci.*, 39(6):1754 – 1760, 1992.

[75] I. Steer. Briefing: High-altitude nuclear explosions: Blind, deaf and dumb. *Janes Defense Weekly*, 38:20–23, 23 October 2002.

[76] R. L. Stenzel. Self-ducting of large-amplitude whistler waves. *Phys. Rev. Lett.*, 35(9):574, 1975.

[77] R. L. Stenzel. Antenna radiation patterns in the whistler wave regime measured in a large laboraory plasma. *Radio Sci.*, 11(12):1045–1056, 1976.

[78] T. H. Stix. *Waves in Plasmas*. AIP, New York, 1992.

[79] A. V. Streltsov, M. Lampe, W. Menheimer, G. Ganguli, and G. Joyce. Whistler propagation in inhomogeneous plasma. *J. Geophys. Res.*, 111:A03216, 2006.

[80] T. F. Tascione. *Introduction to the Space Environment*. Malabar, Florida USA: Kreiger Publishing CO., 2nd edition, 1994.

[81] J. O. Thomas and B. J. Landmark, editors. *Plasma Waves in Space and in the Laboratory*. American Elsevier, New York, 1969.

[82] W. B. Thompson. *An introduction to plasma physics*. Pergamon Press, Oxford, 1st edition, 1962.

[83] A. Vampola and G. Kuck. Induced precipitation of inner zone electrons, 1. observations. *J. Geophys. Res.*, 83(A6):2543–2551, 1978.

[84] A. L. Vampola and A. Korth. Electron drift echoes in the inner magnetosphere. *Geophys. Res. Lett.*, 19(6):625–628, 1992.

[85] S. Vincena, W. Gekelman, and J. Maggs. Shear Alfvén waves in a magnetic beach and the roles of electron and ion damping. *Phys. Plasmas*, 8(9):3884, 2001.

[86] J. Vranjes, D. Petrovic, S. Poedts, M. Kono, and V. M. Cadez. Unstable kinetic Alfvén wave in partially ionized plasma. *Planet. Space Sci.*, 54:641–644, 2006.

[87] J.-E. Wahlund, P. Louarn, T. Chust, H. de Feraudy, A. Roux, B. Holback, P.-O. Dovner, and G. Holmgren. On ion acoustic turbulence and the nonlinear evolution of kinetic Alfvén waves in aurora. *Geophys. Res. Lett.*, 21(17):1831–1834, 1994.

[88] J. R. Wait. *Electromagnetics and plasmas*. Holt, Rinehart and Winston, New York, 1968.

[89] A. D. M. Walker. *Plasma Waves in the Magnetosphere*. Springer-Verlag, New York, 1993.

[90] M. Walt and W. MacDonald. The influence of the Earth's atmosphere on geomagnetically trapped particles. *Rev. Geophys.*, 2:543–577, 1964.

[91] Martin Walt. *Introduction to Geomagnetically Trapped Radiation*. Cambridge University Press, 2005.

[92] T. N. C. Wang and T. F. Bell. On VLF radiation resistance of an electric dipile in a cold magnetoplasma. *Radio Sci.*, 5(3):605, 1970.

[93] T. N. C. Wang and T. F. Bell. Electric dipole radiation at VLF in a uniform warm magneto-plsmas. *Rev. de Physique Appliquee*, 7:11, 1972.

[94] T. N. C. Wang and T. F. Bell. VLF/ELF radiation patterns of arbitrary oriented electric and magnetic dipoles in a cold lossless multicomponent magnetoplasma. *J. Geopphys. Res.*, 77(7):1174–1189, 1972.

[95] J. Wygant, F. Mozer, M. Temerin, J. Blake, N. Maynard, H. Singer, and M. Smiddy. Large amplitude electric and magnetic field signatures in the inner magnetosphere during injection of 15 MeV electron drift echoes. *Geophys. Res. Lett.*, 21(16):1739–1742, 1994.

[96] J. R. Wygant, A. Keiling, C. A. Cattell, M. Johnson, R. L. Lysak, M. Temerin, F. S. Mozer, C. A. Kletzing, J. D. Scudder, W. Peterson, C. T. Russell, G. Parks, , M. Brittnacher, G. Germany, and J. Spann. Polar spacecraft based comparisons of intense electric fields and Poynting flux near and within the

plasma sheet-tail lobe boundary to UVI images: An energy source for the aurora. *J. Geophys. Res.*, 105(A8):18675–18692, 2000.

[97] Y. Yasaka, R. Majeski, J. Browning, N. Hershkowitz, and D. Roberts. ICRF heating with mode control provided by a rotating field antenna. *Nucl. Fusion*, 28(10):1765–1770, 1988.